NATIONAL AND KAPODISTRIAN UNIVERSITY OF ATHENS
SCHOOL OF SCIENCE
FACULTY OF PHYSICS
DEPARTMENT OF ASTROPHYSICS, ASTRONOMY AND MECHANICS

MASTER THESIS

Effect of Very Low Frequency (VLF) waves on the acceleration of electrons to relativistic energies

Afroditi Nasi
201735

Supervisor:
Prof. Ioannis A. Daglis

ATHENS
06/2019

Acknowledgements

The present study constitutes the Master Thesis required for the acquisition of the Master of Science Diploma offered by the Faculty of Physics of the National and Kapodistrian University of Athens, during the period of 2017-2019. The Supervisor of this study is Prof. I. A. Daglis, and the Thesis Committee is comprised by Prof. I. A. Daglis, Prof. A. Mastichiadis and Research Director Dr G. Balasis.

I would like to express my sincere gratitude to my Supervisor, Professor Ioannis A. Daglis, for his continuous support, his excellent guidance and his patience. He has been a great mentor, presenting fine opportunities for me to work on exciting and diverse projects.

Also, I would like to thank the rest of my Thesis Committee, Professor Apostolos Mastichiadis and Research Director Dr George Balasis, for their encouragement and support.

This work would not have been possible without the contribution of my colleague, Dr C. Katsavrias, whose valuable comments and guidance have played an important role on my engagement with this subject, and also without the contribution and support of Professor Wen Li.

Finally, I owe my deepest gratitude to my family and to my partner in life, Alexandros, for their unlimited love and understanding. Especially, I want to thank my sister, Maria, for her invaluable support and contribution in our everyday life.

Abstract

Local acceleration driven by whistler mode chorus waves is fundamentally important for the acceleration of seed electrons in the outer radiation belt to highly relativistic energies. Yet, this mechanism strongly depends on substorm activity and on the source and seed electron populations injected by the substorms into the inner magnetosphere.

In this work we use Van Allen Probes (RBSP) data to investigate the relationship between source electrons, seed electrons, chorus waves and ULF waves during periods of increased substorm activity. To that end we calculate the electron phase space density (PSD) for five values of the first adiabatic invariant μ, corresponding to source and seed electrons, and for narrow value ranges of the adiabatic invariants K and L*. We examine these parameters during 28 selected events, out of which, 20 result in enhancement and 8 in depletion of the average relativistic electron PSD. Furthermore, we perform a superposed epoch analysis in order to compare the time evolution of the wave activity with the electron PSD, defining a key time t_0 as the start time of continuous substorm activity, as indicated by the decrease of AL index.

Chapter 1 includes the necessary physical background supporting this study, and a brief presentation of the missions and instruments from which the data we use are provided. Chapter 2 contains the event and data selection, and Chapter 3 the way we manipulate these data to compute all the important quantities for this study. Chapter 4 briefly presents the method of the Superposed Epoch Analysis that we perform, and a description of the produced plots. Chapter 5 includes the statistical analysis of the 28 selected events by presenting all the produced plots organised in certain groups, the brief comparison between some of the quantities, and some important comments, later presented in Chapter 6 as the final conclusions of this study.

A summary of the conclusions is that the effect of Very Low Frequency (VLF) waves on the acceleration of electrons to relativistic energies seems to be determined by the abundance of seed electrons, mostly at L*=4-5, the nominal heart of the outer radiation belt.

Table of Contents

List of Figures

List of Tables

Chapter 1: Introduction

In this chapter we present some of the physical background useful for our study.

1.1 Terrestrial Magnetosphere

The cavity that is formed in the solar wind by a planet's magnetic field is called a magnetosphere. Inside it, the planetary magnetic field is dominant and defines the morphology and structure of the magnetosphere. It is filled with sparse plasma, which the magnetopause and the shock front separate from the dense plasma of the solar wind. Depending on the solar wind conditions, the magnetosphere is compressed on the day side and elongated on the night side, forming the magnetotail.

The Earth's quasi-bipolar magnetic field has the same effect on the solar wind and forms the terrestrial magnetosphere. It is defined as the space, outside the ionosphere, where the geomagnetic field is dominant. It extends from 6 to 13 R_E (Earth radii) on the day side, and much more on the night side, depending on the solar wind conditions, and contains several different structures, plasma populations and electric current systems (Figure 1).

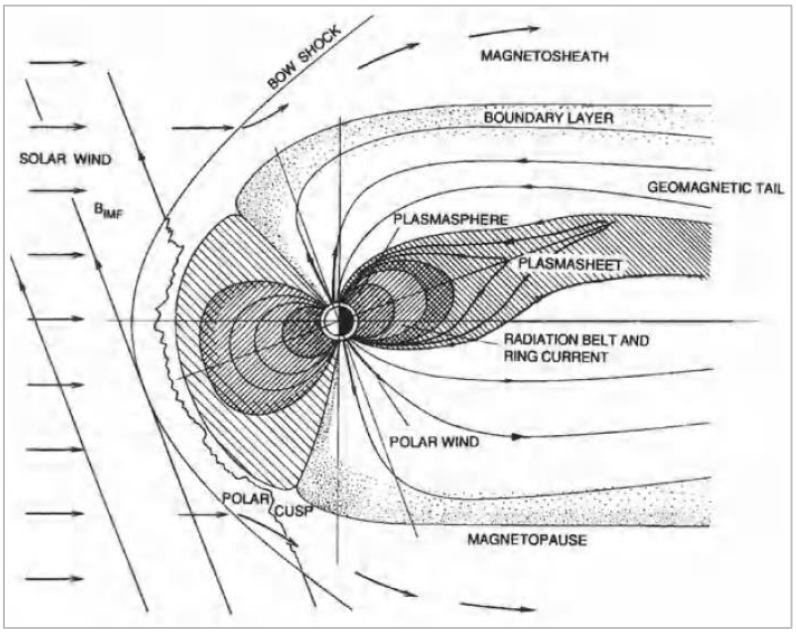

Figure 1 The structure of the terrestrial magnetosphere. [Kallenrode (2004), Parks (1991)]

1.1.1 Geomagnetic field

The outer core of the Earth consists of molten iron and other conducting materials that, following the natural process of geodynamo, generate electric currents which in turn generate the geomagnetic field. It is approximately a dipole field, with its axis tilted by 11° in respect to the rotational axis of the Earth. The north pole of the geomagnetic dipole field is located near the south geographic pole and is thus called south magnetic pole, and conversely for the north magnetic pole (Figure 2).

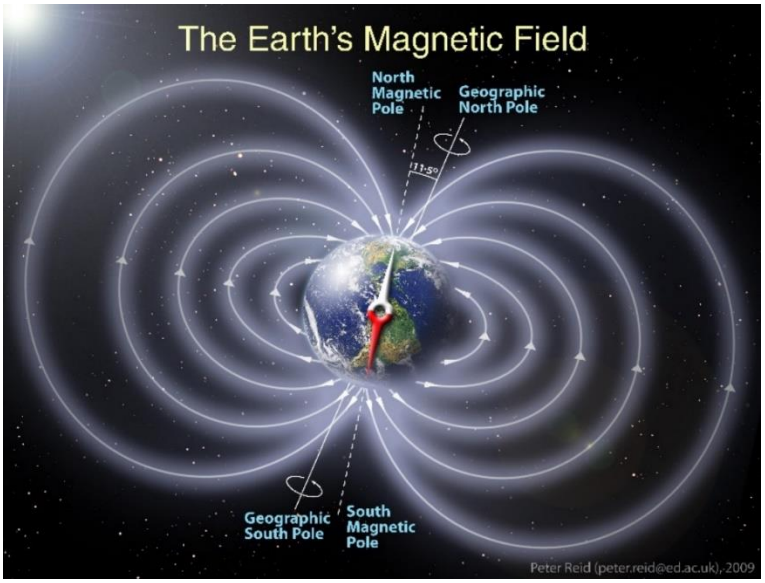

Figure 2 The ideal magnetic dipole field that is formed by the geodynamo process. This approximation is valid up to 6 R_E. [NASA, www.nasa.gov, Peter Reid, University of Edinburg, 2009]

Some regions on the Earth's crust present permanent magnetisation, thus disturbing the dipole field close to the surface (Figure 3). Also, currents in the ionosphere and magnetosphere can affect the dipole field. Together, the crust's field, the currents and the dipole filed, form the geomagnetic field. Its intensity is denoted by B, is measured in Tesla [T] or Gauss [G], and can be represented by a three-dimensional vector with three components (horizontal, vertical, declination or north, vertical, east).

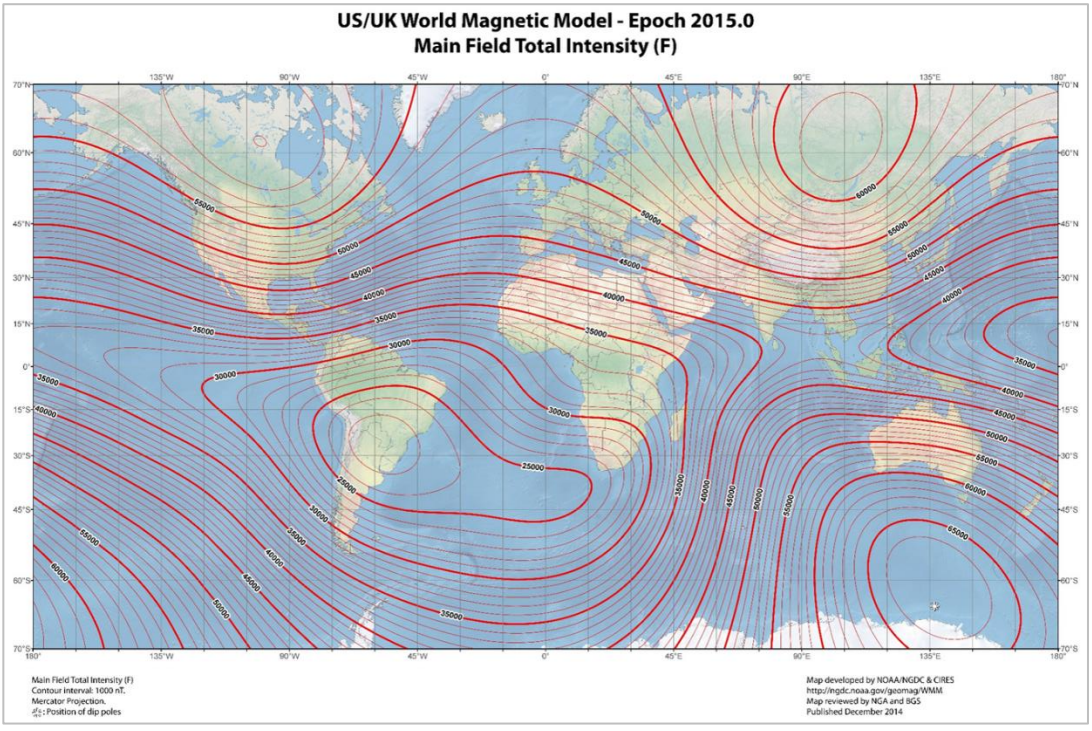

Figure 3 The geomagnetic field intensity on the Earth's surface, according to the 2005 World Magnetic Model (WMM). It is obvious that the field does not fit with the dipole approximation. [NOAA, www.ngdc.noaa.gov]

Starting from the geomagnetic poles, open field lines emerge, continuing in space and stretching to the night side due to the solar wind. Moving closer to the equator on the Earth's surface, the field lines turn to closed, some still following the stretching to the night side (Figure 4).

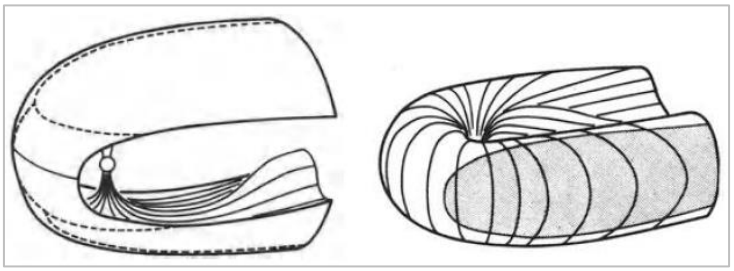

Figure 4 The magnetospheric regions including open (on the left) and closed magnetic field lines (on the right). [Kallenrode (2004), Crooker (1977)]

1.1.2 Trapped particle motion inside the magnetosphere

The charged particles that are trapped inside the magnetosphere are affected by the geomagnetic field and follow three distinct types of motion (Figure 5), affected by and at the same time forming the different trapped populations of particles, e.g. the radiation belts and the ring current. These motions are:

- The **gyration motion**, about a magnetic field line, with a radius depending on the values of the magnetic field B, and the particle properties.
- The **bounce motion**, along a field line, following its curvature drift, and bouncing between two mirror points near the geomagnetic poles, whose location depends on the magnetic field B, its gradient, and the particle properties.
- The azimuthal **drift motion**, perpendicular to the magnetic field lines, because of its gradient, going around the Earth, with a radius and a velocity depending on the magnetic field B and the particle properties.

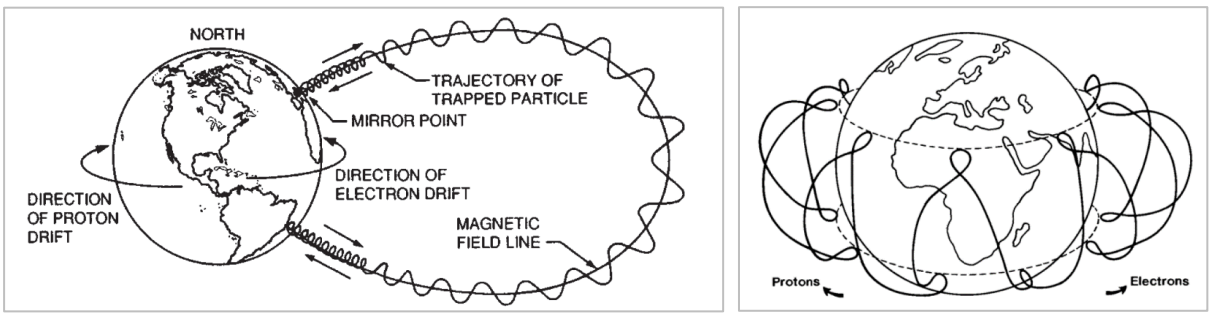

Figure 5 Trajectory of trapped electrons and protons experiencing gyration, magnetic mirroring, gradient and curvature drifts in the geomagnetic field. [Walt (1994), Kivelson & Russel (1995)]

1.1.3 Adiabatic invariants

Each trapped particle motion associates with a quantity that we consider a constant of motion, analogous to the conservation of energy, momentum and angular momentum in mechanical systems. These are called adiabatic invariants, they are approximate constants that exist if a system is undergoing periodic motions that change very slightly over a period, and are very useful in the study of trapped particles.

They can be extracted by calculating the integral of the momentum over a complete cycle, for each motion. According to Hamiltonian theory, the action of every periodic motion should be constant, calculated as the integral of the particle's momentum P_{gen} in generalised coordinates q_{gen}:

$$I = \oint P_{\text{gen}}\, dq_{\text{gen}}$$

If the temporal changes of the magnetic field are quite slow, meaning that the changes happen very slightly over a period, then we assume that the particle's motion is quasi-periodic, and the integral can be taken as a constant. This happens when:

$$\left|\frac{1}{B}\frac{\partial B}{\partial t}\right| \ll \left|\frac{1}{\tau}\right|$$

Where τ is the period of each motion.

For the **gyration motion**, we calculate the integral J_1 of the momentum on a circular orbit perpendicular to the magnetic field:

$$J_1 = \oint \vec{P}\,\vec{dl} \;\rightarrow\; \ldots \rightarrow J_1 = \frac{\pi p_\perp}{qB}$$

Instead, we define a new invariant, μ, called the **magnetic moment**:

$$\mu = \frac{q}{2\pi m} J_1 \;\rightarrow\; \boldsymbol{\mu = \frac{p_\perp^2}{2mB}} \left[\frac{\boldsymbol{MeV}}{\boldsymbol{G}}\right]$$

The adiabatic invariant μ is conserved when:

$$\left|\frac{1}{B}\frac{\partial B}{\partial t}\right| \ll \left|\frac{1}{\tau_g}\right| = \left|\frac{qB}{2\pi m}\right| \quad \text{and} \quad \left|\frac{\nabla B}{B}\right| \ll \left|\frac{1}{r_g}\right| = \left|\frac{qB}{mV_\perp}\right|$$

For electrons: $\tau_g \approx 10^{-3} s$.

Because J_1=constant and μ=constant, it is also $\frac{p_\perp^2}{B}$=constant $\rightarrow$ $\frac{\mathrm{p}^2 \sin^2 a}{B}$=constant, where α is the pitch angle (the angle between the velocity V and the B). This leads to the determination of the mirroring points based on the B and α values on the equator:

$$\frac{\mathrm{p}^2 \sin^2 a_m}{B_m} = \frac{\mathrm{p}^2 \sin^2 a_{eq}}{B_{eq}} \xrightarrow{a_m = 90^o} \sin^2 a_{eq} = \frac{B_{eq}}{B_m}$$

Which in turn determines the particle's bounce motion.

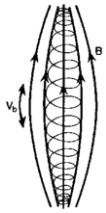

For the **bounce motion**, we calculate the integral J_2 of the momentum of the motion parallel to the magnetic field, between the mirroring points, but instead denote it as J and call it the longitudinal invariant:

$$J_2 = \oint \vec{P}\,\overrightarrow{ds} \;\rightarrow\; \dots \;\rightarrow\; J_2 = 2\int_{S_m}^{S_{m'}} p_{\parallel}\,ds \quad or \quad J = \int p_{\parallel}\,ds \;\rightarrow$$

$$\rightarrow\; J = \sqrt{8m_0\mu}\int_{S_m}^{S_{m'}} \left(B_m - B(s)\right) ds$$

Instead we define a new invariant, K, called **Kauffman's K**:

$$K = \frac{J}{\sqrt{8m_0\mu}} \;\rightarrow\; \boldsymbol{K = \int_{S_m}^{S_{m'}} \left(B_m - B(s)\right) ds \;\left[G^{1/2}\cdot R_E\right]}$$

The adiabatic invariant K is conserved when $\left|\frac{1}{B}\frac{\partial B}{\partial t}\right| \ll \left|\frac{1}{\tau_b}\right|$. For electrons: $\tau_b \approx 10^0 s$.

It defines the magnetic shells on which the particles drift around the Earth.

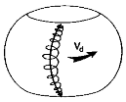

For the **drift motion**, we calculate the integral J_3 of the momentum of the motion perpendicular to the magnetic field and processing around the Earth, returning to the same field line:

$$J_3 = \oint \vec{P}\,\overrightarrow{dl} \;\rightarrow\; \dots \;\rightarrow\; J_3 = q\oint B\,ds = q\Phi$$

Instead, we define a new variant, ϕ, called the flux invariant:

$$\Phi = \frac{J_3}{q} \;\rightarrow\; \Phi = \oint B\,ds$$

It determines that the magnetic flux contained by the drift shells remains constant.

We also define another invariant, called **Roederer's L**:

$$\boldsymbol{L^* = -\frac{2\pi M_E}{\Phi R_E}}$$

where M_E is the Earth's magnetic moment and R_E is the Earth's radius.

The adiabatic invariant L* is conserved when $\left|\frac{1}{B}\frac{\partial B}{\partial t}\right| \ll \left|\frac{1}{\tau_d}\right|$. For electrons: $\tau_d \approx 10^3 s$.

In this study, we are interested in trapped electrons, and we use the three adiabatic invariants **μ,K,L***.

Also, another useful parameter that we use, is **McIlwain's L**, which is defined as the distance from the center of the Earth to the equatorial crossing point of a field line in a dipole magnetic field (Figure 6). If a magnetic field is completely bipolar, the parameters L and L* are equal. In reality, L* and L values can diverge significantly, especially as we move outward from the planet, and tend to converge as we move inward, as the quasi-bipolar approximation is more robust.

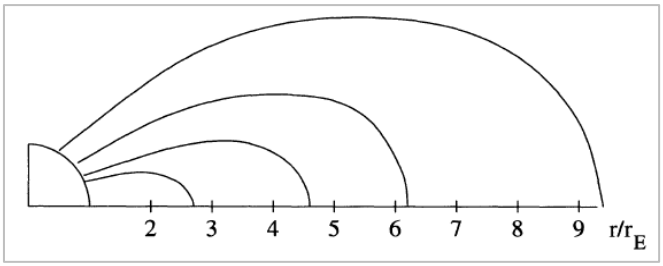

Figure 6 The definition of the McIlwain's L parameter as the distance in R_E at which a field line of the dipole geomagnetic field crosses the magnetic equator. [Kallenrode (2004)]

1.1.4 Trapped populations and magnetospheric structure

The interaction of the solar wind with the terrestrial magnetosphere defines the magnetic field and thus the magnetospheric structure. Satellite experiments have identified the principal features of the magnetosphere (Figure 7).

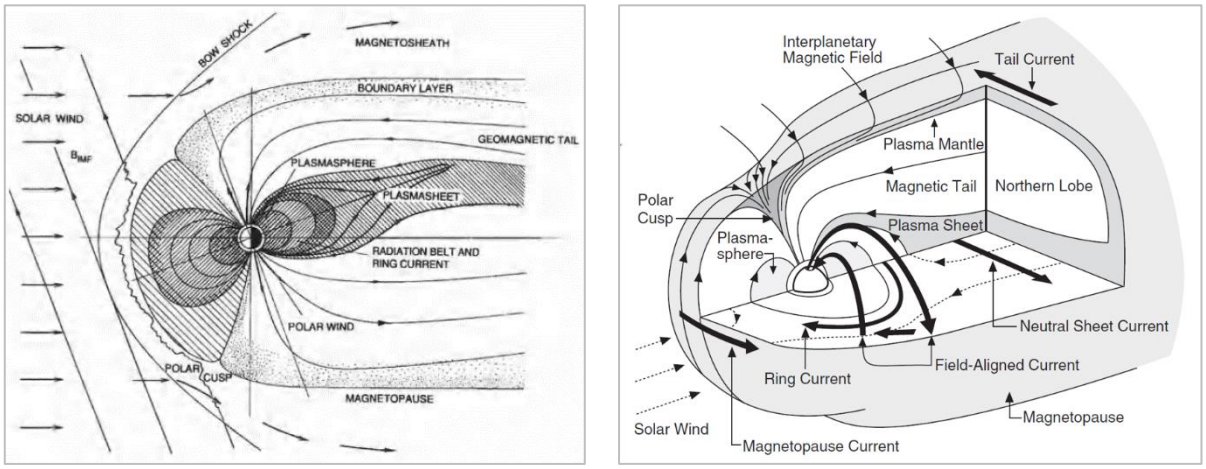

Figure 7 The most important internal structures, trapped particle populations and electric currents of the magnetosphere. [Kallenrode (2004), Parks (1991), Russel (2007)]

Here we mention only some of the structures which are important for this study.

i. The magnetopause

The outer edge of the magnetosphere is called the magnetopause, and is defined as the separatrix on which the pressure of the magnetospheric plasma is equal to the solar wind pressure. On this surface lie the last closed magnetic field lines of the geomagnetic field. Because of the velocity difference between the two plasmas, in front of the magnetopause a bow shock is formed, and between them accumulates compressed solar wind plasma, inside the magnetosheath (Figure 7).

We are interested in the dayside magnetopause, as this is the main area that magnetic reconnection occurs leading to magnetospheric disturbances, and also near it the L1 point is located, where we can extract the solar wind properties from satellite measurements. In this study, the location of the nose of the dayside magnetopause on the equatorial plane is calculated using the Shue et al. [1998] model.

ii. The ring current

The ring current is a toroidal electric current, formed by the azimuthal drift motion of electrons and ions that originate in the solar wind and the ionosphere and reach the inner magnetosphere by drifting from the magnetotail (Figure 7). Because of its shape and direction, it forms its own magnetic field component, with an axis almost parallel to that of the Earth's dipole and the same polarity (southward). Although, on the surface of the Earth, and on the (magnetic) equator, the geomagnetic field is northward, meaning that the magnetic component of the ring current is opposite, and that is the reason why during magnetic storms, when the ring current is enhanced, we detect reductions of the total geomagnetic field.

iii. The radiation belts

The Van Allen radiation belts are two toroidal structures of energetic particles azimuthally drifting around the Earth. The inner belt is comprised by energetic electrons and ions, mostly protons, is very stable, and covers the region of L<2. The outer belt is comprised almost entirely of energetic electrons (100 keV – several MeV), is very dynamic, and covers the region of L=3-6. The two belts are separated by a slot region, characterised by lower energy density (Figure 8).

In this study we are interested in the outer radiation belt, which is known to undergo drastic changes in magnetically disturbed periods, such as geomagnetic storms. The dynamics of the energetic electron population inside the outer radiation belt depend both on external (solar wind parameters) and internal (e.g. waves) procedures, and will be covered in the following chapters.

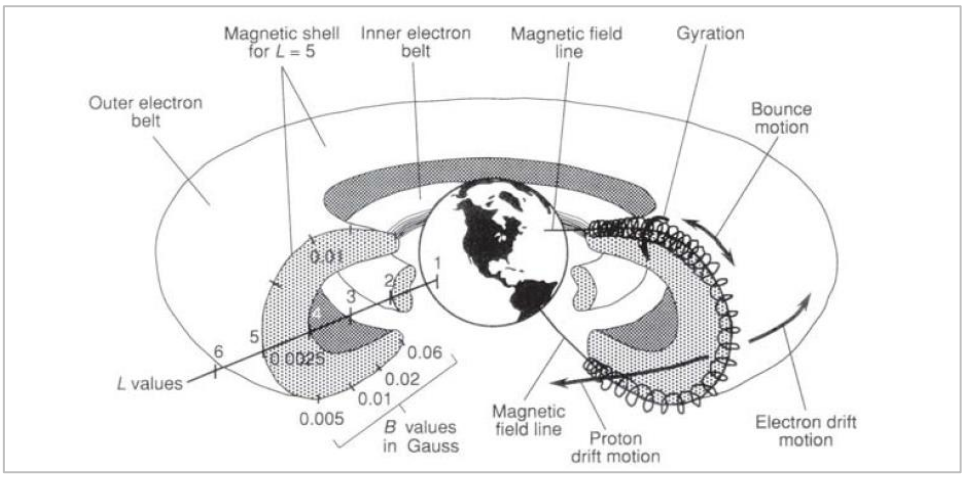

Figure 8 The Van Allen radiation belts, their location relative to the Earth, and the three motions of trapped particles. [Mitchel (1994)]

iv. The plasmasphere

The region above the upper ionosphere, containing dense, low energy (≈1 eV) plasma, is called the plasmasphere. In the plasmasphere, the particle motion is entirely dominated by the geomagnetic field. This region corotates with the Earth, shrinks with increased space weather activity and expands or refills during times of inactivity.

Moving outwards, the region where the plasma density decreases by an order of magnitude is considered its outer boundary, called the plasmapause. In this study, the average location of the plasmapause on the equatorial plane is calculated using the O'Brien et al. [2003] model.

1.2 The Sun

The Sun is our closest star. It is a common dwarf star of the main sequence, of G2V spectral type and an effective temperature of 5.780 K. In order to study it, we define different layers in its interior, called the core, the radiative zone, the convective zone, the photosphere, the chromosphere, the transition region and the corona. Each layer is characterised by different phenomena releasing wave or particle radiation. The three outer layers form the Sun's atmosphere. The photosphere is considered as the visible surface of the Sun, as it thermally radiates, giving the visible continuous solar spectrum.

1.2.1 Solar magnetic field and structures

The variability of the Sun follows an 11-year activity cycle (or a 22-year magnetic cycle). When the Sun is considered active, many dynamic and explosive phenomena arise on its surface, that may disturb the geospace environment. These active regions are located on the photosphere and the corona, and the most important for this study are the solar wind (SW), the stream interaction regions (SIRs) and the interplanetary coronal mass ejections (ICMEs).

These phenomena arise because of instabilities of the solar magnetic field. The hot plasma inside the core, again following the dynamo process, forms the Sun's dipole magnetic field. According to Babcock's theory (Figure 9), and because of the differential rotation of the solar plasma, the magnetic field lines become stretched and tangled creating loops that rise from its surface leading to the formation of coronal loops, sunspots (the footprints of the loops), filaments (projection of the loops on the solar disk), prominences (angle view of the loops outside the solar disk), etc. There formations often interact or become unstable, exploding and releasing great amounts of energy and plasma, for example in the form of solar flares and CMEs.

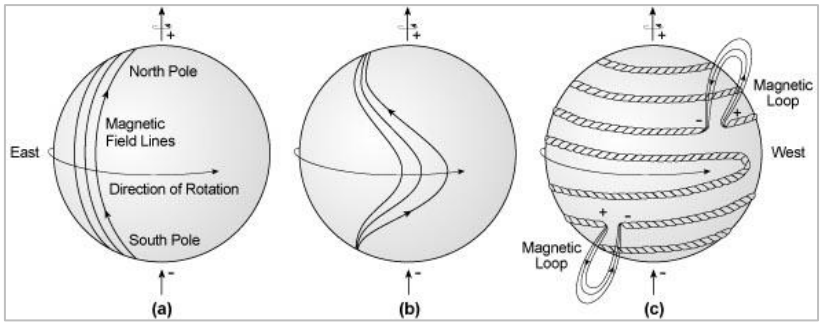

Figure 9 The Babcock model for the formation of the magnetic loops. (a) At solar activity minimum, the magnetic field has a simple dipole form. (b) Due to the differential rotation, the magnetic field lines are stretched at the equator. (c) The magnetic field lines become tangled and form loops and other structures that rise to the solar surface. [Prof. Kenneth R. Lang, Tufts University, 2010]

i. Solar Wind (SW)

The solar wind is a constant stream of solar plasma starting from the corona and reaching the edges of the heliosphere (the solar magnetosphere). The solar wind flows from the Sun towards all directions, with a velocity ranging from 300 to 800 km/s. Inside it, the magnetic field lines are ''frozen in'', and form the Interplanetary Magnetic Field (IMF). They start from inside the Sun, so its rotation makes them form the so-called Parker spirals (Figure 10).

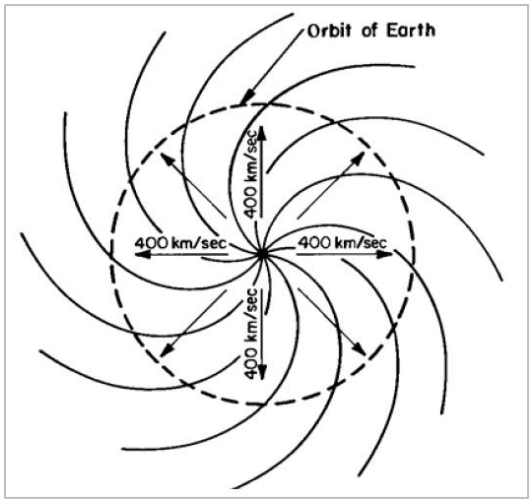

Figure 10 The Parker spirals formed by the interplanetary magnetic field lines, emerging from the Sun's interior. [Kivelson & Russel (1995), Parker (1963)]

Depending on the solar activity, or on the solar structure responsible for this stream, the solar wind has different properties like the velocity, the dynamic pressure, the density, the magnitude and polarity of the magnetic field, etc. This leads to two main types of solar wind, the slow (V=250-400 km/s) and the fast (V=400-800 km/s) solar wind, with different properties.

ii. Stream Interaction Regions (SIRs)

Because the solar magnetic field axis is tilted in respect to the rotational axis of the Sun, and because of the differential rotation of the solar plasma, the slow and fast solar wind can interact and create an increased pressure region, with or without a shock (Figure 11). This region corotates with the Sun and is called a Stream Interaction Region (SIR). If its rotation period lasts more than the solar rotation period (27 days) it is called a Corotating Interaction Region (CIR). The increased pressure and plasma speed as well as the appearance of a southward magnetic field of these SIRs can often lead to enhanced geomagnetic activity.

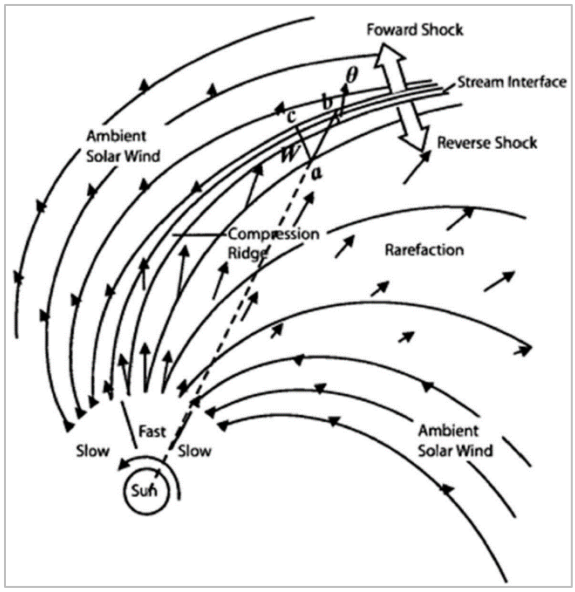

Figure 11 Schematic of a stream interaction region (SIR). [Jian et al. (2006)]

iii. Interplanetary Coronal Mass Ejections (CMEs)

The coronal loops that lead to solar flares can sometimes also lead to the explosive cut off and ejection of a magnetic structure from the solar corona, which then propagates into the heliosphere. This is called a Coronal Mass Ejection (CME), and propagating into the interplanetary medium, maybe passing near the Earth, is called an Interplanetary CME (ICME) (Figure 12). During these ejections, huge amounts of mass and energy are released, in the form of magnetic clouds, accompanied by shocks and plasma sheaths. The increased pressure, plasma speed, density and the compressed magnetic field undergoing large amplitude fluctuations often producing southward components, can often lead to enhanced geomagnetic activity.

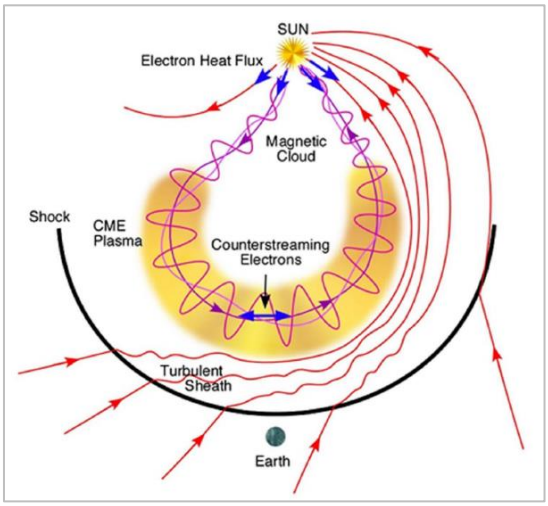

Figure 12 Schematic of an interplanetary coronal mass ejection (ICME). [Zurbuchen & Richardson (2006)]

In this study we examine magnetospheric disturbances caused by both ICMEs and SIRs, without denoting the cause.

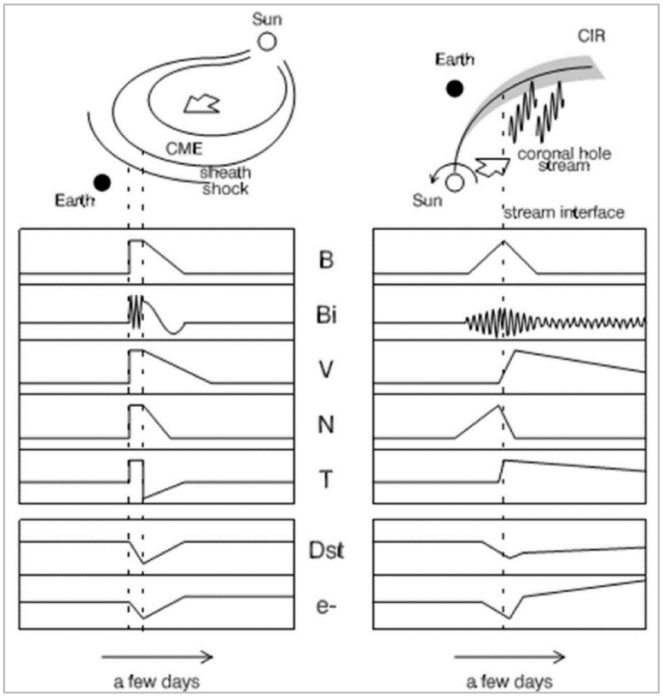

Figure 13 The effects and evolution of various solar wind parameters caused by an ICME and an SIR.

[Kataoka & Miyoshi (2006)]

SIRs exhibit more fluctuating z component of the magnetic field (Bi) than ICMEs. ICMEs exhibit a much steeper gradient of solar wind speed V and density N as well as temperature T than SIRs. These differences lead to different magnetospheric response.

The main difference between a disturbance caused by an ICME and an SIR (Figure 13) is that an ICME is more dense and has a statistically stronger shock, leading to a sudden and strong compression of the magnetopause. On the other hand, an SIR can lead to a more subtle but longer lasting compression. These will in turn lead to a different geomagnetic response and a difference in the excitation of waves, which will be further explained in the following sections.

1.2.2 Magnetic reconnection

The field lines of a magnetic field are not always stable in space and time, but they can move, pulsate and compress. If two field lines come very close, they interact and break, releasing great amounts of energy. If these lines have a specific alignment, then their remnants can reconnect, forming new closed lines, maybe in a different formation. This process is called magnetic reconnection, and is a crucial parameter of solar flares, CMEs, and even geomagnetic disturbances such as storms and substorms.

The ICMEs and SIRs propagating to Earth, transfer the frozen in interplanetary magnetic field. When these formations reach the terrestrial dayside magnetopause, whose field at this region is northward, they interact with these field lines by magnetic reconnection, changing the formation of the local magnetic field. If the interplanetary magnetic field is southward, and thus opposite from the magnetic field of the magnetopause, then the magnetic reconnection is further enhanced, leading to large scale disturbances and variations of the geomagnetic field. The magnetic field lines of the ICME or the SIR connect with those of the magnetopause, and are stretched towards the magnetotail, compressing it and maybe even leading to further reconnection inside it (Figure 14).

The magnetic reconnection releases huge amounts of energy and particles inside the magnetosphere, transferring them to the magnetotail, where they are further propagated inward or outward depending on the local magnetospheric properties.

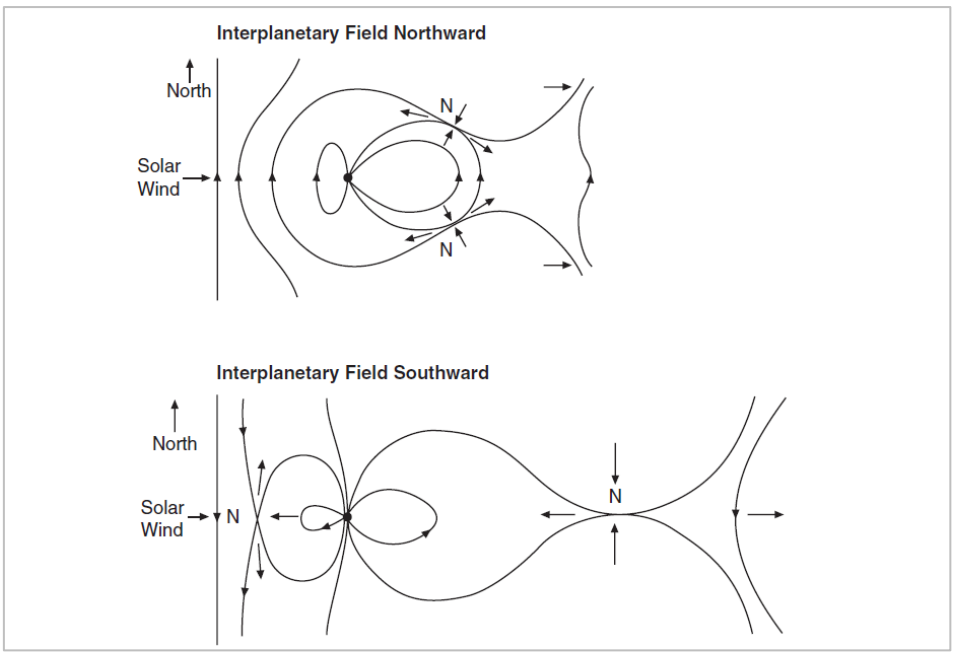

Figure 14 Two models developed by Dungey, about the magnetic reconnection when the interplanetary magnetic field is northward (up) or southward (down). N denotes neutral points where the magnetic field is eliminated. Today they are called X-points. [Russel (2007)]

1.3 Geospace disturbances

The magnetospheric disturbances caused by the arrival of ICMEs and SIRs at the terrestrial region can be divided into two main categories: geomagnetic storms and magnetospheric substorms. These disturbances define geomagnetic activity, are mainly affected by the occurrence of magnetic reconnection, and can last from several hours to a few days, so are considered middle scale variations.

Other magnetospheric disturbances can have different time scales. Large scale variations can include periodic changes due to solar oscillations and solar wind variations, such as the 27-day periodicity following the solar rotation or the 11-year periodicity due to the solar activity cycle. Small scale variations can include disturbances in the order of several minutes to fractions of seconds, and correspond to the generation of oscillations and waves on the magnetosphere.

1.3.1 Geomagnetic storms

i. Definition

A temporal disturbance of the terrestrial magnetosphere that lasts from a few hours to a few days is called a geomagnetic storm. It is characterised by the sudden and strong decrease of the geomagnetic field. A necessary condition for a storm to occur is that the solar wind or the interplanetary structure arriving at the dayside magnetopause should have a southward magnetic field, thus leading to enhanced magnetic reconnection and to energy transfer to the magnetosphere. The geomagnetic storms occur with a frequency that depends on the solar activity cycle.

ii. Phases

A geomagnetic storm is divided in three or four phases:

- **Sudden Storm Commencement (SSC)**: The solar wind or its propagating structure (ICME or SIR) reaches the dayside magnetopause. Because of its enhanced pressure and density, it compresses the magnetopause, which in turn compresses the magnetic field lines inside the magnetosphere making them pulsate. This creates a wave packet propagating to the inner magnetosphere, which is called a Sudden Storm Commencement and defines the start a geomagnetic storm. It lasts only for some minutes and does not occur in every storm.

- **Initial phase**: The compression of the dayside magnetopause leads to the enhancement of the magnetopause current and thus to a small increase of the horizontal component of the geomagnetic field on the Earth's surface. It can last for some hours.

- **Main phase**: The solar wind structure transfers its frozen in magnetic component. If this component is southward and lasts for several hours, it leads to enhanced magnetic reconnection at the dayside magnetopause. Its main effect is the following enhancement of the ring current, as a result of the transfer of particles to the magnetotail and their drift to the inner magnetosphere. As the ring current gets enhanced, its magnetic component also increases, leading to a sudden and strong decrease of the horizontal component of the geomagnetic field on the Earth's surface. This phase can last from some to 12 hours, and the storms are further divided into subcategories depending on the magnitude of the geomagnetic field decrease.

- **Recovery phase**: After the magnetic reconnection stops, particle injections decline, and the ring current weakens. After the high energy particles also get depleted after a few days, the geomagnetic field and the magnetosphere gradually return to their pre-disturbance states.

iii. Indices: Dst, SYM-H

An index is a parameter used to briefly present information of a phenomenon. In our case, the phenomena are geospace disturbances, so various indices are used to quantitatively describe the geomagnetic field variations in time.

For the geomagnetic storms, a useful index is the **Disturbance Storm Time (Dst) index**. It is measured in nanoTesla [nT] and is a measure of the mean disturbance of the horizontal component of the geomagnetic field measured at the Earth's surface near the equator, in hourly values. Thus, it gives us the divergence, positive or negative, from the mean geomagnetic field value (during the 5 most undisturbed days of a year). During quiet days, the Dst index ranges from -20 nT to 20 nT, values we consider undisturbed.

During geomagnetic storms, the horizontal component of the geomagnetic field undergoes certain variations, as explained in the previous section, which are in turn present in the Dst values, as a measure of its disturbance (Figure 15).

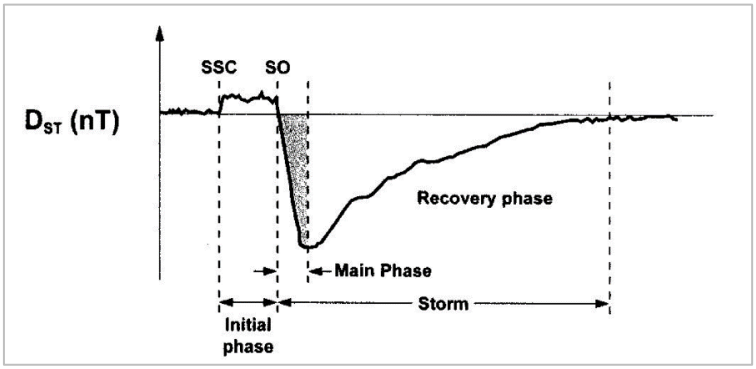

Figure 15 The Dst index profile during an isolated geomagnetic storm occurrence. [Kallenrode (2004)]

As these disturbances are clearly correlated with the behaviour of the ring current, the locations of the magnetic observatories that measure the geomagnetic field values and calculate the Dst index are selected: they are located near the equator (but avoiding the equatorial electrojets) and are almost evenly spaced around the Earth's perimeter (Hermanus, Kakioka, Honolulu, San Juan) (Figure 16).

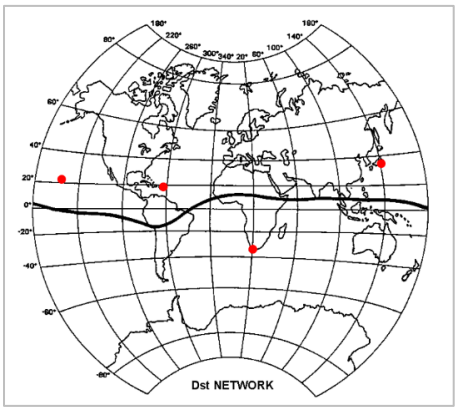

Figure 16 The locations of the magnetic observatories responsible for the extraction of the Dst index values. [WDC Kyoto, wdc.kugi.kyoto-u.ac.jp]

Another useful index is the one measuring the symmetric disturbances of the horizontal component of the geomagnetic field, or else the (SYMmetric-Horizontal) **SYM-H index**. It is similar to the Dst index, but has a time resolution of 1 second, when Dst has a 1-hour resolution. Also, the magnetic observatories responsible for the magnetic field measurements and the calculation of the SYM-H are more and in different locations (Figure 17). In this study, we use the SYM-H index, as a Dst index of higher resolution.

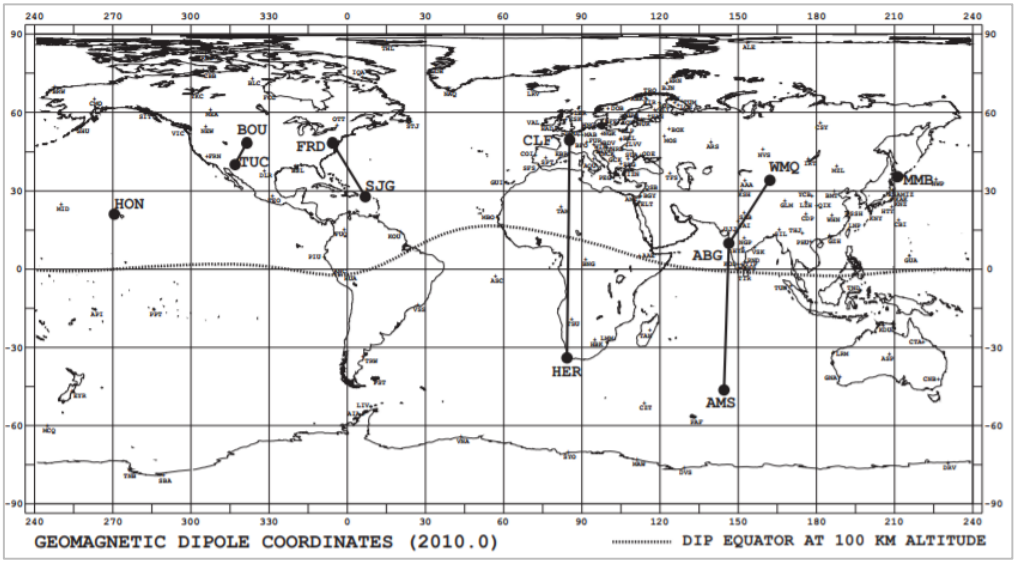

Figure 17 The locations of the magnetic observatories responsible for the extraction of the SYM-H index values. [WDC Kyoto, wdc.kugi.kyoto-u.ac.jp]

1.3.2 Magnetospheric substorms

i. Definition

A temporal disturbance of the terrestrial magnetosphere that lasts from a few minutes to a few hours is called a magnetospheric substorm. It is characterised by a large-scale rearrangement of the geomagnetic field and the magnetosphere, and also by the excitation of auroras at high latitudes. A necessary condition for a substorm to occur is that the solar wind or the interplanetary structure arriving at the dayside magnetopause should have a southward magnetic field, thus leading to enhanced magnetic reconnection and to energy transfer to the magnetosphere. Nevertheless, lower intensity substorm activity can also be exhibited following enhanced solar wind velocity, without any significant dayside reconnection. Typically one to four substorms occur per day.

ii. Phases

A magnetospheric substorm is divided in three phases:

- **Growth phase**: It begins with the dayside magnetic reconnection and is characterised by the accumulation of magnetic tension in the magnetotail, due to the magnetic and kinetic pressure of the solar wind.

- **Onset**: It begins after the magnetotail reaches saturation of stored magnetic tension, leading to magnetic reconnection happening at the magnetotail, as the northern and southern magnetospheric lobes come very close.

- **Expansion phase**: It begins with the magnetic reconnection at the magnetotail, which leads to a plasmoid (plasma bubble) being ejected to the night side. The remaining geomagnetic field then forcefully returns to its pre-disturbance state, due to the conservation of momentum injecting particles to the inner magnetosphere.

iii. Indices: AE, AU, AL

For the magnetospheric substorms, a useful index is the **Auroral Electrojet (AE) index**. It is measured in nanoTesla [nT] and is a measure of the global electrojet activity in the auroral zone. AE index is derived from variations of the horizontal component of the geomagnetic field measured on the Earth's surface near the auroral oval, every 2.5 minutes.

The upper and lower envelopes of all the measured variations are respectively defined as the **Auroral Upper (AU) index** and the **Auroral Lower (AL) index**, and their difference defines the AE index. AU and AL indices respectively express the strongest current intensity of the eastward and the westward electrojet, and AE index represents the total electrojet activity.

During magnetospheric substorms, the geomagnetic field undergoes serious rearrangements, affecting the particles , injecting them to the inner magnetosphere. Some can reach high latitudes and excite auroras or induce electric currents in the ionosphere (auroral electrojets) and in turn variations in the horizontal component of the geomagnetic field on the surface. Thus, the aforementioned indices are a good proxy for the study of substorms (Figure 18).

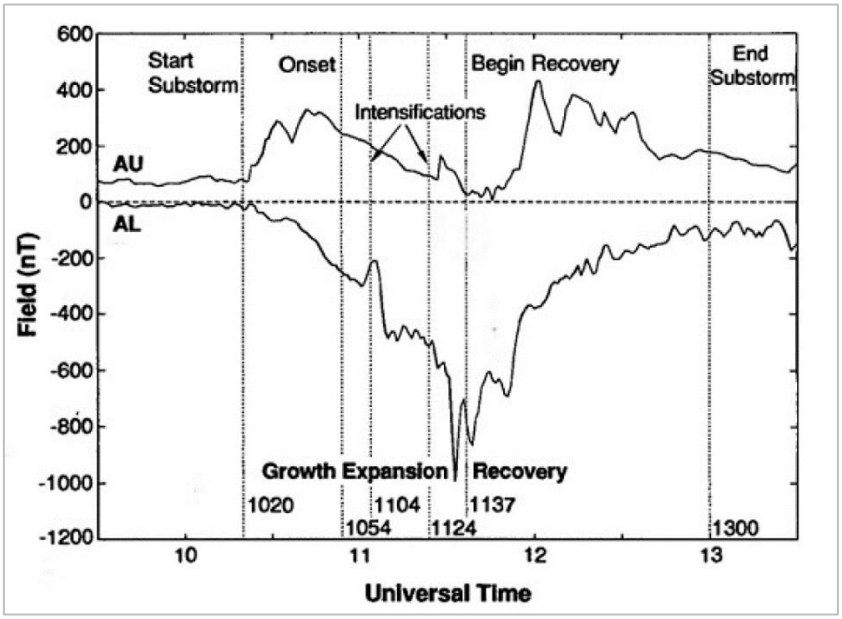

Figure 18 The AU and AL indices profile during an isolated magnetospheric substorm occurrence. [Kivelson & Russel (1995)]

1.4 Waves in geospace

Waves are an important aspect of magnetospheric activity, as they can propagate energy from one location to another. They can grow or decay and can either take energy out of a plasma or increase its energy.

In a normal fluid, only sound waves can occur. In a plasma, where more than one fluids are present, the possible wave types are more. In an unmagnetized plasma, electrostatic waves can occur (e.g. Langmuir waves, ion acoustic waves, electrostatic ion cyclotron waves). In a magnetized plasma, electromagnetic or magnetohydrodynamic (MHD) waves can occur (e.g. whistler-mode waves, Alfvén waves, magnetosonic waves).

These waves interact with the trapped magnetospheric populations via wave-particle interactions, playing a fundamental role in their dynamics, such as those of the outer radiation belt. In this study, we examine only whistler-mode chorus MHD waves (chorus waves) which result in gyro-resonant interactions, and Ultra Low Frequency MHD waves (ULF waves) which result in drift-resonant interactions.

1.4.1 Whistler-mode chorus waves (chorus waves)

Magnetospheric whistler-mode chorus waves are intense coherent electromagnetic emissions exhibiting discrete rising or falling tones in the magnetosphere. The frequency of chorus waves ranges over 0.1-0.8 f_{ce}, where f_{ce} is the equatorial electron cyclotron frequency (a few hundreds to a few thousand Hz), thus considered Very Low Frequency (VLF) waves. They are usually separated in two distinct frequency bands, the lower band (0.1-0.5 f_{ce}) and the upper band (0.5-0.8 f_{ce}).

Chorus waves are generated due to anisotropic angular distributions of 10-100 keV electrons which are injected near midnight from the plasma sheet, as a result of substorm activity. They are predominantly observed outside the plasmasphere, from pre-midnight to the afternoon sector, and their intensity strongly depends on geomagnetic activity. Lower-band chorus waves have a dual role, acting both as loss and acceleration processes for energetic electrons: they can lead to pitch angle scattering of >30 keV electrons and their precipitation in the atmosphere, but they can also lead to energy scattering of seed electrons and their stochastic local acceleration up to relativistic energies. For these reasons, the study of chorus waves, and specifically lower-band chorus waves, is fundamental for understanding the dynamics of the radiation belts.

In this study, we follow the technique presented by Li et al. [2013] and Ni et al. [2014] for inferring the chorus wave amplitude via precipitating electron fluxes measured by POES and MetOp satellites. These missions are comprised by low-altitude polar satellite constellations, meaning that they have a very extensive coverage of the precipitating fluxes, in L and MLT. By these measurements, and via a physics-based back-propagating technique, we can construct the spatiotemporal evolution of chorus wave intensity. The reason we use this technique over in situ measurements in the radiation belts, for example from Van Allen Probes mission, is that it provides a global indicator of chorus wave activity which cannot be obtained by empirical models or direct wave measurements, especially in cases where the apogee of the satellite is on the duskside, where chorus wave occurrence is typically low.

1.4.2 Ultra-Low Frequency waves (ULF waves)

Magnetospheric Ultra-Low Frequency waves exhibit a wide range of frequencies, from 1 mHz to 5 Hz. Depending on their waveform, they are called continuous pulsations (Pc, which are pseudo-sinusoidal) or irregular pulsations (Pi). Each group is divided in types depending on the frequency (Figure 19, Table 1).

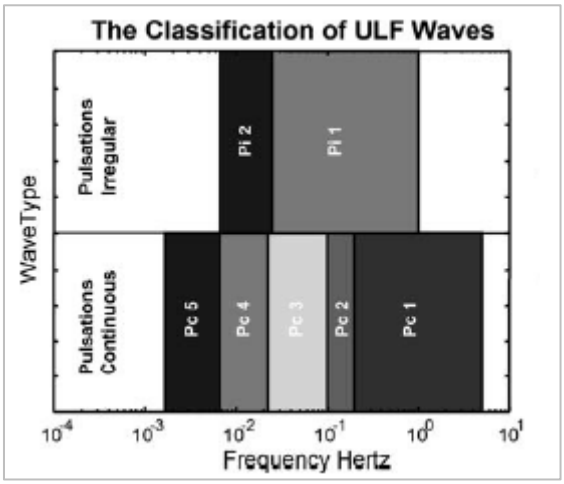

Figure 19 The different types of ULF waves. [McPherron (2005), Woodroffe (2010)].

Pulsations	f [mHz]	T [s]
Pc1	200-1000	0.2-5
Pc2	100-200	5-10
Pc3	22-100	10-45
Pc4	7-22	45-150
Pc5	1-7	150-1000
Pi1	25-1000	1-20
Pi2	1-25	20-1000

Table 1 The Oulu categorization of Ultra Low Frequency (ULF) waves.

ULF waves can be generated in the magnetosphere due to external and internal sources. The external sources refer to solar wind sources that can be divided into three distinct mechanisms: pulsations observed near the dawn and dusk flank magnetopause driven by the strong velocity shear present there, pulsations in the dayside driven by variations in the solar wind dynamic pressure, and pulsations driven by variations in the orientation and strength of the IMF. There are many proposed internal sources, some of which are wave-particle interactions and local reconfigurations of the magnetic field.

ULF waves are observed in all MLTs and their intensity strongly depends on geomagnetic activity. They have a dual role, acting both as loss and acceleration processes for electrons. They can lead to the violation of the third adiabatic invariant for relativistic electrons, causing radial diffusion, especially by the Pc4 and Pc5 waves. For these reasons, the study of ULF waves, and specifically Pc5 waves, is fundamental for understanding the dynamics of the radiation belts.

The detection of ULF waves can be accomplished by processing in situ magnetic field measurements in the radiation belts, for example from Van Allen Probes mission. The processing includes a Fourier or Wavelet transform, and a filtering to the desired frequencies. In this study we perform a Morlet Wavelet transform on magnetic field data from the Van Allen Probes, as presented by Balasis [2013], Katsavrias et al. [2019] and Nasi [2017], to infer the Pc5 wave amplitude and calculate their power.

ULF waves can also be divided in different wave modes (toroidal, poloidal) having different results in their electron interactions. In this study we only examine the total, global ULF Pc5 waves.

1.5 Electron Phase Space Density (PSD)

1.5.1 Energy spectrum

The energy spectrum of a particle population is the number of particles or intensity of a particle beam as a function of particle energy. In this study, the particles are electrons and information about them comes from the differential fluxes measured by the Van Allen Probes. So, the energy spectrum $j(E)$ is just the differential flux j in respect to the mean energy E of the detector channels.

If E_{min} , E_{max} correspond to the energy range of each channel, the center energy of each channel is:

$$E = \sqrt{E_{min}^2 E_{max}^2}$$

Because the energy channels are discreet, the flux is also discreet, but we can convert it to a continuous spectrum by selecting a proper fitting and calculating the fitting parameters. That way, we have a continuous energy spectrum $j(E)$ (in $[cm^{-2}s^{-1}sr^{-1}keV^{-1}]$ from the detectors we use).

1.5.2 Phase Space Density

i. Definition

A Phase Space is a space in which all possible states of a system are represented, with each possible state corresponding to one unique point in the phase space. For mechanical systems, the phase space usually consists of all possible values of position and momentum variables. The motion of an ensemble of systems in this space is studied by classical statistical mechanics.

The local density of points in such systems, called Phase Space Density (PSD), obeys Liouville's Theorem, and so can be taken as constant. Within the context of a model system in classical mechanics, the phase space coordinates of the system at any given time are composed of all the dynamic variables of the system. Because of this, it is possible to calculate the state of the system at any given time in the future or the past, through integration of Hamilton's or Lagrange's equations of motion.

ii. Application

Because of Liouville's Theorem, which dictates that PSD can be taken as a constant, we can use the PSD in radiation belt studies as it remains constant along a particle trajectory. That way, we can examine the development of the PSD to extract information about the particle trajectory and the physical mechanism that is responsible for its change.

So, calculating the PSD for certain values of the three adiabatic invariants μ, K, L* helps us track a specific particle population and determine if the adiabatic approximation is violated.

iii. Calculation

Inside the magnetosphere we use coordinates following the magnetic field lines, thus using the adiabatic invariants μ, K, L*. The invariant μ can be expressed as:

$$\mu = \frac{p_{\perp}^2}{B} = \frac{p^2 \sin^2(a)}{B}$$

Or for the relativistic case:

$$\mu = \frac{\epsilon(\epsilon + m_o c^2)\sin^2(a)}{2m_o c^2 B}$$

Thus, we can determine the energy solving this expression and accepting the positive solution, where $m_o c^2 = 0.511\ [MeV]$ for electrons:

$$\epsilon = -\frac{0.511}{2} + \frac{1}{2}\sqrt{(0.511)^2 + 8 \cdot 0.511 \cdot \mu \cdot B \cdot 10^{-5}/\sin^2(a)}$$

where $\epsilon\ [MeV], \mu\ \left[\frac{MeV}{G}\right], B\ [nT]\ (so\ B \cdot 10^{-5}\ [G])$.

In summary, and according to methods explained in later sections, the values of μ correspond to different energy ranges, as μ also depends on the magnetic field values. This way, it relates to different electron populations as well. For this study, and for simplicity:

μ [MeV/G]	$\epsilon\ [keV]$	e
1	1 – 10	Source
10	10 – 100	
50	50 – 400	Source/Seed
100	100 – 600	Seed
200	200 – 1000	Seed/Relativistic

Table 2 The values of the first adiabatic invariant μ and the corresponding electron energy values and electron populations. Table produced by the author, based on the results of later chapters, summarized in Table 9.

Last, using the continuous electron energy spectrum, meaning the differential electron fluxes with respect to the energy, $j(\epsilon)$, and with known values of μ and B, we can calculate the PSD with respect to the energy:

$$PSD(\epsilon) = 3.325 \cdot 10^{-8} \frac{j(\epsilon)}{\epsilon(\epsilon + 2m_o c^2)} \quad \left[\left(\frac{c}{MeV\ cm}\right)^3\right]$$

where the multiplying factor is used to convert its units to those shown in the bracket.

1.6 Radiation belt variability and wave particle interactions

As presented in the previous sections, we are interested in studying the variability of the electrons comprising the outer radiation belt. These electrons have a specific behaviour in quiet geomagnetic periods, but undergo different processes and exhibit variabilities in disturbed geomagnetic conditions. These are results of large-scale rearrangements of the geomagnetic field, or of breaking the conservation of the some of the three adiabatic invariants, as a result of wave-particle interactions, leading to energy scattering, pitch angle scattering or radial diffusion. These processes are also dependent on the geomagnetic activity, so this system is very complex. Of course, as shown by Reeves et al. [2003], geomagnetic storms can have different outcomes in the outer radiation belt behaviour: about 1/2 of the storms result in relativistic electron flux increase, 1/5 result in flux decrease, and 1/3 demonstrate no significant change in the flux (Figure 20).

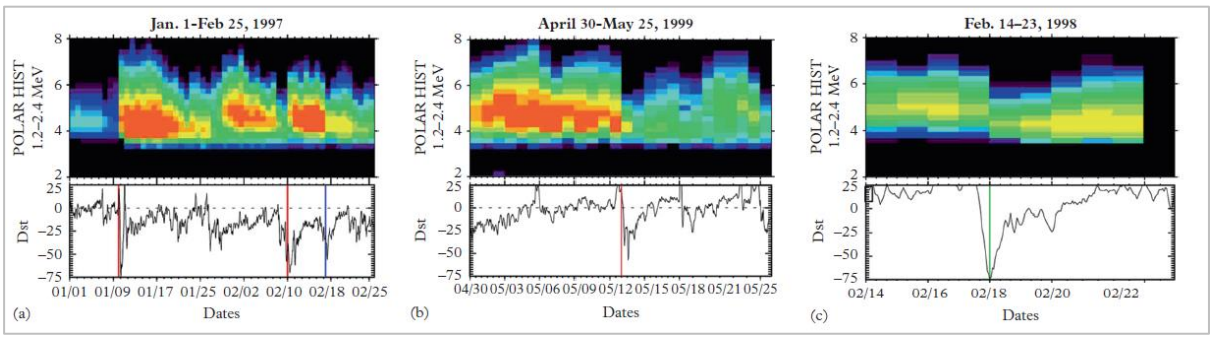

Figure 20 Examples of storms that (a) increased radiation belt fluxes, (b) decreased fluxes, and (c) left the belts relatively unchanged (less than a factor of 2 net change in flux). [Reeves et al. (2003)]

1.6.1 Sources

Electrons in the outer radiation belt come from two sources: the solar wind (~10s eV) and the ionosphere (~1 eV). Although, none of these source electrons have energies comparable to the energy of the electrons comprising the outer radiation belt, so an acceleration mechanism must be responsible for their energization up to 6-7 orders of magnitude.

1.6.2 Acceleration

The prerequisite for the electron acceleration is the violation of one or more adiabatic invariants. The theories explaining this acceleration are divided in two main categories: inward radial diffusion and in situ acceleration via wave-particle interactions (Figure 21).

Inward acceleration means that the third adiabatic invariant is violated, and thus, an electron moving inwards (towards stronger magnetic field) gains energy by conserving the first adiabatic invariant. These electrons can be source electrons (~10-100 keV), seed electrons (~100-500 keV) or relativistic electrons. In situ acceleration is achieved by gyro-resonant interactions between seed electrons and substorm generated chorus waves, accelerating them to relativistic energies, by violating the first and/or second adiabatic invariant.

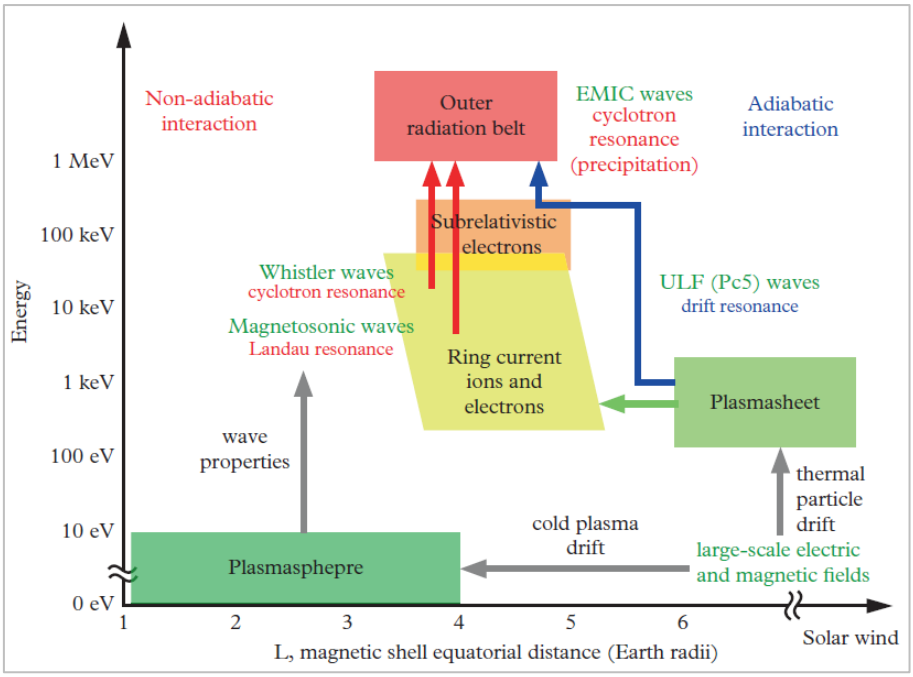

Figure 21 Diagram illustrating the relationship between magnetospheric regions, near-dc and wave fields, and acceleration and transport of electrons (slightly modified from Figure 2 of Miyoshi et al. (2012)). Domains in L and particle energy are shown by boxes, electromagnetic fields including waves are shown in green fonts, the processes that regulate the plasma domain and wave properties are shown by gray arrows, and electron acceleration/transport is shown by blue (adiabatic process) and red (non-adiabatic process) arrows. [Takahashi & Miyoshi (2016)]

1.6.3 Losses

Like the electron flux enhancements, flux decreases can also occur, either as a result of adiabatic effects (e.g. Dst effect), or as true losses due to precipitation into the atmosphere (by chorus or EMIC waves) and due to the combination of outward diffusion (driven by ULF waves) with magnetopause shadowing.

Atmospheric precipitation means that the second adiabatic invariant is violated, resulting in pitch angle scattering. Magnetopause shadowing means that particles are lost by drifting into the magnetopause, a phenomenon that can reach lower L-shells as the magnetopause is compressed due to high solar wind speed or pressure.

1.6.4 PSD response

When phase space density is plotted as a function of L*, thus giving a radial profile of its evolution, we can spot its response to these mechanisms. This is why the PSD is very useful in the study of the outer radiation belt, as it can present the mechanism responsible for its variability (Figure 22).

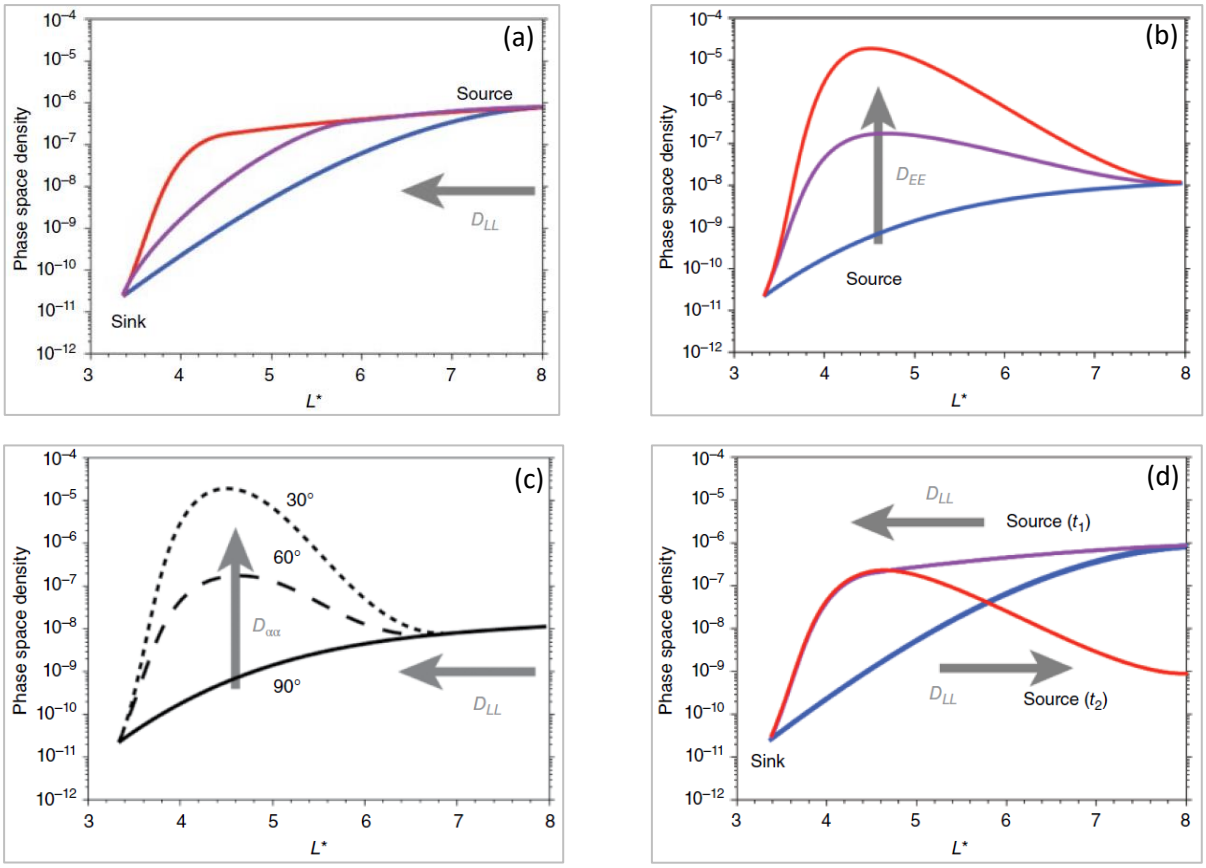

Figure 22 Schematics of the PSD response to different mechanisms [Reeves (2015)].
(a) Radial diffusion from a source region (the magnetotail) to a sink region (the slot). An increase in radial diffusion will increase the transport rate and increase the phase space densities in the heart of the outer radiation belt ($L^* \approx 4–5$).
(b) Local acceleration. Wave-particle interactions produce energy diffusion that accelerates electrons. In this case the source of the relativistic electrons is the local lower-energy electron population.
(c) The different radial profiles of phase space density that can be produced for different equatorial pitch angles (K values) through a combination of radial diffusion and localized pitch angle diffusion.
(d) How peaks can be formed by a combination of radial diffusion and a variable source at high L^*.

1.7 Instrumentation

In this study, we use Van Allen Probes data to calculate the electron PSD from electron flux data, and to calculate the Pc5 wave power from magnetic field data. We also use POES data to extract the chorus wave amplitudes from precipitating electron data from the POES mission.

For this reason, we use only two types of instruments: silicon solid-state detectors (SSD) for the electron fluxes, and fluxgate magnetometers (FGM) for the magnetic field.

i. Silicon Solid-State Detectors (SSD)

The principle of these detectors is based on the physical mechanism of energy loss when a particle interacts with mattes. Heavy charges particles, such as protons, interact with materials due to a series of collision with electrons, with each interaction leading to an energy loss with practically no scattering. As a result, protons continue on an approximately straight line and the energy spread loss is very small. On the other hand, electrons can lose a significant amount of energy and undergo significant scattering due to even one collision with an atomic nucleus.

SSDs are constructed with pure silicon crystals. There are various types of detectors according to the impurities and the method they are inserted in the lattice, yet everyone has the same principle. If a charged particle enters the crystal and interacts with the electrons of the valence band they are transferred to the conductive band. There electrons are free to move with response to the externally applied electric field. For each and every electron transported to the conductive band a hole is created at the valence band. The hole's behaviour is that of positive ion which moves also in response to the external electric field. Both electrons and holes are referred as carriers. The amount of energy needed for the generation of an electron – hole pair in silicon is approximately 3.6 eV. The crystals have electrodes at both their sides which act as reverse biased diodes. The externally applied electric field attracts the carriers to the corresponding electrode and prevents them from re-joining. The total charge collected at an electrode is proportional to the energy loss of the crystal due to its interaction with the particle. In case the particle is stopped by the crystal then the collected charge is proportional to the particle's energy. The electric current caused by the charge collection at the electron collector powers a pre–amplifier which converts it to a voltage pulse. Then this pulse powers a linear amplifier which shapes and amplifies the signal to create a short pulse with amplitude proportional to the collected charge. Of course further processing can be carried out using modern signal processing methods.

The advantages of SSD are the small size, the fine energy resolution, fast timing analysis (timing coincidence is possible in the order of nanoseconds) and the possibility to adjust the thickness of the crystal to match the measurement requirements. The disadvantages include the limitation to small thicknesses (<1mm), susceptibility to damage from light emission and the relatively high energy threshold (approximately 20 keV) for detecting the particles. The limitation on the thickness of the detector means that protons with energies greater than about 14 MeV will not stop at the detector. One way to measure higher energy particles is the organization of two or more silicon detectors, one after the other in an axial configuration (detector telescope).

ii. Fluxgate magnetometers (FGM)

The operation of these magnetometers is based on the principle of magnetic material saturation. A fluxgate magnetometer consists of a small, magnetically sensitive core, which is wrapped by two coils (Figure 23). An alternate current is passing through the first coil, traversing the coil in a cycle of alternate saturation magnetization (magnetized–non magnetized–reversed magnetized–non magnetized–magnetized). That constantly changing field induces an electric current at the second coil and the output current is measured by a detector. Inside a magnetically neutral environment, both the input and output currents will be equal but if the core is exposed to a background field (e.g. terrestrial magnetic field), it's easier to be magnetized in alignment with the environment field and the opposite.

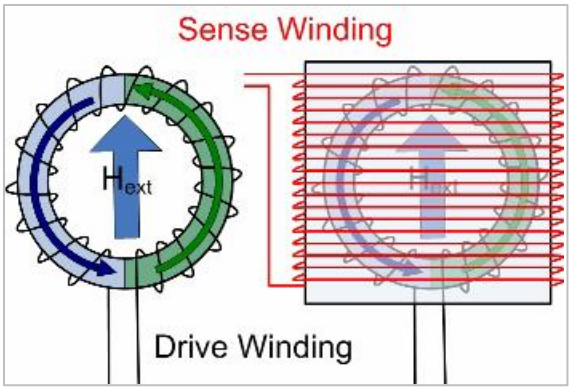

Figure 23 Illustration of a fluxgate magnetometer. A high permeability core is surrounded by a drive winding (black) and a sense winding (red). In this image there is an ambient external magnetic field H_{ext} [Space and Atmospheric Physics, ICL].

1.7.2 Van Allen Probes mission (VAP or RBSP)

The Van Allen Probes mission, previously known as the Radiation Belt Storm Probes (RBSP) mission, is conducted by NASA for the study of the radiation belts, as a part of the Living With a Star program. Its goal is to gain scientific understanding on how populations of electrons and ions in space form or change in response to changes in solar activity and the solar wind. The mission is comprised of two spin-stabilized spacecraft, called probes A and B, that were launched on 30 August 2012. The mission is still active, and the probes are projected to cease operations in early 2020.

The probes follow a near-equatorial elliptic orbit with 10.2° inclination, a period of approximately 9 hours, a perigee at 618 km and an apogee at nearly 30.000 km or 5.8 R_E.

It is vital that the two craft make identical measurements to observe changes in the radiation belts through both space and time, so each probe carries the following instruments, making them able to measure an enormous range of energies, particles and waves (Figure 24):

- Energetic particle, Composition and Thermal plasma (**ECT**) Instrument Suite
- Electric and Magnetic Field Instrument Suite and Integrated Science (**EMFISIS**)
- Electric Field and Waves instrument (EFW)
- Radiation Belt Storm Probes Ion Composition Experiment (RBSPICE)
- Relativistic Proton Spectrometer (RPS)

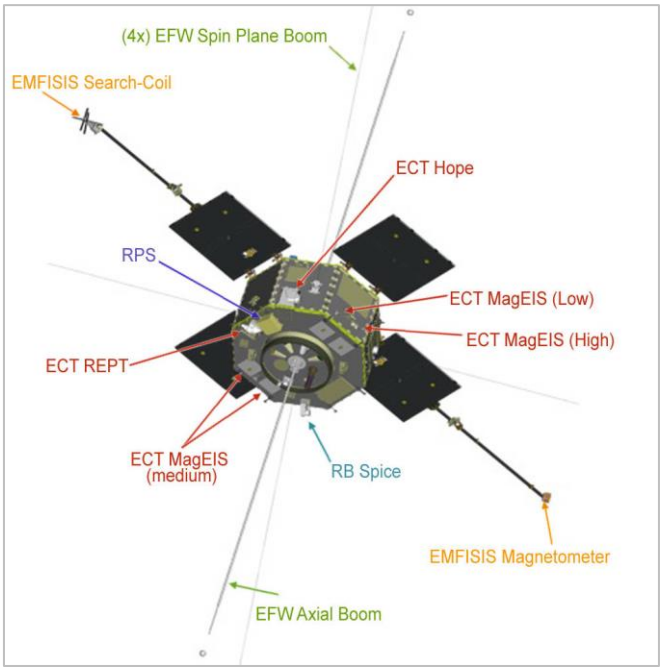

Figure 24 One of the Van Allen Probes with location of instruments indicated. [NASA, www.nasa.gov, JHU/APL]

In this study, we use measurements from two components of the ECT Suite, HOPE and MagEIS for the electron flux, and from the fluxgate magnetometer (FXG) of the EMFISIS for the magnetic field.

i. Helium Oxygen Proton Electron Mass Spectrometer (HOPE)

The HOPE instrument records helium, oxygen, protons, and electrons at lower energies and speeds. Such particles exist throughout the solar system, and play an important role in belt dynamics, since they can generate electromagnetic waves that can, in turn, affect the higher energy particles trapped in the belts. The HOPE instrument is a silicon Solid State Detector (SSD).

ii. Magnetic Electron Ion Spectrometer (MagEIS)

The MagEIS instrument observes electrons and ions in the middle energy ranges. Magnets inside the instrument deflect these particles towards the sensors, thereby differentiating them from the background radiation coming in from the belts. This will provide the cleanest measurements of radiation belt electrons so far achieved. Each RBSP spacecraft will carry four MagEIS instruments, each covering a separate part of the energy spectrum and a wide range of pitch angles. The MagEIS instrument is also a silicon SSD (Figure 25).

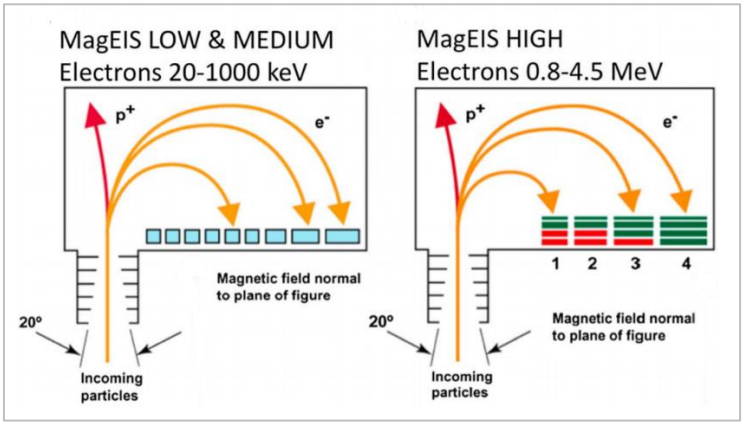

Figure 25 . Schematic diagrams showing MagEIS LOW/MEDIUM (left) and HIGH (right) units. [Fennel et al. (2016)]

iii. Fluxgate magnetometer (FXG)

The two probes carry fluxgate magnetometers which measure the magnetic field strength and vector with a resolution of 2 seconds. The fluxgate magnetometer of the EMFISIS is a wide-range, high performance triaxial fluxgate magnetometer system. It covers ambient fields from 0.008 nT to 65.536 nT.

1.7.3 Polar-orbiting Operational Environmental Satellite mission (POES) MetOp mission (MetOp)

The POES mission is conducted by NASA, ESA, NOAA and EUMETSAT with the intent of improving the accuracy and detail of weather analysis and forecasting. The mission is comprised of a constellation of satellites, the first of which was launched in April 1960, and the last in February 2009. The mission is still active, and the Joint Polar Satellite System (JPSS), which launched in November 2017, is the planned successor to the POES program. The satellites follow a polar orbit at a 520 miles altitude.

The MetOp mission is conducted by ESA and EUMETSAT, with the intent of providing numerical weather prediction models with high resolution global atmospheric temperature and humidity structure. The mission is comprised of three satellites, called A,B and C, launched in 2006, 2012 and 2018 respectively, and is planned to continue until 2021.

In order to provide data continuity between MetOp and POES satellites, several instruments are carried on both fleets of satellites:

- Advanced Microwave Sounding Units (AMSU-A1/AMSU-A2)
- High-resolution Infrared Radiation Sounder (HIRS/4)
- Advanced Very High-Resolution Radiometer (AVHRR/3)
- Advanced Data Collection System (A-DCS)
- Space Environment Monitor (**SEM-2**)
- Search And Rescue Processor (SARP-3)
- Search And Rescue Repeater (SARR)
- Microwave Humidity Sounder (MHS)

In this study, we use measurements from the SEM-2 monitor for the precipitating electron fluxes, in order to compute the chorus wave amplitudes, following the method presented by Li et al. [2013] and Ni et al. [2014].

i. Space Environment Monitor (SEM-2)

Measurements of Earth's radiation belts and charged particle fluxes at satellite altitude. Provide awareness of solar and terrestrial anomalies and warnings of solar wind occurrences that may damage or impair satellite functionality.

SEM consists of two solid state detectors each one with a 30^{o} field of view: the Total Electron Detector (TED), which measures proton and low energy electron fluxes (60 eV – 16 keV), and the Medium Energy Proton and Electron Detector (MEPED) which measures higher energy electron fluxes (30 keV – 140 MeV). These detectors measure particles at two directions: an almost parallel (0^{o} telescope) and one perpendicular (90^{o} telescope) to the local magnetic field direction. This way, the 0^{o} telescope is ideal for precipitated particle measurements while the 90^{o} telescope is ideal for trapped particles in the terrestrial magnetosphere. Unfortunately, these detectors have significant proton contamination in the electron channels, therefore we only use processed data using the method introduced by Lam et al. [2010].

Chapter 2: Event and data selection

Our goal is to examine the relationship between source electrons, seed electrons, chorus waves and ULF waves. What we expect is that following a substorm, source and seed electrons are injected to the inner magnetosphere, emitting chorus waves and increasing their energy. These seed electrons interact with the emitted chorus waves finally becoming relativistic electrons. For this reason, we will examine electron fluxes of energies corresponding to source (~10s keV) and seed (~100s keV) electrons, chorus wave amplitude and Pc5 wave power, for geomagnetic disturbance events that either result to enhancement or depletion of relativistic electrons. We will examine the electron Phase Space Density (PSD) to see how the electron populations evolve over time, because the way the PSD changes reflects the physical mechanisms responsible.

This study is based on the study of Katsavrias et al. [2019]. Katsavrias et al. created a list of 71 events with certain characteristics, examined only seed (μ=100 [MeV/G]), relativistic (μ=900 [MeV/G]) and ultra-relativistic (μ=4200 [MeV/G]) electrons, and finally divided the events into three categories, resulting either in enhancement, depletion or no change of the studied relativistic electron PSD. However, the present study examines only events resulting in enhancement or depletion, and only source and seed electrons, in order to see how they affect the behaviour and the results of those studied by Katsavrias et al.

2.1 Events

We are interested in using Van Allen Probes (RBSP) data for examining the electron populations, because of the high-quality pitch angle distributions of both the MagEIS and HOPE instruments, so we are confined to events happening after 2012, when the RBSP mission is active. The events we examine cover the period from 2013 to 2017 and are chosen based on the work of Katsavrias et al. [2019], meaning that we only study the selected 20 and 8 events that result in enhancement or depletion of the average relativistic electron PSD, respectively.

2.1.1 Disturbance type

The events are geospace disturbances, meaning both storm and non-storm events, that can have either an ICME or an SIR as a driver. The indices we examine for selecting an event is AL index, because we are interested in substorms and their effect on electrons, and the SYM-H index, to categorize storm events. The event intensities vary from weak to severe, and their duration from 5 to 9 days, based on the time that the solar wind conditions return to the pre-disturbance levels.

2.1.2 Characteristics / Preconditioning

We need a clear identification of each event and driver, so we need quiet pre-disturbance conditions. We selected events that emerge after at least 12 hours of quiet-time conditions, meaning that the following criteria are satisfied:

- Solar wind velocity: $V_{SW} < 400$ [km/s]
- Solar wind dynamic pressure: $P_{SW} < 3$ [nPa]
- SYM-H index: SYM-H > -20 [nT]
- AL index: AL > -300 [nT]
- z-component of IMF: -5 [nT] < B_z < 5 [nT]

Here is an example (Figure 26) of a selected event (27 Feb – 5 Mar, 2013) using solar wind and magnetospheric parameters and indices, whose properties are explained in the following sections. It is clear that the disturbance emerges after at least 12 hours of quiet-time conditions, that satisfy the above criteria. These plots will not be presented for each one of the events, but all the mentioned parameters are used and plotted later in a superposed epoch analysis.

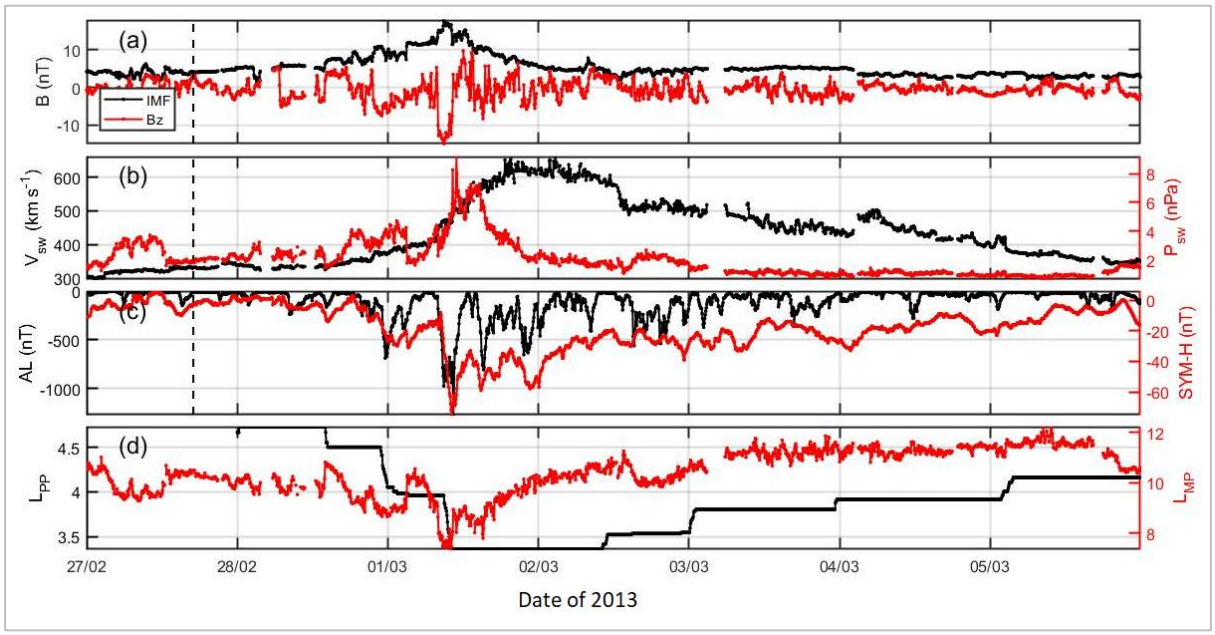

Figure 26 Evolution of solar wind properties, magnetospheric properties and indices for an example of a selected event, here for 27 Feb – 5 Mar, 2013. Top to bottom: (a) black: Interplanetary Magnetic Field IMF [nT], red: its horizontal component Bz [nT], (b) black: solar wind velocity V_{SW} [km/s], red: solar wind dynamic pressure P_{SW} [nPa], (c) black: AL index [nT], red: SYM-H index [nT], (d) black: average location of the plasmapause L_{PP} [R_E] based on O'Brien et al. [2003], red: location of the dayside magnetopause L_{MP} [R_E] based on Shue et al. [1988]. All quantities are further explained in the previous and following sections. Figure produced in MATLAB by the author.

2.1.3 Event categories

We separated the events in two categories depending on the resulting enhancement or depletion of the average relativistic electron (μ=900 [MeV/G]) PSD post-event (the average PSD during 24-72h after the maximum compression of the magnetopause according to Katsavrias et al. [2019]) comparing to pre-event (24-48h before), for L*>4.5:

- **Enhancement** Events:

$$\log_{10}(PSD_{pre}) - \log_{10}(PSD_{post}) \leq -\log_{10}(6) \quad \rightarrow \quad \boldsymbol{PSD_{post}/PSD_{pre} \geq 6}$$

- **Depletion** Events:

$$\log_{10}(PSD_{pre}) - \log_{10}(PSD_{post}) \geq \log_{10}(4) \quad \rightarrow \quad \boldsymbol{PSD_{post}/PSD_{pre} \leq 1/4}$$

where the $\log_{10}(4)$ and $-\log_{10}(6)$ values where selected as they correspond to the average logarithmic PSD evolution for the events studied by Katsavrias et al [2019]. The rest of the events are considered resulting in no significant change of relativistic electrons. The use of average PSD and not its maximum value allows us to neglect intermittent and short-term variations.

For our study, this separation may sound irrelevant, as it refers to relativistic electrons, but we keep the events organised this way to check if there really is a clear pattern on source and seed electron evolution based on the resulting relativistic enhancement.

Here is an example (Figure 27) of the behaviour of the average PSD for relativistic electrons of μ=900 [MeV/G] at L*=4.5 and L*=5, for enhancement and depletion events, as studied by Katsavrias et al. [2019]. It is clear that the PSD value difference between the pre- and post-event phases follows the aforementioned pattern. The properties of the figures are explained in detail in later sections.

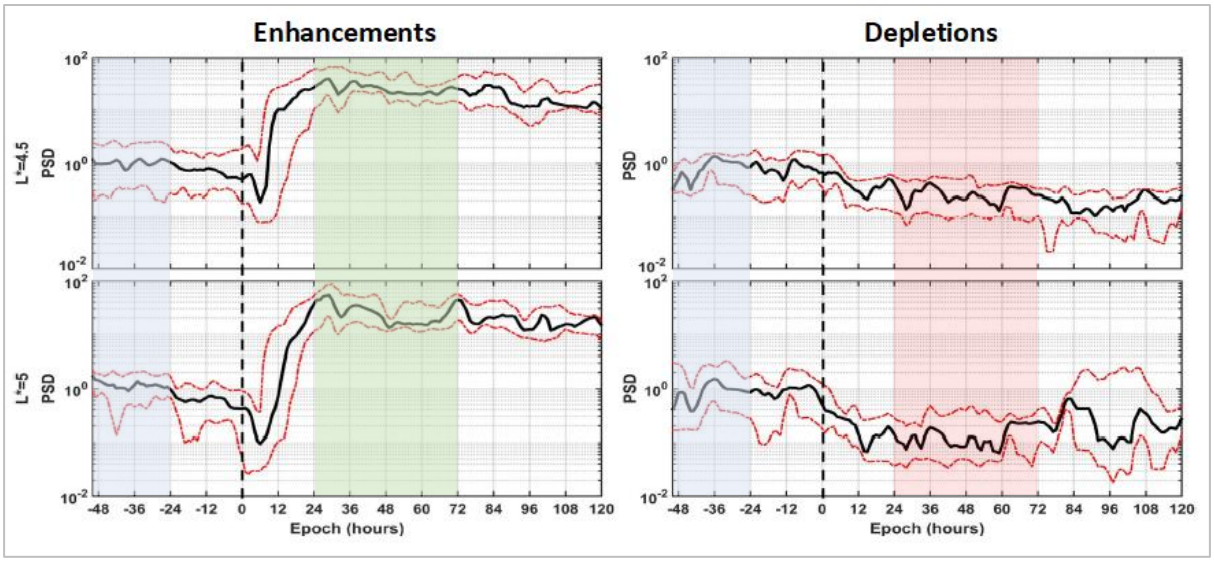

Figure 27 Evolution of the average PSD [(c·MeV^{-1}·cm^{-1})^3] for relativistic electrons of μ=900 [MeV/G] at the regions of L=4.5 and L*=5, for enhancement and depletion events, as studied by Katsavrias et al. [2019]. Although the PSD values are comparable in the pre-event phase (24-28h before 0h) in the two event categories, it is clear that post-event (24-72h after 0h), in enhancement events the PSD shows an increase larger than 1 order of magnitude, but in depletion events it only appears to decrease, thus explaining the characterisation of the event categories. The time of Epoch=0h corresponds to the time of the maximum compression of the magnetopause, which is different to the key time that we use in this study. Figure by Katsavrias et al. [2019]. The solid black line is the median, and the red lines are the 25% and 75% quantiles, all further explained in later sections.*

2.1.4 Final list of events

The selected 28 events are the following, 20 resulting in enhancement and 8 in depletion of the average relativistic electron PSD. The key time t_0 is used in the Superposed Epoch Analysis, corresponds to the start time of continuous substorm activity as indicated by the decrease of AL index, and its selection will be covered in later sections.

	t_i	t_f	t_0	Duration [days]	AL_{min} [nT]	SYM-H_{min} [nT]	Resulting in relativistic e …	#
2013	27 Feb	3 Mar	28 Feb 19:15	7	-1271	-75	Enhancement	1
	12 Apr	16 Apr	13 Apr 01:16	5	-292	-18	Depletion	2
	22 Apr	29 Apr	23 Apr 20:20	8	-1105	-52	Enhancement	3
	24 Jul	30 Jul	25 Jul 15:54	7	-573	-25	Depletion	4
	2 Aug	8 Aug	3 Aug 20:50	7	-736	-55	Enhancement	5
	16 Sep	22 Sep	18 Sep 14:46	7	-1086	-30	Enhancement	6
	30 Sep	6 Oct	1 Oct 13:06	7	-1596	-87	Enhancement	7
	14 Nov	21 Nov	15 Nov 14:10	8	-668	-42	Depletion	8
	6 Dec	12 Dec	7 Dec 18:20	7	-955	-72	Enhancement	9
	12 Dec	18 Dec	13 Dec 23:58	7	-661	-42	Depletion	10
2014	5 Feb	13 Feb	6 Feb 02:50	9	-931	-40	Enhancement	11
	6 Jun	13 Jun	7 Jun 12:26	8	-1225	-71	Enhancement	12
	10 Sep	16 Sep	10 Sep 16:21	8	-1130	-95	Depletion	13
2015	15 Mar	21 Mar	17 Mar 05:35	7	-2030	-233	Enhancement	14
	8 Apr	13 Apr	9 Apr 02:21	6	-935	-88	Enhancement	15
	2 Nov	6 Nov	2 Nov 13:15	5	-1648	-66	Enhancement	16
2016	5 Mar	10 Mar	6 Mar 11:45	6	-974	-109	Enhancement	17
	6 Apr	10 Apr	7 Apr 15:40	5	-1007	-67	Depletion	18
	11 Apr	15 Apr	11 Apr 12:05	5	-948	-69	Enhancement	19
	18 Jul	24 Jul	19 Jul 23:19	7	-907	-33	Depletion	20
	18 Sep	24 Sep	19 Sep 05:55	7	-650	-38	Enhancement	21
2017	15 Jun	21 Jun	16 Jun 04:53	7	-782	-38	Enhancement	22
	7 Jul	14 Jul	8 Jul 23:19	8	-858	-37	Enhancement	23
	2 Aug	8 Aug	3 Aug 14:00	8	-973	-34	Enhancement	24
	6 Nov	13 Nov	7 Nov 03:30	8	-1331	-89	Enhancement	25
	3 Dec	10 Dec	4 Dec 04:51	8	-1081	-46	Enhancement	26
	14 Dec	22 Dec	17 Dec 04:05	9	-922	-33	Enhancement	27
	22 Dec	29 Dec	24 Dec 09:28	8	-686	-30	Depletion	28

Table 3 The events selected for this study, based on the Table 4.2 and Table 4.3 from the study of Katsavrias (2019). t_i is the start date of the event, t_f is the final date of the event, and t_0 is the selected key time for the superposed epoch analysis, selected as the start time of continuous substorm activity based on AL index, and the method is covered in later sections. Also noted are the duration of each event, the minimum values of SYM-H and AL indices, the result considering the relativistic electrons, and an index number. Table produced by the author.

2.2 Solar wind and geomagnetic indices data

The properties of the solar wind are all determined from the NASA Coordinated Data Analysis Web (cdaweb.sci.gsfc.nasa.gov) OMNI data, meaning high resolution measurements from ACE spacecraft located at L1 point. High (1-min and 5-min) resolution OMNI data contain solar wind magnetic field and plasma data at Earth's bow shock nose, and geomagnetic activity indices. Their 5-min resolution is derived from 1-min data with added 5-min energetic proton fluxes. We download them from the official site: https://omniweb.gsfc.nasa.gov/ in csv format, each file corresponding to one year.

For our study, we use the data about the interplanetary magnetic field IMF, its horizontal component Bz, the solar wind velocity and dynamic pressure V_{SW} and P_{SW}, the geomagnetic indices AL and SYM-H, and we also calculate the dayside magnetopause position L_{MP} and the average location of the plasmapause L_{PP}, based on the models by Shue et al. [1998] and O'Brien and Moldwin [2003] respectively. We use these data, fold them around the selected key time t_0 and depict their evolution for enhancement and depletion events.

2.3 Electron data

All electron data we use are RBSP mission measurements, but from different instruments depending on the electron energy, from 1 keV to 10^3 keV (1 MeV):

Instrument	HOPE	MagEIS
Electrons	Source e	Source e, Seed e, Relativistic e
Energies	1 - 30 keV	30 - 10^3 keV
Channels	1 - 31	32 - 44

Table 4 The electron populations, electron energies and detector channels that correspond to each of the HOPE and MagEIS instruments, covering 1 keV to 1 MeV. Table produced by the author.

2.3.1 Source electrons

HOPE instrument on board the RBSP probes provide the source electron (1-30 keV out of 1-100 keV) data. We download the level 3 data from the official site (https://www.rbsp-ect.lanl.gov/science/DataDirectories.php/) in cdf format. They contain information of the epoch, the differential flux, the channel energy, L, L*, and MLT, every 23 seconds. We use data from 31 of its 72 channels, corresponding to 0.933-29.1680 keV, and referring to pitch angles 36°, 54°, 72°, 90°, 108°, 126°, 144°.

We use these data to export the source electron differential fluxes for every pitch angle, calculate the PSD and the magnetic ephemeris. We fold them around the selected key time t_0 and depict their evolution for enhancement and depletion events.

2.3.2 Source, Seed and Relativistic electrons

MagEIS instrument on board the RBSP probes provide the rest of the source electron (30-100 keV out of 1-100 keV) data, plus the seed electron (100-500 keV) and relativistic electron (500-1000 keV) data. We download the level 3 data from the official site (https://www.rbsp-ect.lanl.gov/science/DataDirectories.php/) in cdf format. They contain information of the epoch, the differential flux, the channel energy, L, L*, and MLT, every 11 seconds. We use data from 13 of its 23 channels, corresponding to 33-909 keV, and referring to pitch angles 41 °, 57 °, 74 °, 90 °, 106 °, 123 °, 139 °. We assume that the MagEIS and HOPE pitch angles are in agreement, as the instruments have an $\pm 15^{o}$ opening.

We use these data to export the seed electron fluxes for every pitch angle, calculate the PSD and the magnetic ephemeris. We fold them around the selected key time t_0 and depict their evolution for enhancement and depletion events.

2.4 Wave data

Our information about the chorus waves and the ULF waves are extracted in different ways.

2.4.1 ULF waves

For the ULF Pc5 waves we use RBSP data, meaning the magnetic ephemeris in mat format we extract from them. We use the magnetic field measurements, filter them for the frequencies we need (2-7 mHz for the Pc5 waves), perform wavelet analysis to calculate the wave amplitude and power, and finally fold them around the selected key time t_0 and depict their evolution for enhancement and depletion events.

2.4.2 Chorus waves

For the chorus waves we use POES data, that can be downloaded from the official site: https://www.ngdc.noaa.gov/stp/satellite/poes/dataaccess.html. They contain energetic particle measurements at polar-orbit altitude, meaning the flux of energetic ions and electrons at the altitude of the satellite. From these fluxes information about chorus waves can be extracted, following the method presented by Li et al. [2013] and Ni et al. [2014].

The original POES data where manipulated by Li to infer the chorus wave amplitude, and we acquired the produced data in txt format. They contain information about the time and the chorus wave amplitude in pT, in 10 L-shell bins from L=3 to L=8.

We use these produced data to load the chorus wave amplitude, fold it around the selected time t_0 and depict its evolution for enhancement and depletion events.

2.5 Summary of our methodology

We examine the electron PSD (RBSP data) evolution in time depending on the solar wind conditions and magnetospheric parameters (OMNI data), the chorus wave amplitude (POES data), and the Pc5 wave power (RBSP data). We acquire the desired data, and process them in Matlab environment to clean them, interpolate them, calculate the fluxes, the PSD, the magnetic ephemeris, the wave properties, etc. Then we fold them around a key time t_0 performing a superposed epoch analysis, in order to compare the characteristics of the two event categories, resulting in enhancement or depletion of the relativistic electron fluxes.

2.6 Why use Matlab

The Matlab software (MATrix LABoratory) is a computing environment and programming language used for numerical and symbolic computing (with specific toolboxes) that allows matrix manipulations, plotting of functions and data, implementation of algorithms, etc. It is developed by MathWorks (www.mathworks.com) and is regularly updated to new versions or with new toolboxes. It has great plotting abilities and is equipped with many functions.

We use Matlab to process our data for this study, because it can open and read large data files, can convert them or compute different quantities in a relatively small running time. Also, it is a useful tool in portraying our results in a way that can be read and understood clearly.

The National and Kapodistrian University of Athens provides the Matlab software to all its students free of charge, through its Computer Center (www.cc.uoa.gr). The most recent version is R2018b.

We use Matlab to read our data files, export the electron fluxes and magnetic ephemeris, compute the PSD, perform the superposed epoch analysis, and depict the solar wind parameters, PSD, and wave evolution around the selected time t_0. The scripts and functions we use will be presented in later sections.

Chapter 3: Data processing

In this chapter we present the way we processed the acquired data in order to calculate all the physical quantities we are interested in studying. In our *Documents > MATLAB folder*, we have three main folders for this study:

- *Data folder*, containing the downloaded RBSP data.
- *Events folder*, with 28 *event subfolders*, containing the extracted fluxes, the extracted channel energy, the magnetic ephemeris, the calculated PSD, the downloaded OMNI data, the POES data, the extracted chorus wave amplitude, and all the matlab scripts and functions we used.
- *Epoch folder*, containing the extracted ULF wave amplitude and power, all the above epoch folded quantities for enhancement and depletion events, the scripts and functions we used and the final plots.

The OMNI data containing the solar wind parameters and geomagnetic indices, as well as the txt data extracted from POES data containing the chorus wave amplitude, do not need any extra processing before depicting, except performing the superposed epoch analysis. So, they are located in the event subfolders and are ready for plotting.

The RBSP data from the HOPE and MagEIS instruments are located in the data folder, but need some processing to calculate the magnetic ephemeris, the electron fluxes, the PSD, and the ULF wave amplitude, before performing the superposed epoch analysis and plotting them.

3.1 Magnetic ephemeris and electron fluxes

The RBSP data from HOPE and MagEIS instruments contain information about the probe positions and the electron fluxes:

	HOPE		**MagEIS**	
	Quantity name	Units	Quantity name	Units
Time (**T**)	Epoch_Ele	-	Epoch	-
Flux (**FEDU**)	FEDU	$cm^{-2}s^{-1}sr^{-1}keV^{-1}$	FEDU_CORR	$cm^{-2}s^{-1}sr^{-1}keV^{-1}$
Channel Energy (**Ech_RBSP**)	HOPE_ENERGY_Ele	eV	FEDU_Energy	keV
L	L_Ele	-	L	-
L*	L_star_Ele	-	L_star	-
MLT	MLT_Ele	hours	MLT	hours
Resolution	23 sec		11 sec	
Pitch Angles	4.5°, 18°, 36°, 54°, 72°, 90°, 108°, 126°, 144°, 162°, 175.5°		41°, 57°, 74°, 90°, 106°, 123°, 139°	

Table 5 The data properties from HOPE and MagEIS instruments: the physical quantity, and its recorded name and units. Table produced by the author.

We organised the data files in the event subfolders, and created Matlab scripts (*cdfread, HOPE_fluxes, MagEIS_fluxes*) to load them, read them, separate their contents and create matlab files for later use:

- Four files containing all info (T, L*, MLT, Ech_RBSP) as magnetic ephemeris for HOPE and MagEIS, for probe A and B
- Twenty-eight files containing the electron fluxes (FEDU) for HOPE and MagEIS, for probe A and B, and for seven pitch angles values, 41°-139°

The energy channels are different in the two instruments, and we want to use specific channels from each one. In summary:

E=1 keV  E=10^3 keV

Instrument	**HOPE**	**MagEIS**
Electrons	Source e	Source e, Seed e, Relativistic e
Energies	1 - 30 keV	30 - 10^3 keV
Channels	1 - 31	32 - 44

Table 6 (Table 4) The electron populations, electron energies and detector channels that correspond to each of the HOPE and MagEIS instruments, covering 1 keV to 1 MeV. Table produced by the author.

HOPE						**MagEIS**		
Energy [keV]	Real channel	Selected now as channel	Energy [keV]	Real channel	Selected now as channel	Energy [keV]	Real channel	Selected now as channel
0.9333	37	1	5.8516	53	17	33	1	32
1.0467	38	2	6.5631	54	18	54	2	33
1.1739	39	3	7.3611	55	19	80	3	34
1.3167	40	4	8.2560	56	20	108	4	35
1.4768	41	5	9.2598	57	21	143	5	36
1.6563	42	6	10.3856	58	22	184	6	37
1.8577	43	7	11.6483	59	23	226	7	38
2.0836	44	8	13.0645	60	24	235	8	39
2.3369	45	9	14.6529	61	25	346	9	40
2.6210	46	10	16.4344	62	26	470	10	41
2.9396	47	11	18.4325	63	27	597	11	42
3.2970	48	12	20.6735	64	28	749	12	43
3.6979	49	13	23.1870	65	29	909	13	44
4.1475	50	14	26.0061	66	30			
4.6518	51	15	29.1680	67	31			
5.2173	52	16						

Table 7 The mean energy of each detector channel, for HOPE and MagEIS instruments, together with its corresponding index number, as intended and as used in this study. Table produced by the author.

Now the magnetic ephemeris and electron fluxes are in the event subfolders and are ready to be used for calculating the PSD, detecting the ULF waves, and then performing a superposed epoch analysis and plotting all of the above.

3.2 PSD Calculation

To this point, every event subfolder contains the original data, the solar wind parameters, the magnetic ephemeris (T, L*, MLT, Ech_RBSP) and the electron fluxes. We created Matlab scripts (*PhaseSpaceDensity_''probe''_''pitch angle''*) to calculate the electron Phase Space Density (PSD), according to the previous chapters. The process followed in order to convert differential fluxes to PSD is based on Chen et al. [2005] and Turner and Li [2008].

3.2.1 For pitch angle α=90°

i. Collecting the Flux

For probes A and B, and for the equatorial electrons, the scripts (*PhaseSpaceDensity_A_90, PhaseSpaceDensity_B_90*) load the magnetic ephemeris, the 90° flux, the channel energies, keep measurements with flux > 3 [$cm^{-2}s^{-1}sr^{-1}keV^{-1}$], interpolate the HOPE and MagEIS fluxes to have the same time resolution (23 sec), smooth the flux every 5 minutes, calculate the mean flux every 5 minutes, and create a new flux variant containing continuous fluxes from HOPE and MagEIS keeping only the desired 44 energy channels back to back.

ii. Plotting the Flux-Energy spectrum and fitting

Then, the scripts create a logarithmic plot of the flux in respect to the channel energies, which forms a discreet spectrum as the energy channels and the flux measurements are discreet. We want to turn the discreet spectrum into a continuous one, in order to use it in the calculation of the PSD. So, we use the plots to select a matching fit for the data and use the fit as a continuous flux spectrum for calculating the PSD.

Checking the plots for different events, and after some trials, we finally selected the fit for five groups of channels (channels 1-22 and 23-31 corresponding to HOPE, and channels 32-35, 35-41, 41-44 corresponding to MagEIS):

- Power law $y = ax^b$ for the MagEIS measurements of source, seed and relativistic electrons, so in the log-log plot it is written as:

$$\log(y) = \log(ax^b) \;\rightarrow\; \log(y) = \log(a) + b\log(x) \;\rightarrow\; \log(y) = b\log(x) + c$$

- 3rd degree polynomial $y = ax^3 + bx^2 + cx + d$ for the HOPE measurements of source electrons, so in the log-log plot it is written as:

$$\log(y) = \log(ax^3 + bx^2 + cx + d)$$

The fitting parameters are determined in a least-square sense using a Levenberg-Marquardt method (Levenberg [1944], Marquardt [1963]) which is one of the most widely used optimization methods in solving non-linear curve fitting problems. This way we can compute all the fitting parameters and create a continuous flux spectrum in respect to the energy.

iii. Magnetic Field

Later, the scripts load the magnetic field B from the FXG data, create two files containing the magnetic field measurements, and interpolate the magnetic field for later use.

iv. Energy and PSD

Using the parameters of the continuous flux fitting and the interpolated B, and for selected values of the first adiabatic invariant μ=1, 10, 50, 100, 200 [MeV/G], the scripts can now calculate the electron energy and the PSD in respect to μ, and then create two files containing the PSD for pitch angle 90°, for probes A and B.

v. Magnetic ephemeris

Last, the scripts load the magnetic coordinates data and compute the magnetic ephemeris, containing the time T, the interpolated equatorial magnetic field B_{eq}, and the parameters and adiabatic invariants L, L* and K, and create two files containing them, for probes A and B. All values of the invariants K and L* are obtained from the magnetic ephemeris of ECT suite which are calculated using the Tsyganenko and Sitnov [2005] magnetospheric field model (TS05).

3.2.2 For the rest of the pitch angles

We follow the same steps for probes A and B and for the rest of the pitch angles in other scripts (*PhaseSpaceDensity_A_41, PhaseSpaceDensity_A_57, … , PhaseSpaceDensity_B_41, …*) collecting the flux, calculating the fit parameters, the electron energy and the PSD, creating twelve more files containing the PSD, for probes A and B, and for pitch angles 41°, 57°, 74°, 106°, 123°, 139°. We don't need to calculate the magnetic ephemeris as we did it for the 90° PSD for each probe.

3.2.3 K-binning

We create a script (*find_eph*) that loads every PSD file, the magnetic field B and the magnetic ephemeris we calculated, computes the equatorial pitch angle α_{eq}, bins the PSD in respect to α_{eq}, then matches the K,L and L* values with the binning, finally bins the PSD in respect to K and creates two new PSD files with K binning, for probes A and B.

Now the PSD for all pitch angles is in the event subfolders and is ready for performing a superposed epoch analysis and plotting.

3.3 Adiabatic invariant values

In order to calculate the electron PSD for certain electron populations, we need to assign specific values to the three adiabatic invariants, or at least assign narrow value ranges.

3.3.1 L* values

This study is concentrated on the outer radiation belt, which covers the region of L=3-6, so we only examine three magnetospheric regions, corresponding to **L*=3-4**, **L*=4-5** and **L*=5-6**. The same binning is used for L, as in these regions we consider the two parameters equal.

3.3.2 K values

We examine only near-equatorial mirroring electrons, corresponding to **K < 0.03 [$G^{1/2}R_E$]**. This means that the magnetic field line length that the electrons cover is very short, making them bounce very close to the equatorial plane, leading to a motion that mostly consists of gyration around the field lines and drifting around the Earth, thus trapping them in toroidal formations (the radiation belts).

3.3.3 μ values

In this study we use μ values corresponding to source, seed and relativistic electrons, for the regions of L*=3-6 and for K<0.03 [$G^{1/2}R_E$], depending on calculations presented in previous sections. The electron energy depends on the values of μ and B. Although in this study we consider fixed values of **μ=1, 10, 50, 100, 200 [MeV/G]**, the value of the magnetic field B is not only different at each region of L*=3-4, 4-5, 5-6, but also changes further depending on the magnetospheric conditions, for example storms and substorms that can distort its geometry. This leads to each μ value corresponding to different electron energies, and thus different electron populations, for each region, and for disturbed or undisturbed magnetospheric conditions.

During the PSD calculation, we also calculated the energy for fixed values of μ. We use these data to plot the energy corresponding to each μ value, to correlate it with the electron populations.

What follows is an example of the different range of energies in this study, for three cases of random events which where selected as examples of weak ($AL_{min}\approx$ -300 nT), intense ($AL_{min}\approx$ -1000 nT) and severe ($AL_{min}\approx$ -2000 nT) magnetic field reconfigurations based on the minimum value of AL for each event, one of which was the most extreme geomagnetic event in the list that we study (15 Mar, 2015). This way we can inspect the way the energy spectrum distorts following the geomagnetic disturbances.

i. Event of 12-16 Apr 2013 with $AL_{min} \approx$ -300 nT

Here is the evolution of solar wind parameters and geomagnetic indices (Figure 28). We can see that 12-13 Apr are considered quiet-time conditions, and the maximum disturbance occurs between 14-15 Apr.

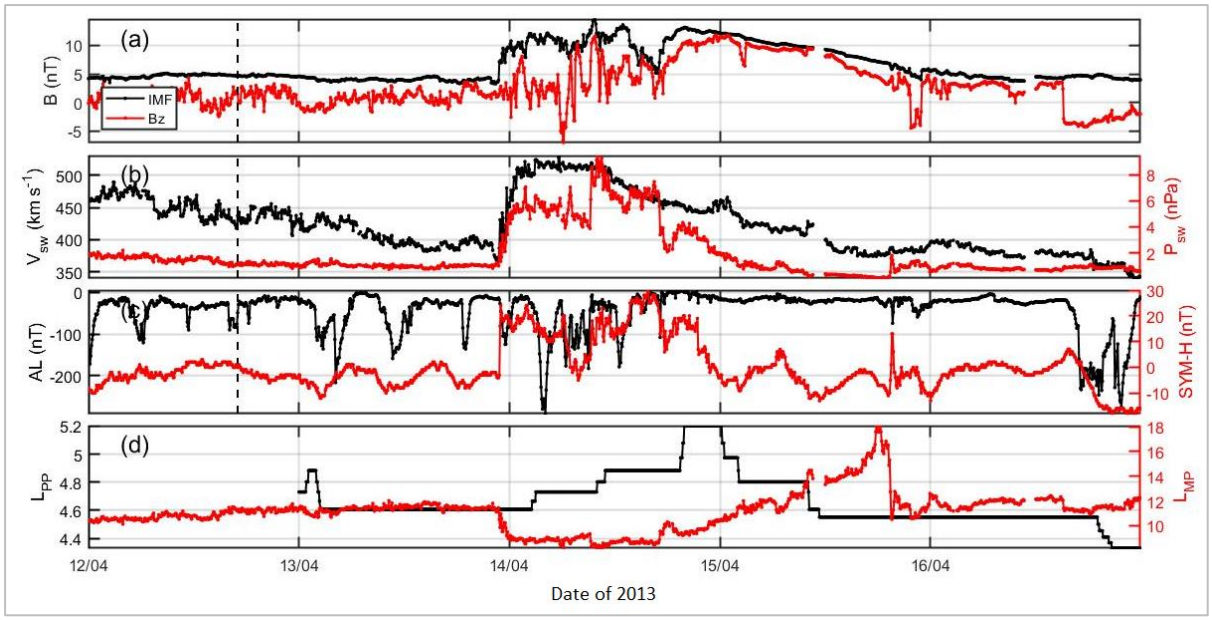

Figure 28 Evolution of solar wind properties, magnetospheric properties and indices for 12-16 Apr 2013. Figure produced in MATLAB by the author.

According to the physical background previously presented, and after manipulating the data according to the previous sections, we constructed a radial preview of the energy range for each μ value.

Here is an example of the energy ranges in the quiet-time conditions of this event (Figure 29):

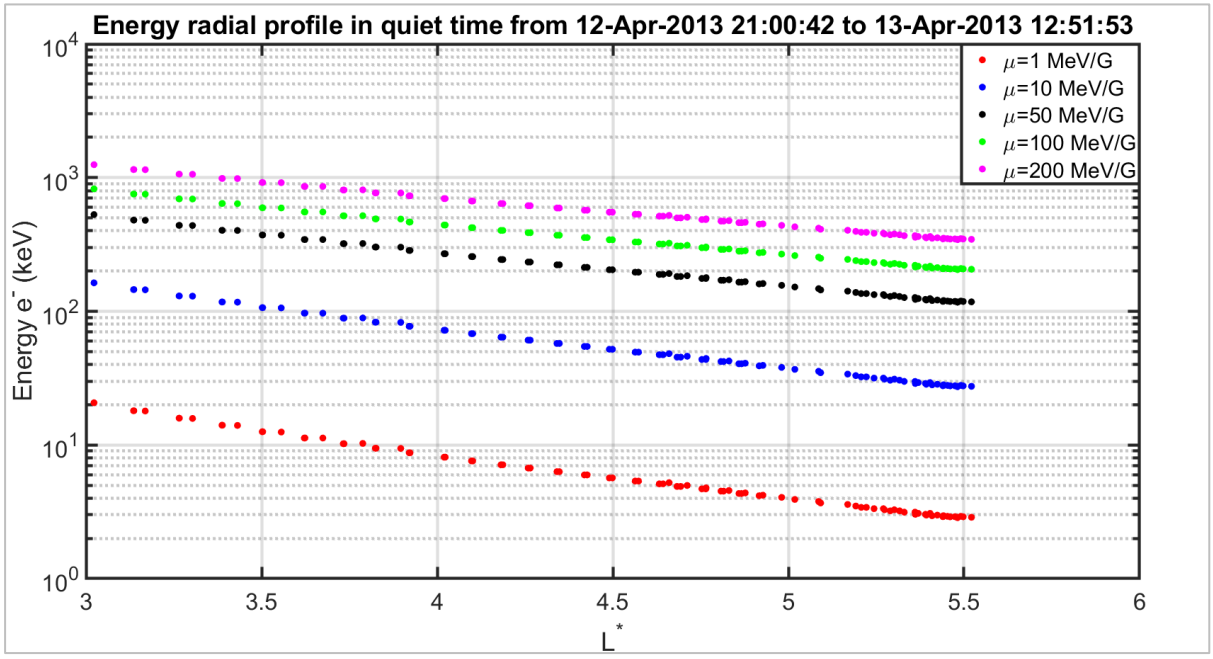

Figure 29 Radial profile of the energy in quiet-time conditions of the previous event, based on data from the RBSP mission. Figure produced in MATLAB by the author.

And here is a comparison of the quiet-time energy range (in color) together with the accumulative energy response (grey for each μ value) during all of the event (Figure 30):

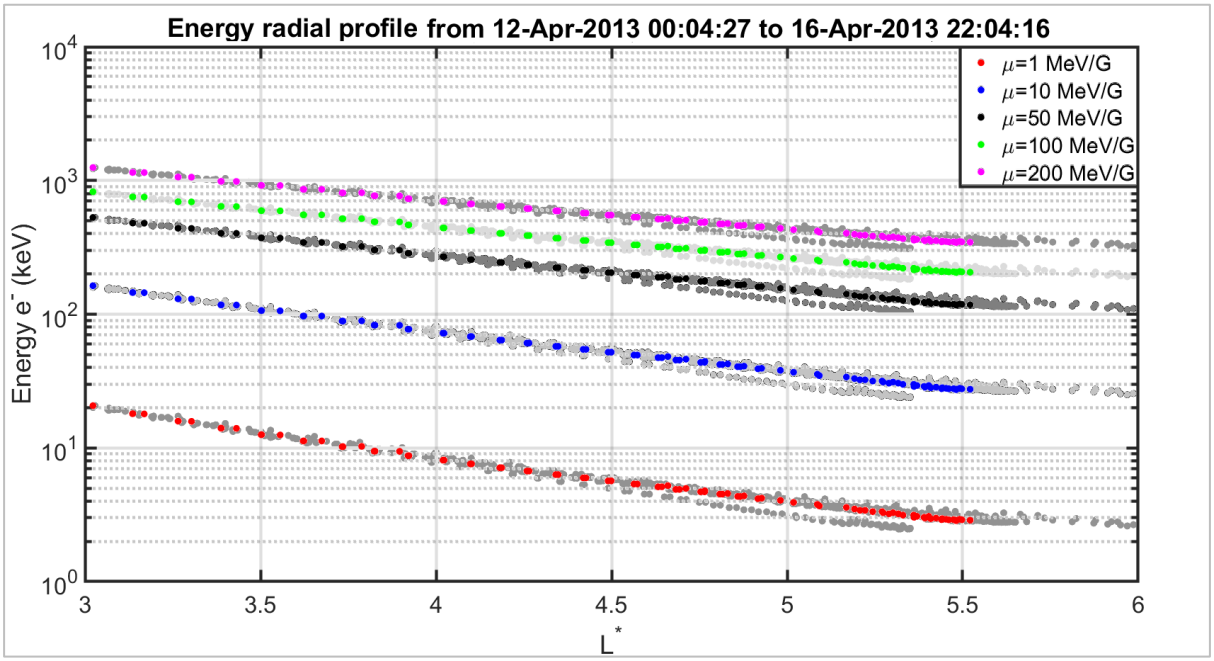

Figure 30 Radial profile of the energy for all the data accumulated during the previous event, based on data from the RBSP mission. Figure produced in MATLAB by the author.

We can see that in lower L* the energy range is almost identical, but there are some differences in higher L*, where some energy values are larger or smaller than of those in the quiet-time conditions. This indicates that the energy corresponding to each μ value is subjective to changes according to the magnetospheric disturbances, which are very small in this event.

ii. Event of 27 Feb – 5 Mar 2013 with $AL_{min} \approx$ -1000 nT

Here is the evolution of solar wind parameters and geomagnetic indices. We can see that 27-28 Feb are considered quiet-time conditions, and the maximum disturbance occurs between 1-3 Mar (Figure 31).

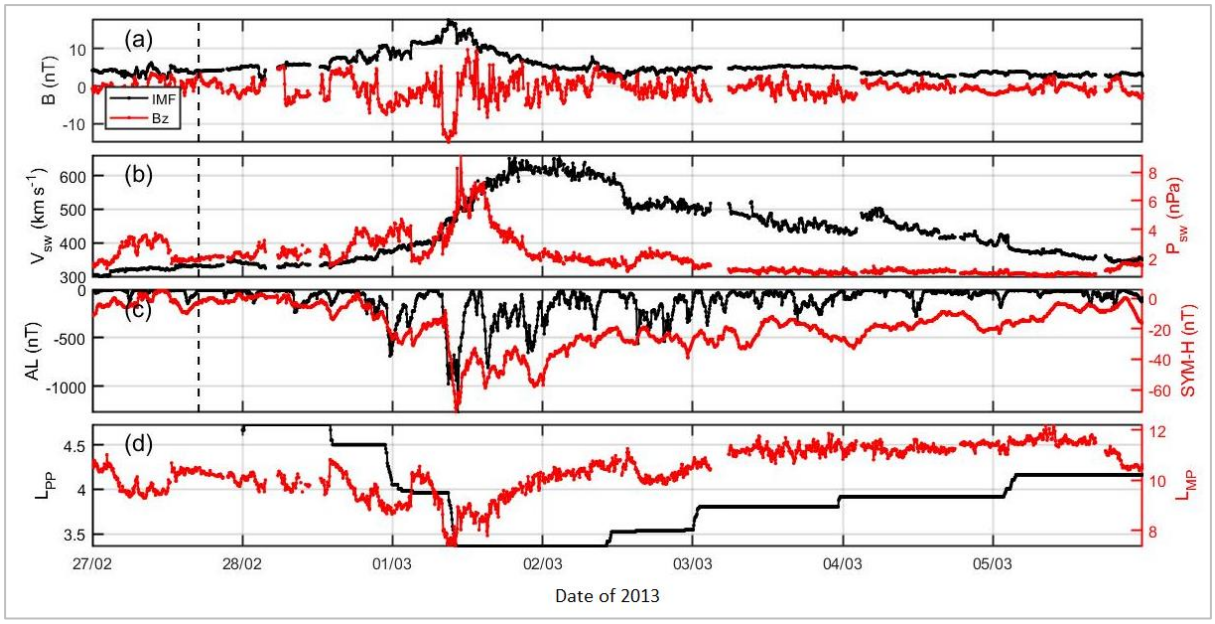

Figure 31 Evolution of solar wind properties, magnetospheric properties and indices for 27 Feb-5 Mar 2013. Figure produced in MATLAB by the author.

In this case we notice that the energy spectrum seems more disturbed, following the larger disturbance of the magnetosphere. Although, as in the previous event, the energy range at lower L* is comparable, but in larger L* it is very disturbed, but only reaching smaller energy values than those in the quiet-time conditions (Figure 32).

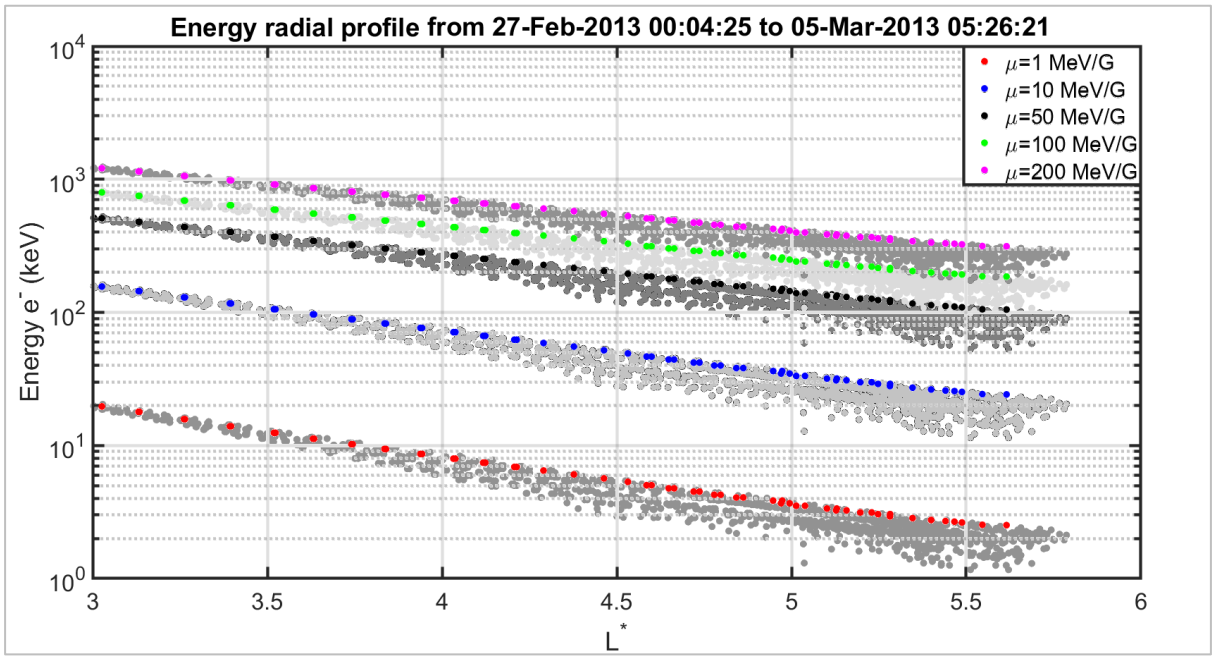

Figure 32 Radial profile of the energy for all the data accumulated during the previous event, based on data from the RBSP mission. Figure produced in MATLAB by the author.

iii. Event of 15-21 Mar 2015 with $AL_{min} \approx$ -2000 nT

This event is the most extreme, with AL reaching under -2000 nT. 15-16 Mar are considered quiet-time conditions, and the maximum disturbance occurs between 17-18 Mar (Figure 33).

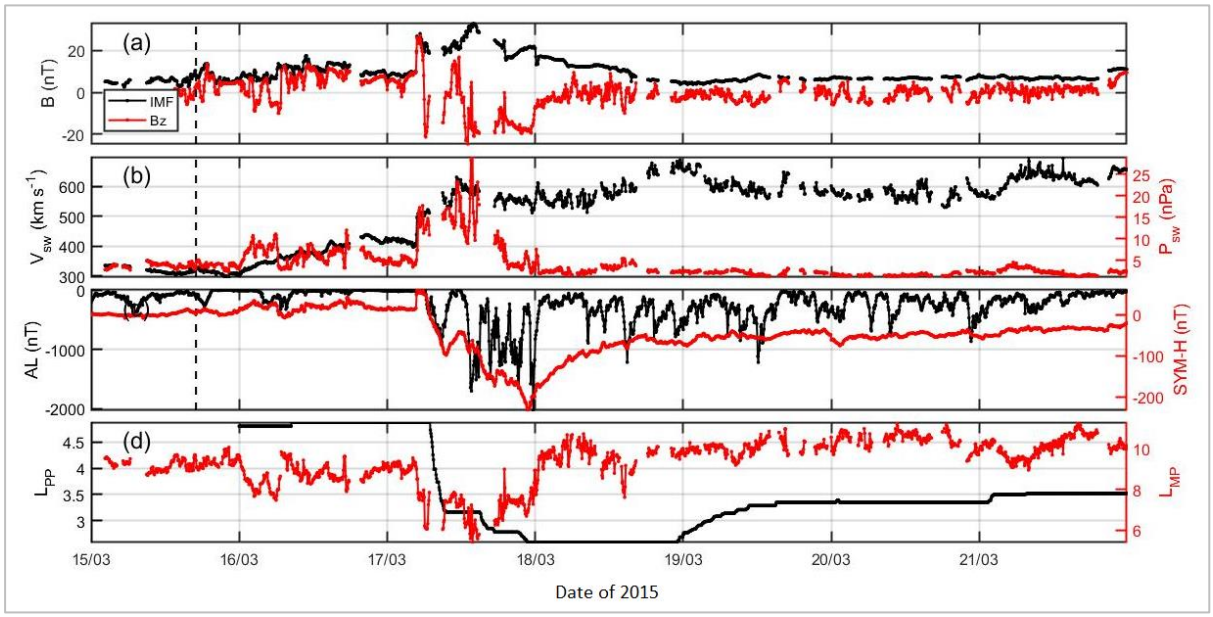

Figure 33 Evolution of solar wind properties, magnetospheric properties and indices for 15-21 Mar 2015. Figure produced in MATLAB by the author.

This time the energy spectrum is even more disturbed, following the great disturbance of the magnetosphere. The energy range is disturbed even in lower L*, but in larger L* it can take values smaller and larger than those in quiet-time conditions. The magnetospheric disturbance is so intense, that in some cases the last closed drift shell is located near L*=4 (Figure 34).

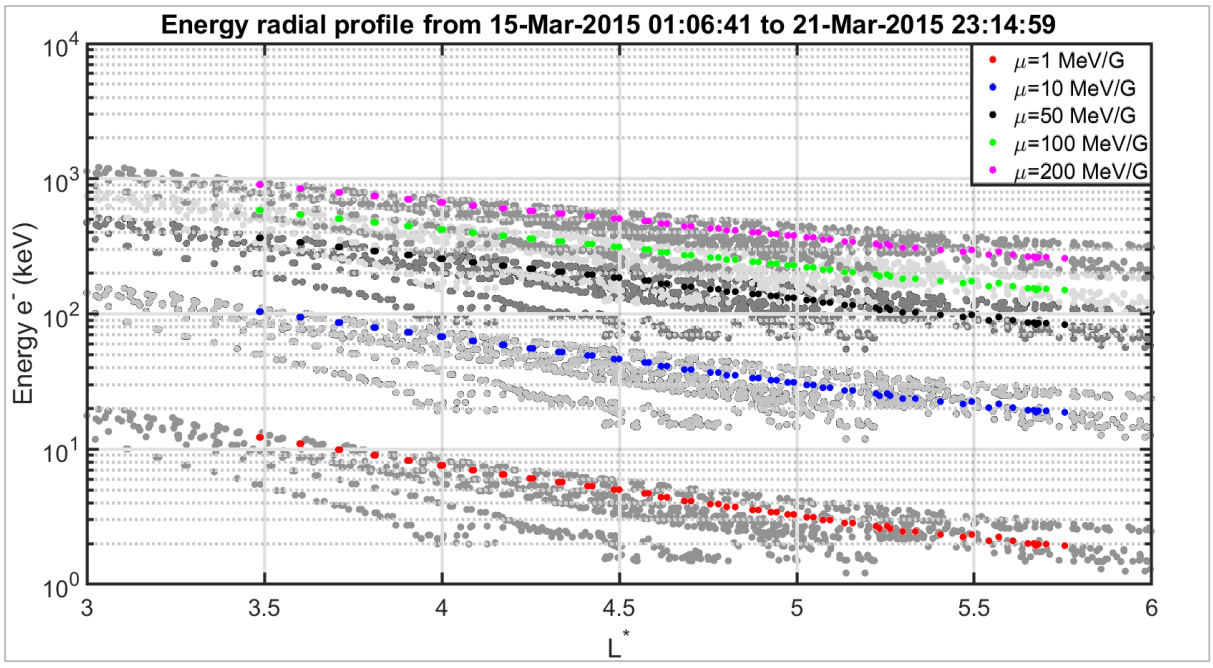

Figure 34 Radial profile of the energy for all the data accumulated during the previous event, based on data from the RBSP mission. Figure produced in MATLAB by the author.

iv. Defining the μ values

We can see that the energy spectrum is different depending to the magnetospheric conditions, and is summarised according to the electron populations during the event of 27 Feb – 5 Mar 2013, as a medium response event, at each region, as follows:

	L*=3-4		L*=4-5		L*=5-6	
μ [MeV/G]	$\epsilon\ [keV]$	e	$\epsilon\ [keV]$	e	$\epsilon\ [keV]$	e
1	6 – 10	Source	2 – 8	Source	1 – 4	Source
10	60 – 100	Source/Seed	20 – 70	Source	10 – 40	Source
50	200 – 400	Seed	100 – 300	Seed	50 – 150	Source/Seed
100	300 – 600	Seed/Rel	150 – 500	Seed	100 – 250	Source/Seed
200	600 – 1000	Rel	300 – 700	Seed/Rel	200 – 400	Seed

Table 8 The values of the first adiabatic invariant μ and the corresponding electron energy values and electron populations that are inferred from the previous sections. They are summarized in Table 9. Table produced by the author.

According to these energy ranges, we use each μ value to describe one electron population, for simplicity, as:

μ [MeV/G]	$\epsilon\ [keV]$	e
1	1 – 10	Source
10	10 – 100	
50	50 – 400	Source/Seed
100	100 – 600	Seed
200	200 – 1000	Seed/Relativistic

Table 9 The values of the first adiabatic invariant μ and the corresponding electron energy values and electron populations. Table produced by the author, based on Table 8.

3.4 ULF wave amplitude and power

The last thing we need to calculate is the Pc5 wave power. To do this, we must load the magnetic ephemeris, read the magnetic field B, filter it, and perform a Morlet Wavelet Transform, extracting the wave amplitude and calculating the power for the Pc5 waves, for enhancement and depletion events. The method we follow for the Morlet Wavelet Transform is presented by Balasis et al. [2013], Katsavrias et al. [2019] and Nasi [2017].

The main advantage of Wavelet transform over Fourier transform is that it provides information not only about the frequency of the timeseries characteristics but also about their timing. This is possible by using special base functions called wavelets, instead of the sine and cosine functions. Wavelets have a localised behaviour in time and this way they can reveal the local properties of timeseries. They are not periodic functions, so they are not characterised by a period, but from their scale size or scale, which tells us how compact they are in time.

To perform the wavelet transform we will create a script (*myWavelet*) based on the *wavelet* function and other complementary functions which can be found on the Torrence & Compo site: http://paos.colorado.edu/research/wavelets. One of the outputs of the *myWavelet* script is the wavelet transform $W_n(s)$, called *wavex* in the script, from which we determine the ULF wave amplitude and calculate the power.

Now the Pc5 wave power is saved in the epoch folder and is ready for performing a superposed epoch analysis and plotting.

Chapter 4: Superposed Epoch Analysis

In the epoch folder, we finally determine the key time t_0 and create the final plots. First, we must understand the way we perform the superposed epoch analysis and the way we select the key time t_0, and then we will present the way we fold the desired quantities around it.

4.1 Epoch analysis

A useful tool in data analysis is the Superposed Epoch Analysis (SPE or SEA). It can be used to:

- Detect periodicities within a time sequence:
  The data sequence can be broken into separate subsets of equal duration, and then all subsets can be superposed. This requires some hypothesis for the length of the period to set the subsets' duration.

- Reveal a correlation between two data sequences:
  A key time must be defined, corresponding to each occurrence of an event in one data sequence (#1). Then, subsets of data from another sequence (#2) are extracted, within some time range near each key time. All extracted subsets from sequence #2 are superposed, with key times synchronized, by adding them. Data binning is often used to effectively superpose data from sequence #2 that are recorded at different or irregular times.

In this study, we want to compare the behaviour of two event groups, resulting in enhancement or depletion of the average relativistic electron PSD. To do this, we select a key time t_0 corresponding to a specific event occurring once in every event, and we will plot all the quantities we examine around it.

4.2 Selecting the key time t_0

The way we select the key time t_0 depends on each study. Here, we want to examine the relationship between source electrons, seed electrons, primarily chorus waves and secondarily ULF waves, during and after substorms. So, we must choose a key time corresponding to a vital event during substorms. We decided that this event is the start time of continuous substorm activity, which is indicated by the decrease of the AL index, as we expect that after this point, the source electrons begin to be injected to the inner magnetosphere.

We create a script to manually select the key time for each event. This script reads the OMNI data and creates a plot of AL index, the user automatically uses the cursor and clicks on the point where AL begins its drop. This action extracts the cursor data and saves the timestamp. This way we create a new variable, *keyT*, containing 28 key times t_0, one for each event, corresponding to the moment when AL begins to drop, indicating enhanced substorm activity in the following time period.

Here is an example of a selected event (December 6-12, 2013) for which we selected the time t_0 based on the AL index starting to indicate enhanced activity (Figure 35):

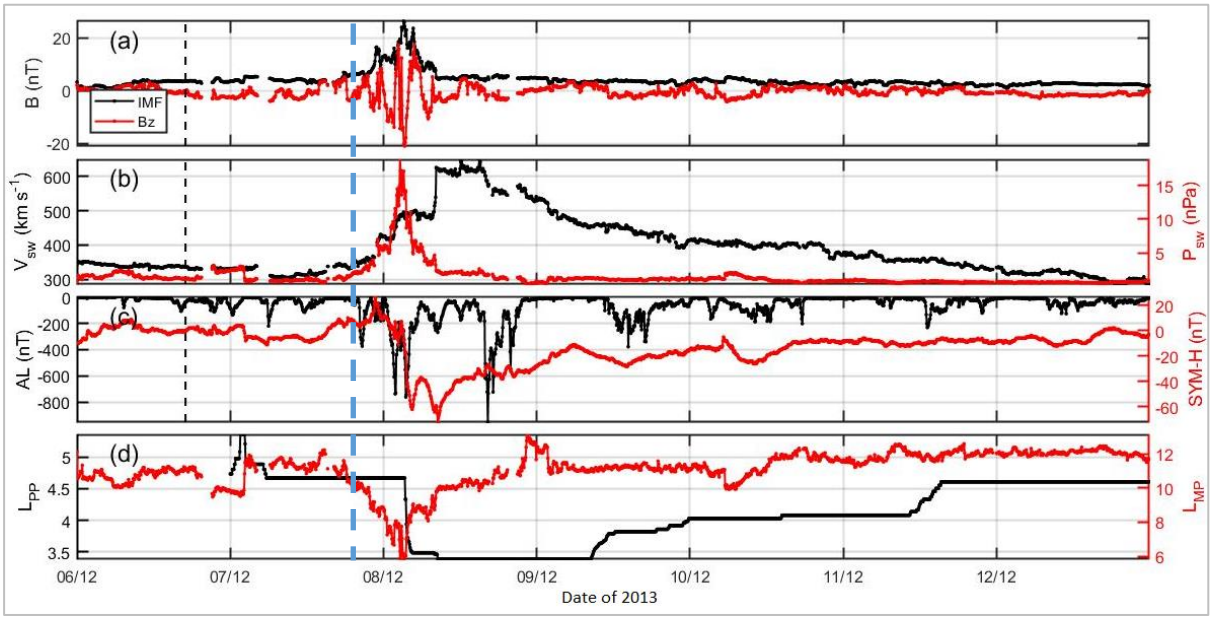

Figure 35 The selection of key time t_0 (7/12 18:20), denoted by a dashed blue line, based on the evolution of AL index, for the example event of December 6-12, 2013. Figure produced in MATLAB by the author.

4.3 Creating the plots

All the files and variables we need for plotting are now ready. In the epoch folder, we create all the necessary scripts (*Epoch_Folding_…*) to load, read, fold and plot the desired quantities. The final output is comprised by 58 plots, for all the desired quantities (solar wind, geomagnetic indices, PSD, waves), for enhancement and depletion events. The plots are presented in the next chapter, and have the following properties (Figure 36):

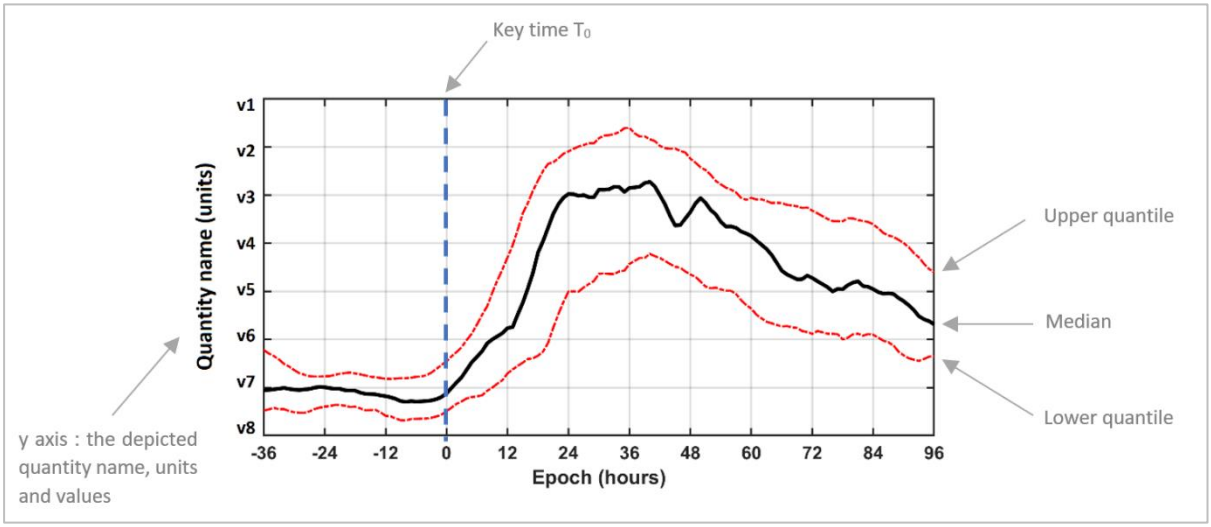

Figure 36 Example of a produced plot, as a result of this study, along with an explanation of its basic properties, all listed below. Figure produced in MATLAB by the author

i. Key time t_0

The vertical dashed line across all plots corresponds to the selected key time t_0, so to Epoch = 0 h, and is defined as the time when AL index begins decreasing, indicating enhanced substorm activity. All the desired quantities are plotted around it.

ii. Plot axes

The x axis of every plot is the Epoch in hours. It extends from -36 h before the selected T_0, to +96 h or +120 h after, divided every 12 h. This way we can inspect the conditions just before the event, and their development in time for several days.

The y axis of every plot represents the plotted quantity, with the corresponding units and divisions.

iii. Median value of the quantities

The plotted quantities are depicted with a solid black line corresponding to the median values of the quantity, either for the group of 20 enhancement events, or for the group of 8 depletion events.

The properties of a dataset can be measured by its median, which is a useful tool in statistics and probability theory and can be thought of as the "middle" value. Its advantage compared to the mean, which is often described as simply the "average", is that it can give a better idea of a "typical" value, because a small proportion of extremely large or small values of the dataset cannot skew the median so much as the mean, so the median is usually the preferred measure of central tendency when the distribution is not symmetrical.

For a finite list of numbers, the median can be found by arranging the numbers from smallest to greatest. For an odd number of numbers, the middle one is picked. For an even number of numbers, the median is the mean of the two middle numbers. The index of the middle number of a dataset a of n numbers in numerical order can be found as $(n+1)/2$, which either gives the middle number (for an odd number of numbers) or the halfway point between the two middle numbers (for an even number of numbers), so the median can be taken by averaging the floor $(\lfloor \dots \rfloor)$ and the ceiling $(\lceil \dots \rceil)$ numbers of the point.

So, the median of a dataset a of n numbers can be represented as:

$$median(a) = \frac{a_{\lfloor (n+1)/2 \rfloor} + a_{\lceil (n+1)/2 \rceil}}{2}$$

In MATLAB, the median can be calculated using the command y = median(x). We will use the command y = nanmedian(X), which is the median computed after removing NaN values.

iv. Quantiles

The dashed red lines in every plot are the upper and lower quantiles of the depicted quantity, the area between which includes 50% of the events in each event category.

If we divide the range of a probability distribution into continuous intervals with equal probabilities, or we divide the observations in a sample in the same way, then the cut points are the quantiles. There is one less quantile than the number of groups created. In statistics and probability, quantiles are useful because they are less susceptible than means to long-tailed distributions and outliers. If the data are not distributed according to an assumed distribution, or if there are outliers far from the

mean, then quantiles are more useful descriptive statistics than means and other moment-related statistics.

For a finite set of values, if we divide it into q subsets of (nearly) equal size, we do it by creating a set of q-1 q-quantiles, one for each integer k where 0 < k < q.

For 2 divisions, the one 2-quantile is actually the median.

For 4 divisions, the three 4-quantiles are called quartiles. Thus, quartiles are the three cut points that will divide a dataset into four equal-sized groups, each containing ¼ of the dataset. They are denoted by Q, as Q1, Q2 and Q3, where again the Q2 quartile is the median. The Q1 and Q3 quartiles are called the lower and upper quantile/quartile, respectively. Also, the difference between the upper and lower quartiles is also called the interquartile range, midspread or middle fifty, is denoted as IQR = Q3 − Q1, and contains the 50% of the dataset.

For a population, of discrete values or for a continuous population density, the k-th q-quantile is the data value where the cumulative distribution function crosses k/q. That is, x is a k-th q-quantile for a variable X if $Pr[X < x] \leq k/q$ and $Pr[X > x] \leq 1 - k/q$.

If, instead of using integers k and q, the "p-quantile" is based on a real number p with 0 < p < 1 then p replaces k/q in the above formulas as $Pr[X < x] \leq p$ and $Pr[X > x] \leq 1 - p$.

In MATLAB, the quantiles of a data set can be calculated using the command y = quantile(x,p) which returns quantiles of the elements in x for the cumulative probability or probabilities p in the interval [0,1]. In our case, we want the upper and lower quartiles, Q1 and Q3, meaning $k = 1$ and $k = 3$ for $q = 4$, so we will use the values $p = k/q = 1/4 = 0.25$ and $p = k/q = 3/4 = 0.75$ respectively.

v. Presentation

The plots for enhancement events are located on the left, and for depletion on the right. All plots are aligned based on the key time t_0. Below the lower quantile lies the 25% of the events, below the median lies the 50% and below the upper quantile lies the 75% of the events, in each event category, meaning enhancement or depletion events.

The plots are presented in Chapter 5, divided in certain groups for easier comparison:

Chapter 5: Results and discussion

5.1 Parameters and indices

5.1.1 Solar wind parameters: IMF, Bz, V_{SW}, P_{SW}

The depicted quantities are the **Interplanetary Magnetic Field IMF [nT]**, its **horizontal component Bz [nT]**, the **solar wind velocity V_{SW} [km/s]**, and the **solar wind dynamic pressure P_{SW} [nPa]**.

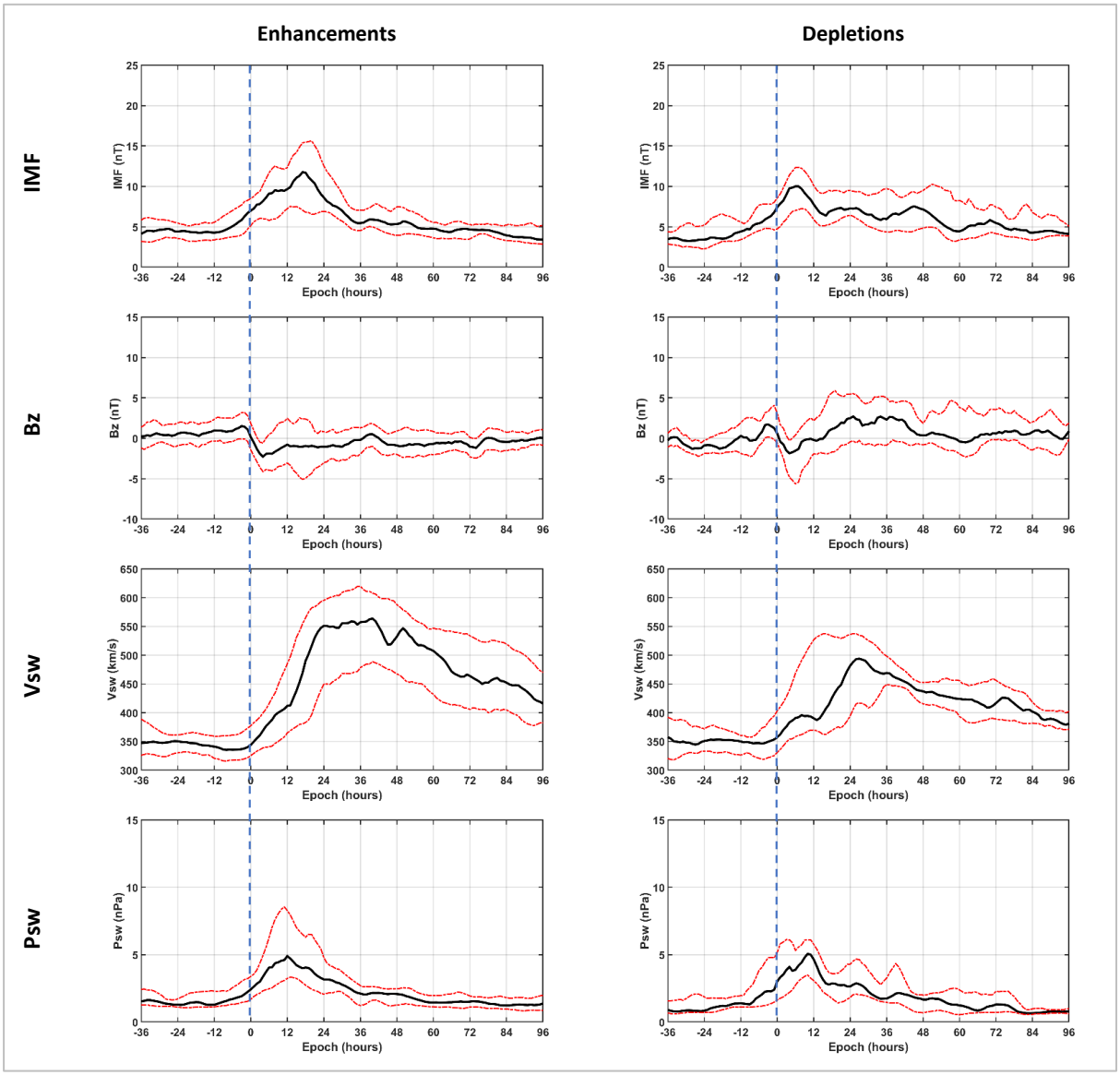

Figure 37 Superposed epoch analysis on solar wind parameter values for enhancement (left) and depletion events (right). Top to bottom: the Interplanetary Magnetic Field IMF [nT], its horizontal component Bz [nT], the solar wind velocity V_{SW} [km/s], and the solar wind dynamic pressure P_{SW} [nPa]. Figure produced in MATLAB by the author.

All the parameters begin diverging some hours before t_0.

The **Interplanetary Magnetic Field IMF [nT]** at first shows a similar increase in both event categories, but in enhancement events it is followed by a second increasing step at 12h, reaching a maximum in 18h, although in depletion events it just decreases to a plateau. Both return to the pre-event phase values after 60h.

The **horizontal component of the IMF, Bz [nT]** also shows a similar small increase and then decrease to comparable values for both event categories until 12h after t_0, but in enhancement events it stays negative/southward for almost 36h, although in depletion events it turns to positive/northward at 12h and at least until 48h.

The **solar wind velocity V_{SW} [km/s]** exhibits the largest difference between the two event categories. In enhancement events it shows a two-step increase with a maximum value over 550 km/s at 24h that forms a plateau until 40h and then stays larger than the pre-event phase value even after 96h, and even larger that the median velocity $\bar{V}$ for years 2013-2018, $(\bar{V} = 420\ km/s)$ for over 84h. Although, in depletion events, the increase is still two-step but with a smaller maximum value near 500 km/s at 24h that then just decreases, crossing $\bar{V}$ only after 48h .

The **solar wind dynamic pressure P_{SW} [nPa]** shows a small difference between the two event categories. In enhancement events it gradually increases some hours before t_0, reaches a maximum value at 12h and then gradually decreases until after 48h. In depletion events, it increases more sharply 10h before t_0, even for the upper quantile, forms two small steps reaching a smaller maximum value before 12h, and then sharply decreases after 12h. Another difference is that the pre- and post-event phase values are still larger in enhancement events.

It is important to note that these results agree with those of Katsavrias et al. [2019], which follow the same list of events but were depicted based on a different key time t_0', defined as the time of the maximum compression of the magnetopause (almost $t_0' \cong t_0$+12h as shown in the next section, for L_{MP}) . This agreement shows that the method of selecting the key time does not affect the solar wind parameter behaviour in any way, and does not skew the properties of the two event categories.

Also important is the fact that Bz and V_{SW} can act as reconnection rate proxies, as their product (magnetic field cross velocity) gives us an electric field: $-Bz \cdot V_{SW} = E_y$, that can be thought of as a proxy for the rate of reconnection happening on the dayside magnetopause, according to Newell [2007] and Burton [1975], where the product equals zero for positive Bz. We note that for 0-12h Bz is negative in both event categories and V_{SW} shows a similar increase, so reconnection is enhanced. Later, for 12-24h, Bz is still negative for enhancement but positive for depletion events, while V_{SW} shows a second step of increasing values, much larger for enhancement events, so the rate is even larger for enhancement events, but almost none in depletion events, because of the positive Bz. This will prove useful in later sections.

These results also agree with those of Baker and Daglis [2007] which note that an interval of southward IMF along with a period of $V_{SW} \geq 500$ km/s plays a key role in relativistic electron enhancements, and also they agree with the results of Li et al. [2015] which note that a combination of prolonged southward Bz, high solar wind speed and low solar wind dynamic pressure are critical to lead to efficient MeV electron acceleration, and these parameters are more efficient if operating simultaneously.

In summary, we can conclude that:

- Enhancement events are caused by disturbances showing a two-step increased IMF, a prolonged negative Bz, and a highly increased and long lasting V_{SW} values reaching over 500 [km/s], together resulting in enhanced magnetic reconnection at the dayside magnetopause.

5.1.2 Geomagnetic indices: SYM-H, AL
Magnetopause location: L_{MP}, Plasmapause location: L_{PP}

The depicted quantities are the **SYM-H index [nT]**, the **AL index [nT]**, the **magnetopause location L_{MP} [R_E]**, and the **plasmapause location L_{PP} [R_E]**.

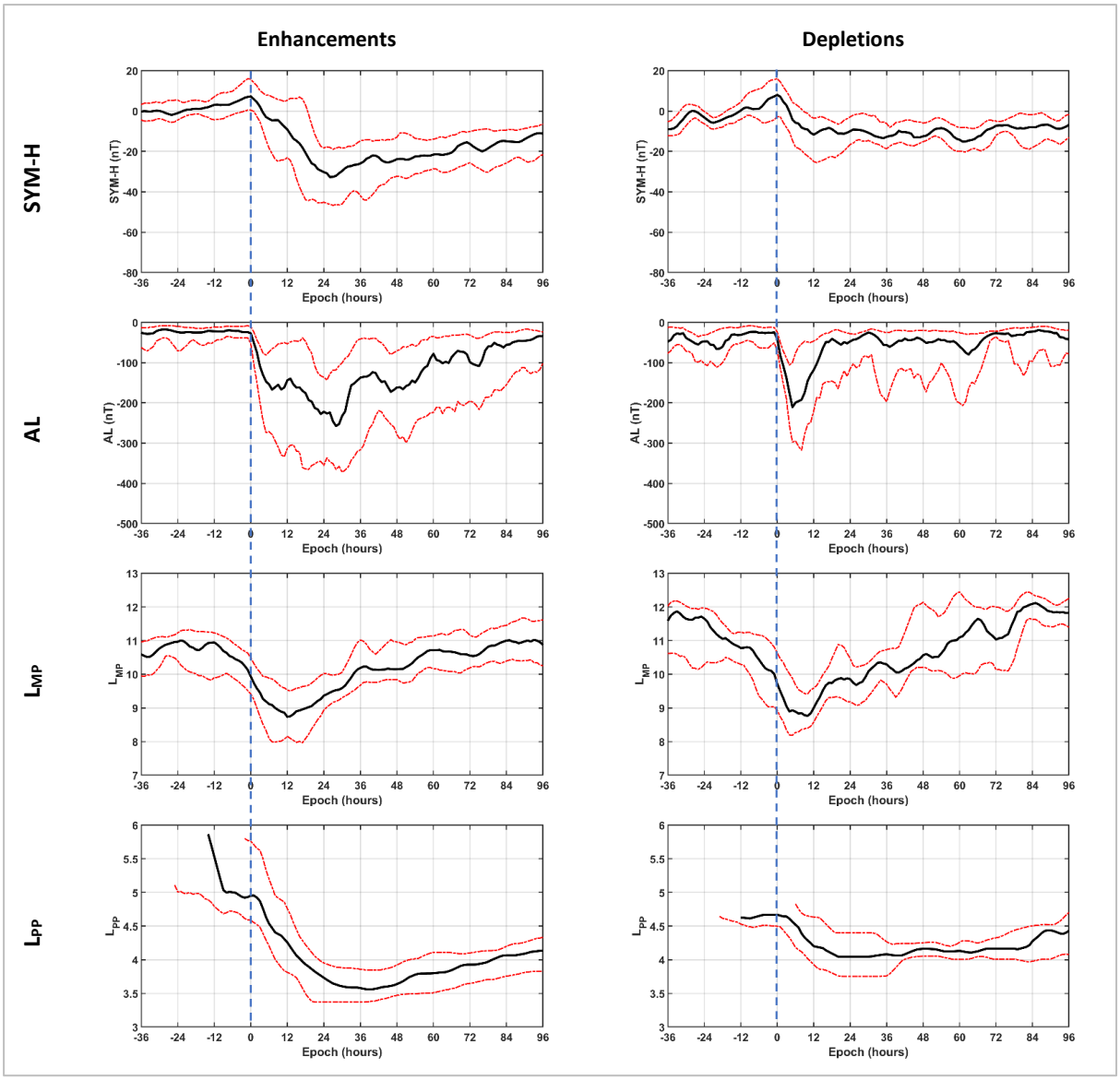

Figure 38 Superposed epoch analysis on geomagnetic indices values and the location of the magnetopause and plasmapause. Top to bottom: the SYM-H index [nT], the AL index [nT], the magnetopause location L_{MP} [R_E], and the plasmapause location L_{PP} [R_E]. Figure produced in MATLAB by the author.

All the parameters begin diverging some hours before t_0, except AL from whose behaviour we defined t_0 as the start time of continuous substorm activity, as indicated by the decrease of AL index, as obvious in both event categories.

The **SYM-H index [nT]** shows a large difference between the two event categories. In both it creates a small peak around t_0, which in enhancement events is followed by a big decrease to a minimum value around -40 nT at 24h, and then gradually increases to its pre-event phase values even after 84h. Although, in depletion events, the peak is followed by a small and decrease around -20 nT thus returning to its pre-event phase values in after 12h.

This shows that geomagnetic storms which occur during enhancement events are statistically stronger and longer than those occurring during depletion events. We can conclude that this is associated with Bz and V_{SW}, which again shows a direct linking to Ey, as a rate of reconnection proxy, which is an important factor of geomagnetic storms, as again showed by Burton [1975]. As expected, from 0-12h when the rate of reconnection is enhanced, SYM-H decreases for both enhancement and depletion events, but from 12-24h when the reconnection is only enhanced for enhancement events, SYM-H continues decreasing to its minimum, although for depletion events SYM-H returns to its normal values. In comparison (Figure 39):

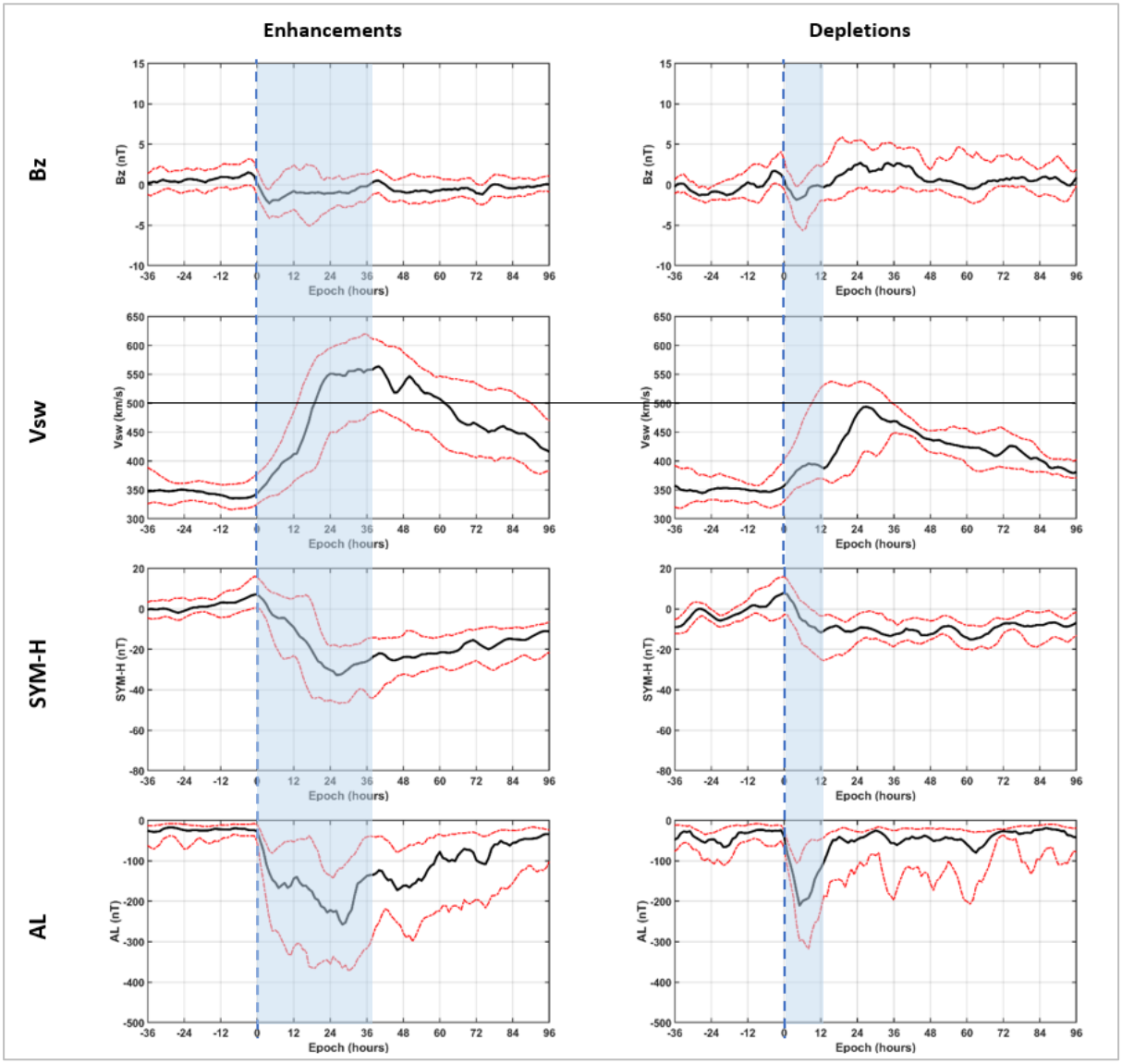

Figure 39 Comparison of some parameters and indices from previous figures. The product of -Bz and V_{SW}, giving Ey, acts as a rate of reconnection proxy and thus correlates with SYM-H and AL indices. When Bz is negative during enhanced V_{SW}, Ey is positive indicating enhanced reconnection, which is denoted with a blue rectangle. When Bz turns positive, Ey and thus reconnection eliminates. In enhancement events the V_{SW} reaches values over 500 km/s denoted by a black horizontal line.

The **AL index [nT]** also shows a large difference between the two categories. At first, in both event categories the AL is almost stable. After t_0 it shows a similar decrease in both categories, which in enhancement events is followed by a second step reaching -250 nT around 30h and then remains enhanced until almost 72h, but in depletion events it reaches a minimum of around -200 nT in 6h and then just increases to its pre-event phase values in only 18h. The lower quantile exhibits the same behaviour, meaning that 75% of enhancement events do (because the y axis has negative values).

This shows prolonged substorm activity throughout enhancement events but very limited in depletion events. This is expected, as shown by Hajra et al. [2014c], that lengthy and continuous intervals of AE, thus AL, activity are ideal for electron acceleration. Once again, results show the dependence of substorm activity on Bz and V_{SW}, thus on Ey, as a rate of reconnection proxy, following the results of Pulkkinen [2015]. Comparison is shown in the previous figure (Figure 39).

The **magnetopause location L_{MP} [R_E]** shows a similar compression to 9 R_E around or before 12h in both event categories. This is expected since the location of the magnetopause, as calculated from the Shue 1998 model, is strongly dependent on the P_{SW} which reaches similar maximum values but earlier in depletion events. Also, the magnetopause seems more compressed pre- and post-event in enhancement events. This may be because of the slightly larger P_{SW} pre- and post- event in enhancement events in comparison to depletion events, but it can also be random and depending on our event sample. In comparison (Figure 40):

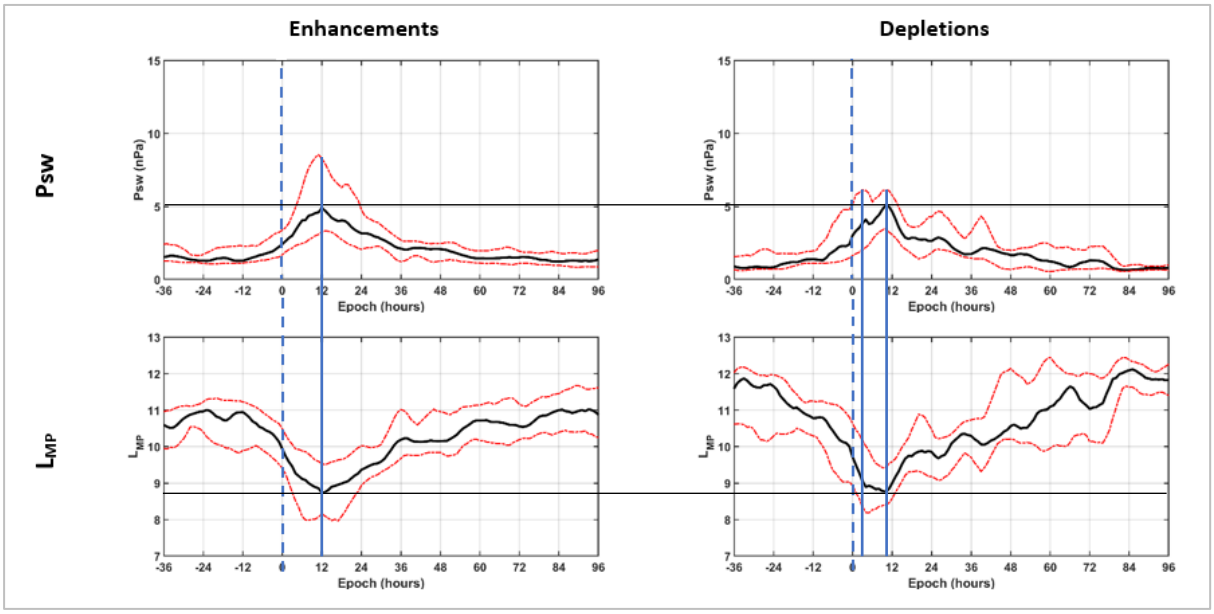

Figure 40 Comparison of some parameters from previous figures. The dayside magnetopause location is calculated from a model highly dependent on the P_{SW}, so they are clearly correlated, reaching extreme values at the same time, denoted by blue vertical lines. The extreme values of the median are comparable in the two event categories, denoted by black horizontal lines.

The **plasmapause location L_{PP} [R_E]** begins around 5 R_E and reaches a minimum of 3.5 R_E in 36h in enhancement events, although in depletion events it begins around 4.7 R_E and compresses only to 4 R_E. The plot seems correlating with the SYM-H index, which is logical as both are affected by the ring current. The plasmapause reaches its minimum value almost 12h after the SYM-H minimum. In comparison (Figure 41):

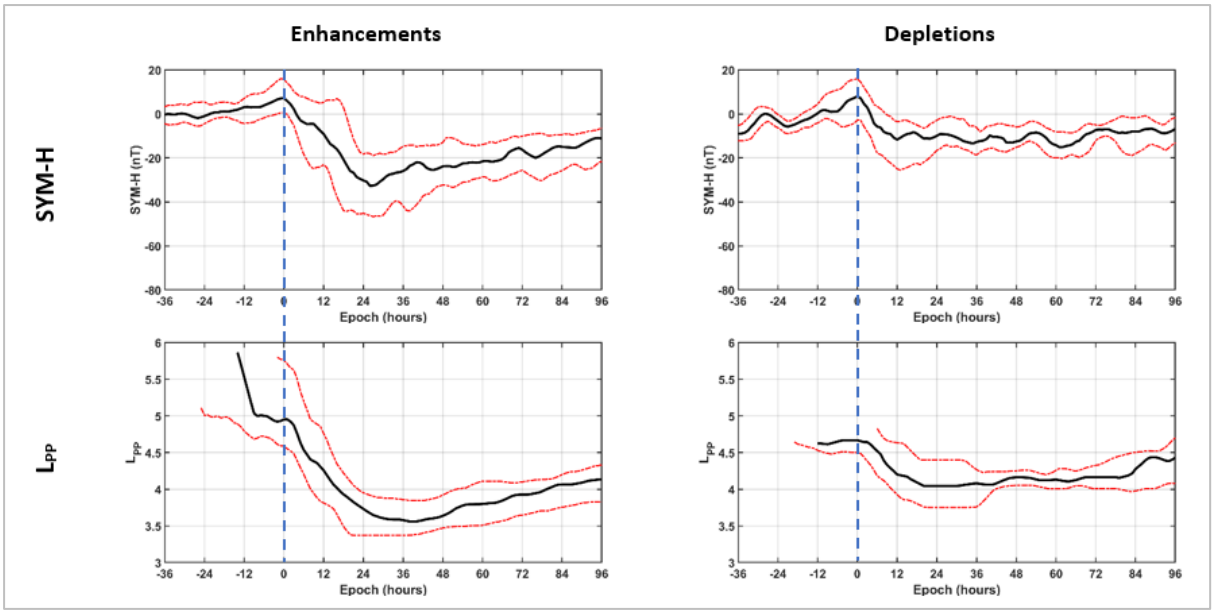

Figure 41 Comparison of some parameters from previous figures. The plasmapause location correlates with the SYM-H index, as the plasmasphere is affected by the geomagnetic storm activity.

These results agree with those of Pierrard [2008], who notes that during storm events the plasmapause moves closer to the Earth. We also note the fact that in enhancement events, the plasmapause position reaches values under L=4.

In summary, we can conclude that:

- Enhancement events are characterised by increased geomagnetic activity, indicated by prolonged negative SYM-H and AL indices, meaning statistically stronger and more prolonged storm and substorm activity, and a significantly compressed plasmapause reaching under L=4.

5.2 Waves vs L or L*

5.2.1 Chorus wave amplitude vs L

All plots depict the **chorus wave amplitude [pT] versus L**. All values have been normalized to the median between 18-36 h before t_0, separately for the group of enhancement and of depletion events.

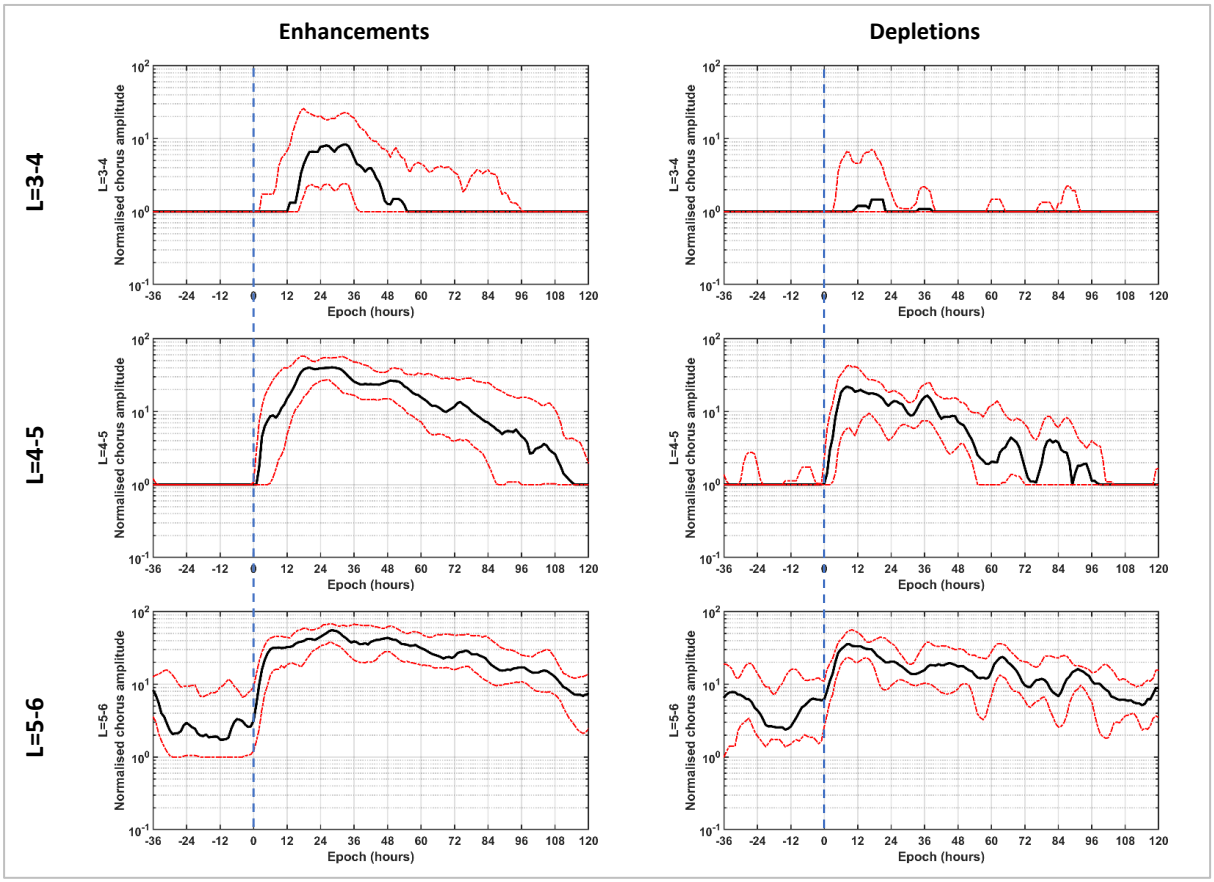

Figure 42 Superposed epoch analysis on chorus wave amplitude values [pT] at different magnetospheric regions noted by L. Top to bottom: L=3-4, L=4-5, L=5-6. Figure produced in MATLAB by the author.

At **L=3-4** the chorus waves exhibit the largest difference between the two event categories. They appear some hours after t_0 (3h for the upper quantile, 10h for the median) with a maximum of almost 10 pT from 20-36h for enhancement events, that ends before 48h, but they are almost negligible for depletion events.

The time lag and small amplitude that is presented in L=3-4 can be justified by the plasmapause location, which we saw that crossed or was around L=4 during 12-72h for enhancement events and during 12-36h for depletion events. As mentioned by Meredith et al. [2001], chorus waves appear outside the plasmasphere, so in depletion events chorus waves are almost not detected at L=3-4, as the plasmapause almost never reaches values L<4, except around 24h where we see a tiny amplitude of 0-6 pT. On the other hand, in enhancement events the plasmapause can reach values 3.3<L<4 during 12-72h where we can detect chorus waves of 1-20 pT. In comparison (Figure 43):

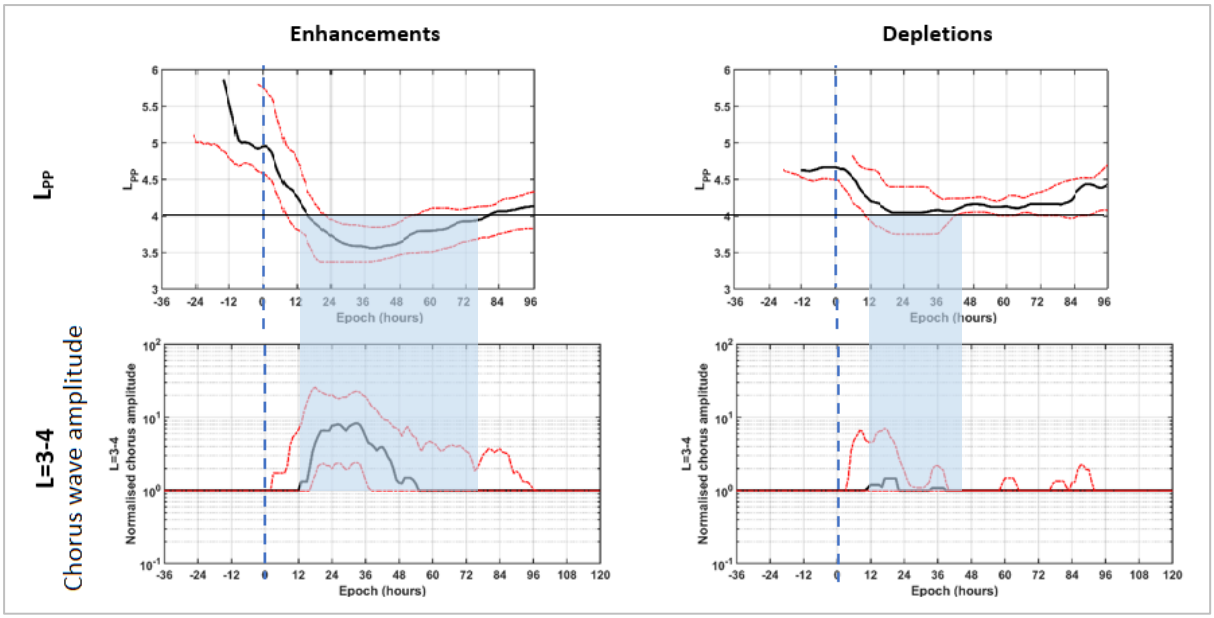

Figure 43 Comparison of some parameters from previous figures. The appearance of chorus waves at L=3-4 correlates with the plasmapause location. As long as the plasmapause is located outside L=4, which is denoted by a black horizontal line, the waves are obscured. When the plasmapause compresses and comes near or crosses L=4, the waves can be detected, as denoted by a blue rectangle.

Moreover, according to Li et al. [2013], the chorus wave amplitudes inferred by their method, can only be used effectively for values over ~10 pT, since the electron fluxes measured by the 0° telescope of the POES satellites could be close to the background level if the chorus-driven pitch angle scattering is too weak. At L=3-4, where the chorus wave amplitude lies mostly under 10 pT, it is not safe to reach any conclusions, so we consider them as negligible in both event categories.

At **L=4-5** the chorus waves appear almost immediately after t_0, and exhibit a two-step increase to 40 pT and a gradual slow decrease until 108h in enhancement events. In depletion events, they exhibit a single peak of 20 pT at 6h and a quicker and fluctuating decrease until 96h. The maximum value is larger, it is reached later, and the duration is larger in enhancement events.

At **L=5-6** the chorus waves appear almost before t_0, and exhibit a sharp increase to 30 pT in 6h, and later reach 50 pT after 24h, while continuing to fluctuate and slowly decrease, until after 120h in enhancement events. In depletion evens their behaviour is comparable, but with only one maximum of 40 pT at 6h and a greater decrease rate.

Our results agree with those of Bingham [2018], who presented chorus wave power increasing at larger L*, and appearing mostly inside the main phase of storms, and also until 24h or more into the recovery phase. They also agree with Li et al. [2016] who showed that in enhancement events, the chorus wave activity is more pronounced and long-lived in a broad L-shell region.

Although, considering the previous notes about region L=3-4, we can see that chorus waves appear almost at t_0, so they should correlate with AL index (Figure 44), thus substorm activity, agreeing with the results of Meredith et al. [2001], Li et. Al [2015], Boynton et al. [2018]. This is expected, as chorus waves are generated due to anisotropic angular distributions of source electrons that get injected to the inner magnetosphere during substorms, according to O'Brien et al. [2003], Baker and Daglis [2007], Thorne et al. [2013].

On the other hand, we can see that this is not entirely true, as the chorus wave amplitude is comparable for the two event categories, even though we already saw that storm and substorm activity is not that enhanced in depletion events. This means that the chorus waves in reality correlate with something else, which we expect is the source electron appearance, that is examined via their PSD in later sections. In comparison (Figure 44):

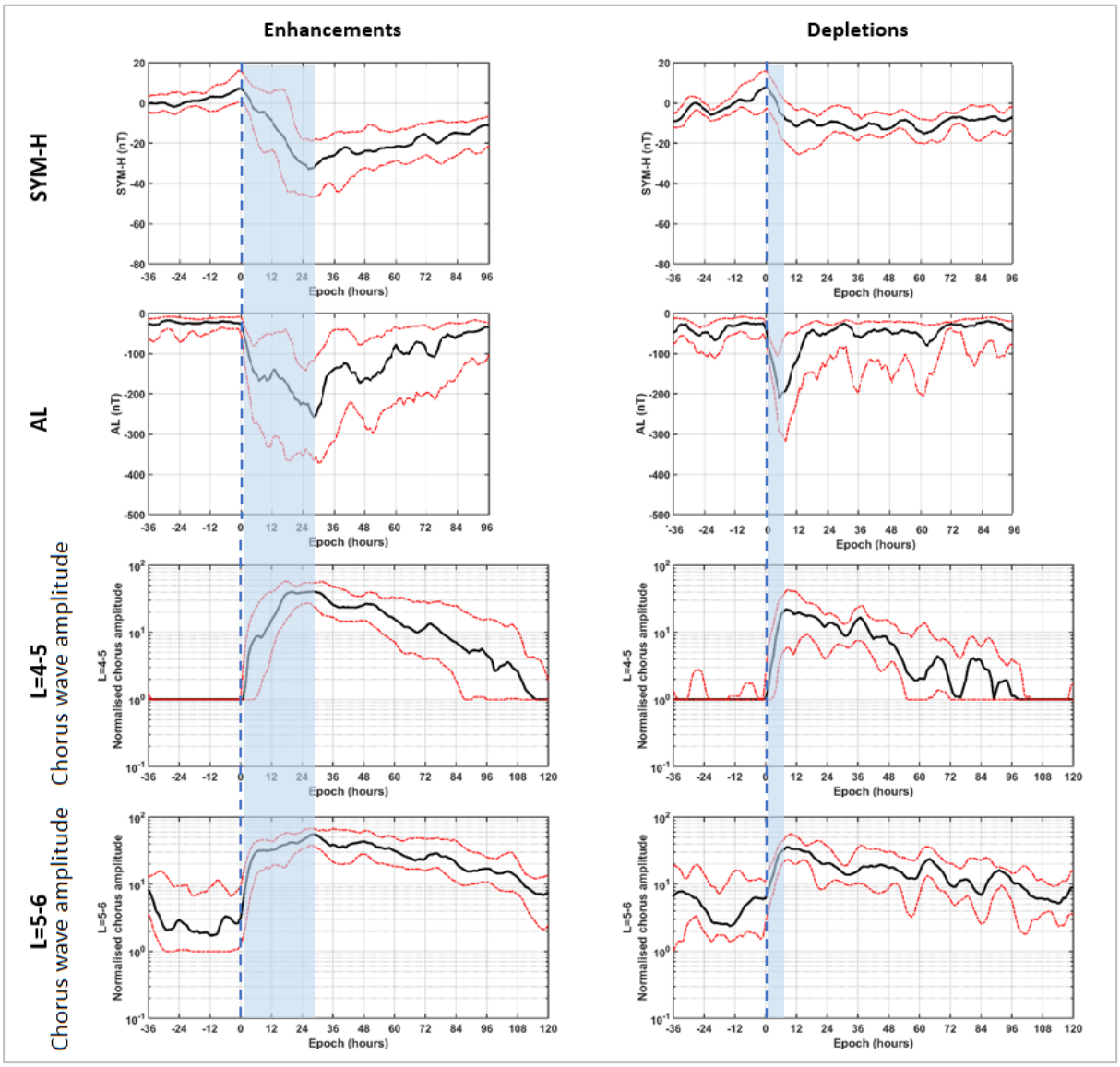

Figure 44 Comparison of some parameters from previous figures. Excluding L=3-4, where the chorus waves are obscured by the plasmapause location, there is a clear correlation between the chorus wave amplitude maximum value with the SYM-H and AL indices minimum values, which happen almost at the same time, denoted by a blue rectangle, but their duration is not correlated, as it is clearly greater than storm and substorm activity duration, especially in larger L, and mostly in depletion events.*

In summary, we can conclude that:

- Chorus waves appear at t_0 in both enhancement and depletion events, during enhanced geomagnetic storm and substorm activity, but decay with a smaller rate than the activity does.
- The chorus wave amplitude maximum value and duration increase with increasing L, in both enhancement and depletion events.
- In enhancement events the chorus wave activity is more pronounced and long-lasting over a broad L-shell region: at L=3-4 the waves appear more because of the more compressed plasmapause, at L=4-5 their duration is longer, but in L=5-6 their activity is comparable with that of depletion events.

5.2.2 Pc5 wave power vs L*

All plots depict the **Pc5 wave power [nT^2/Hz] versus L***. All values have been normalized to the median between 18-36 h before t_0, separately for the group of enhancement and of depletion events.

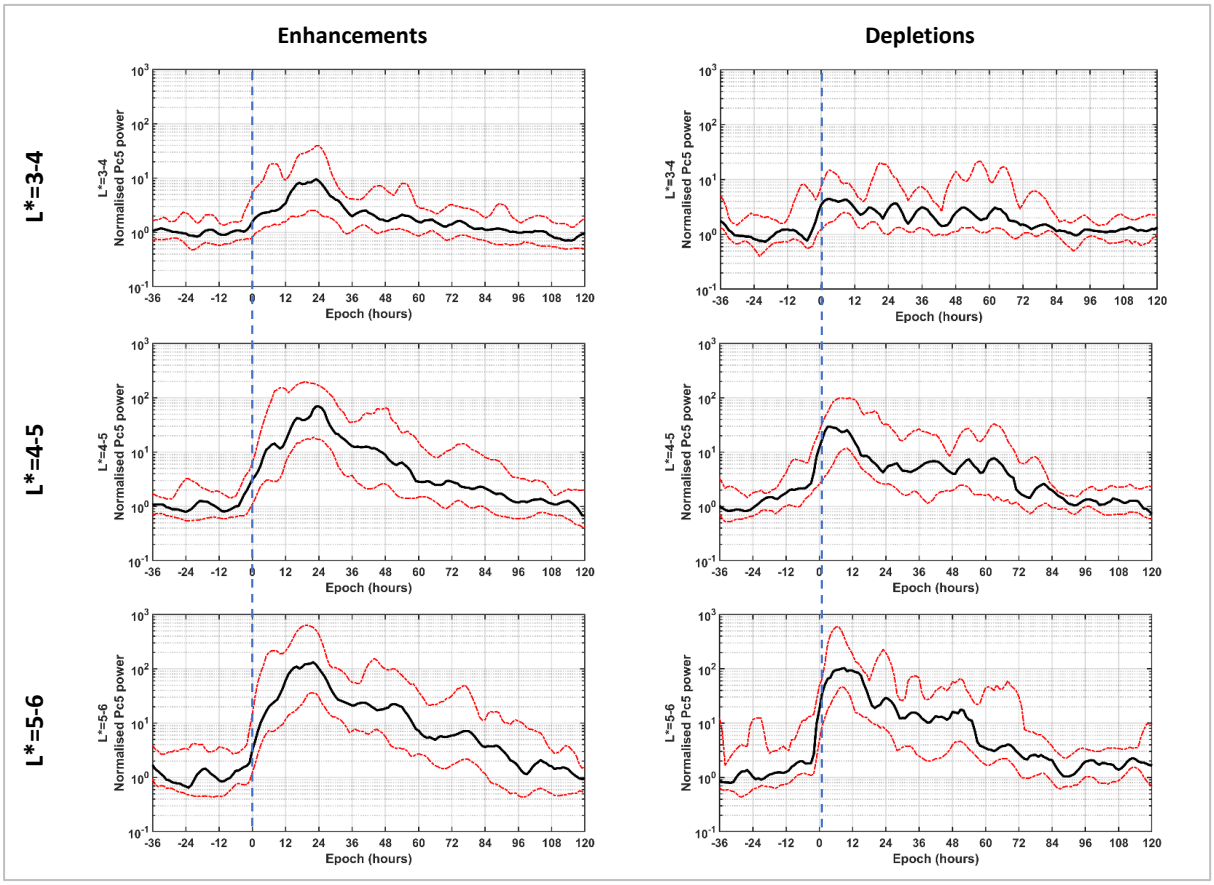

Figure 45 Superposed epoch analysis on Pc5 wave power values [nT^2/Hz] at different regions noted by L. Top to bottom: L*=3-4, L*=4-5, L*=5-6. Figure produced in MATLAB by the author.*

At **L*=3-4** the Pc5 waves exhibit a large difference between the two categories. They appear some hours before t_0, with a two-step increase and a maximum power of over 10 nT^2/Hz at 24h and return to their pre-event phase values after 84 h in enhancement events, but in depletion events their power increases at t_0 and fluctuates intensively around 2-10 nT^2 for 60h.

At **L*=4-5** the Pc5 waves also appear some hours before t_0, and exhibit a two-step increase with a maximum power of almost 100 nT^2/Hz at 24h and a gradual decrease until 96h in enhancement events, but in depletion events they reach a maximum power of over 20 nT^2 in 6h which then drops and continues to fluctuate around 10 nT^2 for 60h.

At **L*=5-6** the Pc5 waves again appear a while before t_0, with a two-step increase to a power of over 100 nT^2/Hz at 24h and a gradual decrease until 96h in enhancement events, but in depletion events it reaches a comparable maximum in 6h, then fluctuates to its pre-event phase values until 48h.

At each region, although the median shows different maximum values and duration, the behaviour of the quantiles seems similar for the two event categories. Still, in enhancement events, the maximum values are larger, and the Pc5 waves decrease with an almost uniform rate in comparison to depletion events where they decrease faster and reach plateaus that disappear at 60h. These results agree with those of Turner et al. [2013], who compared two storms in detail and showed that the one resulting in enhancement also presented more prolonged and enhanced Pc5 wave activity.

It appears that the Pc5 wave power exhibits a two-step increase at all regions in enhancement events, but just one step in depletion events. The first step covers 0-12h in both event categories, while the second step appears at 24h only in enhancement events.

Claudepierre et al. [2008] went a great deal in discussing the different mechanisms driving the excitation of Pc5 waves during geospace disturbances. He particularly focused on waves excited by pressure pulses without significant enhancement of solar wind speed, and waves excited by high values of solar wind speed which can lead to plasma instabilities (such as Kelvin-Helmholtz).

Our results show that the first peak (Figure 46) in Pc5 power (occurring in both event categories) correlates with the increase in P_{SW} that occurs at the same time. This indicates that the dynamic pressure pulses of the solar wind are the dominant mechanism for the excitation and propagation of global/stochastic Pc5 waves, as shown by Kepko et al. [2002]. The second peak (Figure 47) (occurring only in enhancement events) correlates with the increased V_{SW}, as they reach a maximum at the same time. This indicates that during enhancement events, Pc5 wave activity is excited by both mechanisms (pressure pulses and instabilities) while during depletion events pressure pulses are the dominant driver.

Also, for the waves to form, magnetic reconnection is needed at the dayside magnetopause. So we expect a correlation with Ey, as a rate of reconnection proxy, as explained before. It also looks that, for the second peak to form, the velocity needs to be over 500 km/s. In comparison (we show only L*=4-5 for simplicity in Figure 46 and Figure 47):

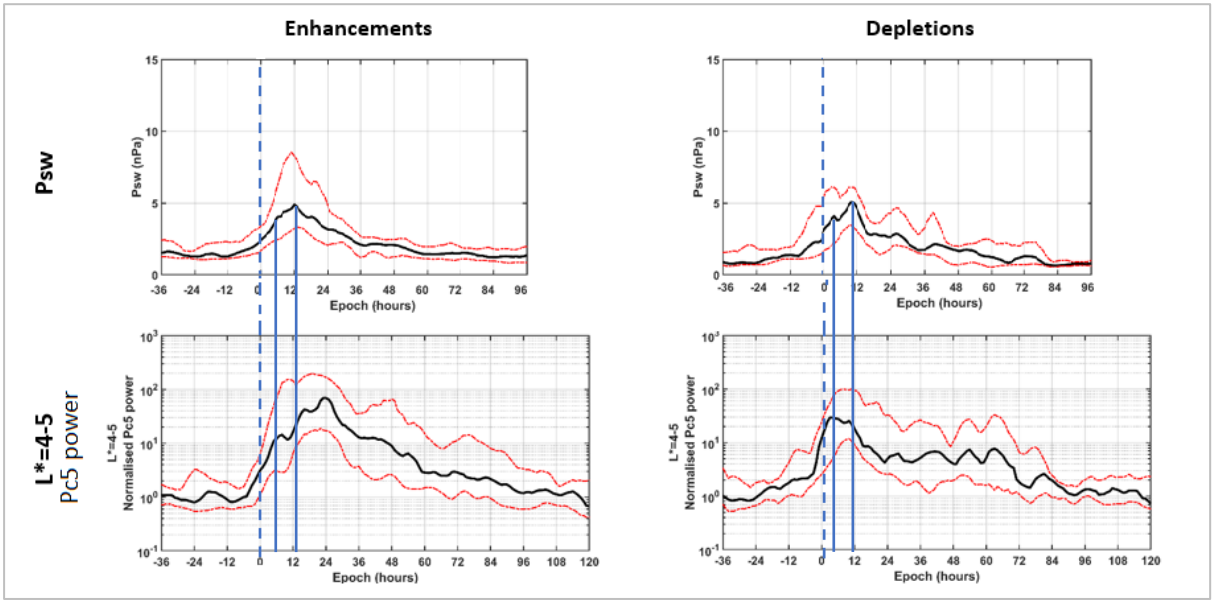

Figure 46 Comparison of some parameters from previous figures. The Pc5 wave power, shown only at L=4-5 for simplicity, form two peaks in enhancement and one peak in depletion events. The first peak, shows a great correlation with the P_{SW}, denoted here by vertical blue lines.*

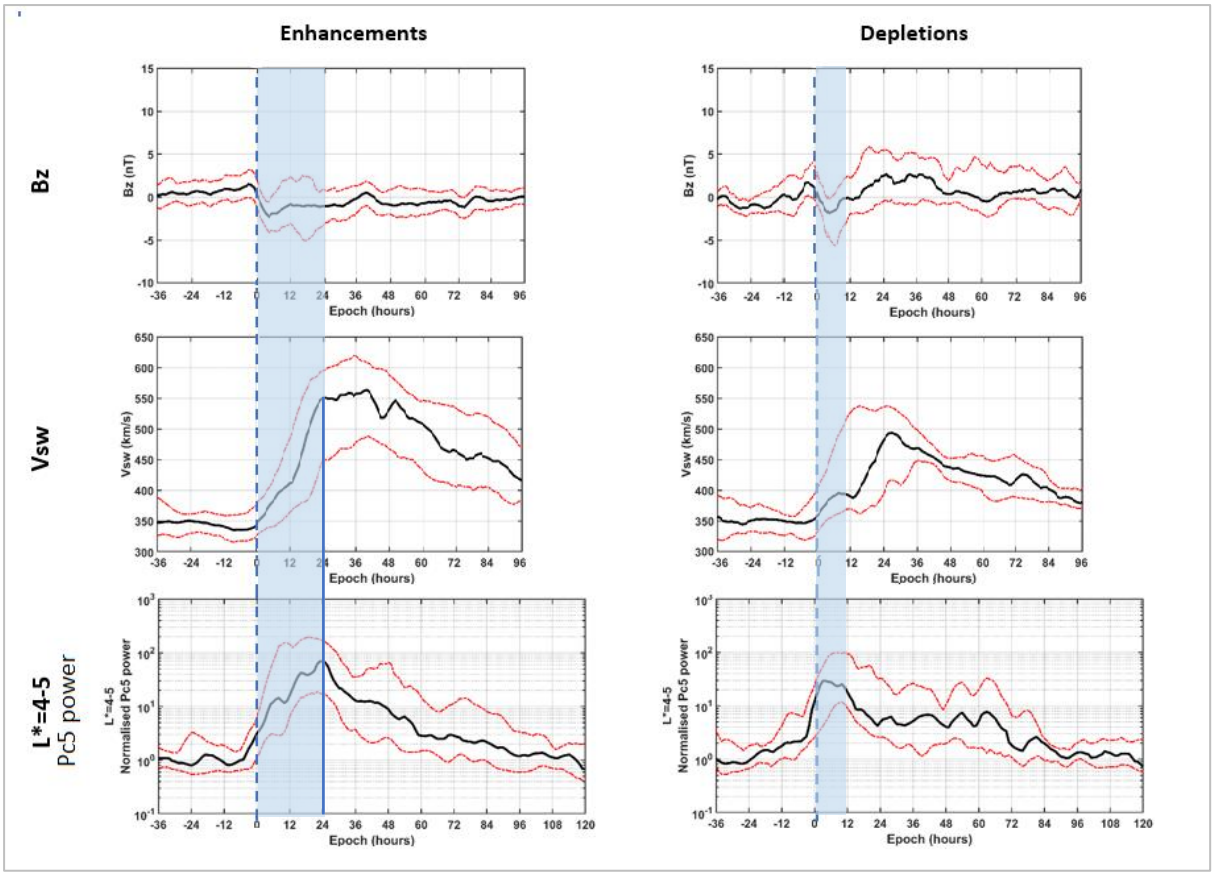

Figure 47 Comparison of some parameters from previous figures. The Pc5 waves, shown only at L=4-5 for simplicity, form two peaks in enhancement and one peak in depletion events. The second peak that forms only in enhancement events shows a great correlation with the V_{SW}, denoted by a vertical blue line. The blue rectangles indicate enhanced dayside reconnection.*

In summary, we can conclude that:

- Pc5 waves appear a while before t_0 in both event categories. During enhancement events their main drivers seem to be pressure pulses and instabilities generated by the enhanced solar wind velocity, while in depletion events, only pressure pulses are responsible for the excitation of Pc5 waves.
- The Pc5 wave power maximum value and duration increase with increasing L*, both in enhancement and depletion events.
- In enhancement events the Pc5 wave activity is more pronounced and longer-lasting: the wave power maximum value is less than 1 order of magnitude larger, is reached 24h after t_0, and the Pc5 wave activity decays slower, compared to depletion events, especially at L*=4-5. At L*=5-6 their activity is comparable.

5.3 PSD at L* vs μ

5.3.1 PSD at L*=3-4 vs μ

All plots depict the electron **PSD** $\left[\left(\frac{c}{MeV\ cm}\right)^3\right]$ **at L*=3-4 versus μ** $\left[\frac{MeV}{G}\right]$. All values have been normalized to the median between 18-36 h before t_0, separately for the group of enhancement and of depletion events.

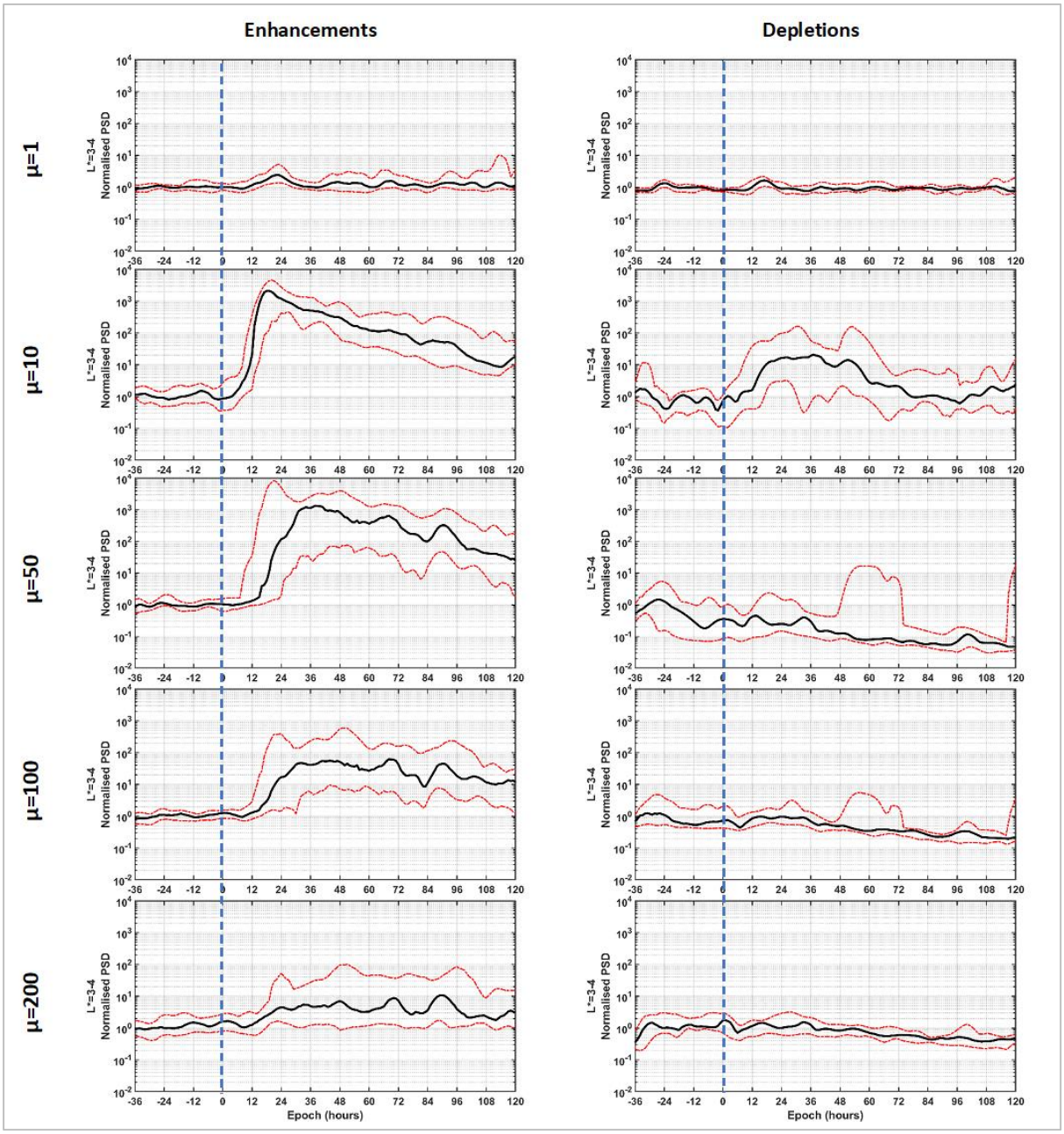

Figure 48 Superposed epoch analysis on the electron PSD [(c·MeV^{-1}·cm^{-1})^3] at L=3-4 for different values of μ [MeV/G]. Top to bottom: μ=1,10 [MeV/G] for source electrons, μ=50 [MeV/G] for source/seed electrons, μ=100 [MeV/G] for seed electrons, μ=200 [MeV/G] for seed/relativistic electrons. Figure produced in MATLAB by the author.*

For **source electrons** of **μ=1 [MeV/G]** or **E=1-10 [keV]**, the PSD shows no significant difference not only between the two event categories, but also in any variations in time. There is only one small peak in PSD almost 12-24h after t_0 for both event categories, and the quantiles are very close to the median, indicating that this behaviour is noticed in almost all the studied events.

We can say that none of the aforementioned mechanisms plays any important role on transporting or exciting these source electrons at L*=3-4, but we need to examine the rest of the regions.

For **source electrons** of **μ=10 [MeV/G]** or **E=10-100 [keV]**, the PSD shows a large difference between the two event categories. In enhancement events it starts increasing 4-6h after t_0, reaching an absolute maximum value of $2 \cdot 10^3$ $[(c \cdot MeV^{-1} \cdot cm^{-1})^3]$ at 12-18h, and then gradually decreasing even after 120h. In depletion events it starts increasing 12h after t_0, reaching a plateau value of around 20 $[(c \cdot MeV^{-1} \cdot cm^{-1})^3]$ until almost 40h and then decreasing to its pre-event state after 68h.

These source electrons appear at L*=3-4 before all other electrons and reach the largest maximum PSD value very quickly in enhancement events, 12h after t_0. They also appear in depletion events, but with a maximum smaller by 2 orders of magnitude. The mechanism responsible for the appearance of these source electron at this region, deeply inside the magnetosphere, is an injection caused by substorm activity. There seems to be a correlation between the PSD and the AL index, but we must examine all the other regions to arrive at a conclusion.

For **source/seed electrons** of **μ=50 [MeV/G]** or **E=50-400 [keV]**, the PSD also shows a large difference. In enhancement events it starts increasing 12-16h after t_0, reaching a maximum of around 10^3 $[(c \cdot MeV^{-1} \cdot cm^{-1})^3]$ at 30h, and then gradually decreasing even after 120h. In depletion events not only it does not increase, but it looks like gradually decreasing, with some exceptions from extreme events. Because this population covers source and seed electrons, we will not use it as an indication of a specific behaviour.

For **seed electrons** of **μ=100 [MeV/G]** or **E=100-600 [keV]**, the results are the almost the same as for μ=50 [MeV/G], with the enhancement event maximum being around 60 $[(c \cdot MeV^{-1} \cdot cm^{-1})^3]$ and then decreasing very slowly, almost in a plateau, when in depletion events the PSD is only decreasing.

For **seed/relativistic electrons** of **μ=200 [MeV/G]** or **E=200-1000 [keV]**, the results show almost no increase in both event categories. In enhancement events they reach only a value of 10 $[(c \cdot MeV^{-1} \cdot cm^{-1})^3]$, and in depletion events they still only decrease. Because this population covers seed and relativistic electrons, we will not use it as an indication of a specific behaviour.

The seed electrons of all μ values do appear in enhancement events, with a decreasing PSD maximum and increasing duration for increasing μ, but only seem to decrease in depletion events. The mechanism responsible for their appearance is either an injection directly from the plasma sheet caused by substorm activity, or the diffusion of electrons located at larger L*, or even the excitement of source electrons.

In summary, at L*=3-4, excluding the μ=1 [MeV/G] electrons, in enhancement events, for increasing μ, the PSD maximum decreases, its epoch increases and its decay rate decreases. The μ=10 [MeV/G] source electrons appear in both event categories, more prominently in enhancement events, but seed electrons appear mostly in enhancement events. We notice that the interquartile range is very narrow for μ=1 [MeV/G] in both categories, and for μ=100,200 [MeV/G] for depletion events, indicating an almost standard behaviour. We will try to detangle these conclusions by depicting the PSD in different ways in the following sections.

5.3.2 PSD at L*=4-5 vs μ

All plots depict the electron **PSD** $\left[\left(\frac{c}{MeV\ cm}\right)^3\right]$ **at L*=4-5 versus μ** $\left[\frac{MeV}{G}\right]$. All values have been normalized to the median between 18-36 h before t_0, separately for the group of enhancement and of depletion events.

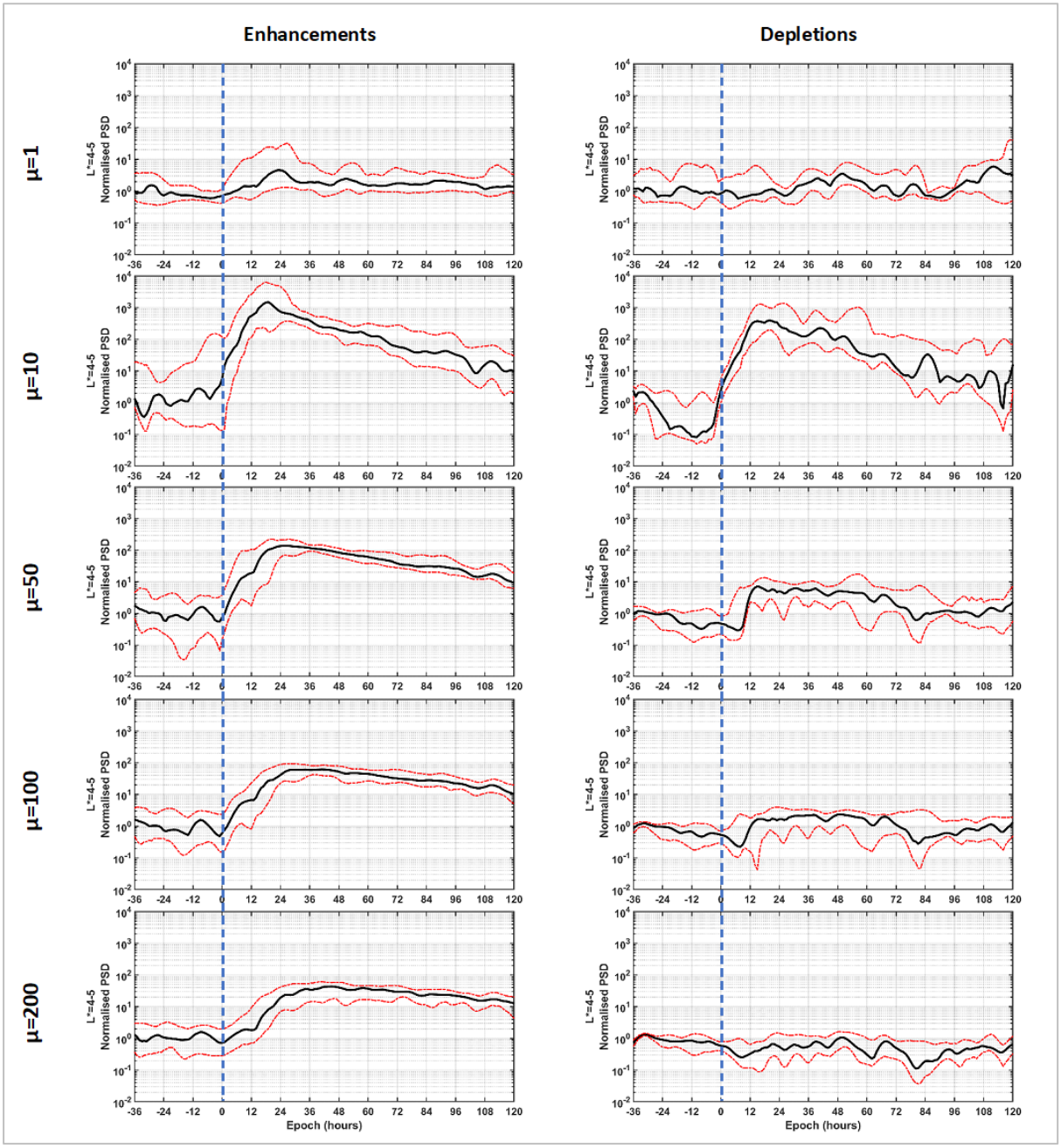

Figure 49 Superposed epoch analysis on the electron PSD [(c·MeV^{-1}·cm^{-1})^3] at L=4-5 for different values of μ [MeV/G]. Top to μ=1,10 [MeV/G] for source electrons, μ=50 [MeV/G] for source/seed electrons, μ=100 [MeV/G] for seed electrons, μ=200 [MeV/G] for seed/relativistic electrons. Figure produced in MATLAB by the author.*

For **source electrons** of **μ=1 [MeV/G]** or **E=1-10 [keV]**, the PSD again shows no significant difference between the two event categories. There is only one small peak in PSD 24h after t_0 in enhancement events, and many fluctuations in depletion events, none reaching values 1 order of magnitude larger than the pre-event phase values, so again the μ=1 [MeV/G] electrons seem insignificant, even though the interquartile range is not so narrow.

For **source electrons** of **μ=10 [MeV/G]** or **E=10-100 [keV]**, the PSD exhibits subtle differences between the two event categories. It starts increasing some hours before t_0 and reaches more than 10^3 $[(c\cdot MeV^{-1}\cdot cm^{-1})^3]$ at 18h in enhancement events, when in depletion events it starts increasing around t_0, reaches a smaller maximum around $4\cdot10^2$ $[(c\cdot MeV^{-1}\cdot cm^{-1})^3]$ at 12h. Then it gradually decreases until after 120h for both categories.

These source electrons appear at L*=4-5 before all other electrons and reach the largest maximum PSD very quickly, with a comparable maximum value for both event categories. Again, the mechanism responsible for the appearance of these source electron at this region is an injection caused by substorm activity. At this region there seems to be no correlation between their PSD and the AL index, as in both event categories they exhibit the same behaviour. We still must examine L*=5-6.

For **source/seed electrons** of **μ=50 [MeV/G]** or **E=50-400 [keV]**, the PSD shows a small difference. In enhancement events it starts increasing at t_0, reaching a maximum of 10^2 $[(c\cdot MeV^{-1}\cdot cm^{-1})^3]$ at 24h, and then gradually decreasing even after 120h. In depletion events it starts increasing 6h after t_0, reaching a plateau value of less than 10 $[(c\cdot MeV^{-1}\cdot cm^{-1})^3]$ until almost 60h and then decreasing to its pre-event state values after 72h. Because this population covers source and seed electrons, we will not use it as an indication of a specific behaviour.

For **seed electrons** of **μ=100 [MeV/G]** or **E=100-600 [keV]**, and for **seed/relativistic electrons** of **μ=200 [MeV/G]** or **E=200-1000 [keV]**, the results for enhancement events are almost the same as for μ=50 [MeV/G], but with maximum values of 80 and 30 $[(c\cdot MeV^{-1}\cdot cm^{-1})^3]$, but for depletion events there seems to be no increase, as the PSD fluctuates around 1 -3 $[(c\cdot MeV^{-1}\cdot cm^{-1})^3]$.

The seed electrons of μ=50 [MeV/G] appear in both event categories, but in depletion events they do with a maximum smaller by less than 1 order of magnitude. The seed electrons of μ=100 [MeV/G] and μ=200 [MeV/G] do appear in enhancement events, with a decreasing PSD maximum for increasing μ, but almost only decrease in depletion events. The mechanism responsible for their appearance is either an injection directly from the plasma sheet caused by substorm activity, or the diffusion of electrons located at larger L*, or even the excitement of source electrons.

In summary, at L*=4-5, excluding the μ=1 [MeV/G] electrons, in enhancement events, for increasing μ, the PSD maximum decreases, its epoch increases and its decay rate decreases. The μ=10 [MeV/G] source electrons appear in both event categories with comparable magnitudes, seed electrons of μ=50 [MeV/G] appear more prominently in enhancement events, but seed electrons of μ=100 [MeV/G] and μ=200 [MeV/G] appear only in enhancement events. We notice that the interquartile range is very narrow for μ=50,100,200 [MeV/G] in enhancement events, indicating an almost standard behaviour.

5.3.3 PSD at L*=5-6 vs μ

All plots depict the electron **PSD** $\left[\left(\frac{c}{MeV\ cm}\right)^3\right]$ **at L*=5-6 versus μ** $\left[\frac{MeV}{G}\right]$. All values have been normalized to the median between 18-36 h before t_0, separately for the group of enhancement and of depletion events.

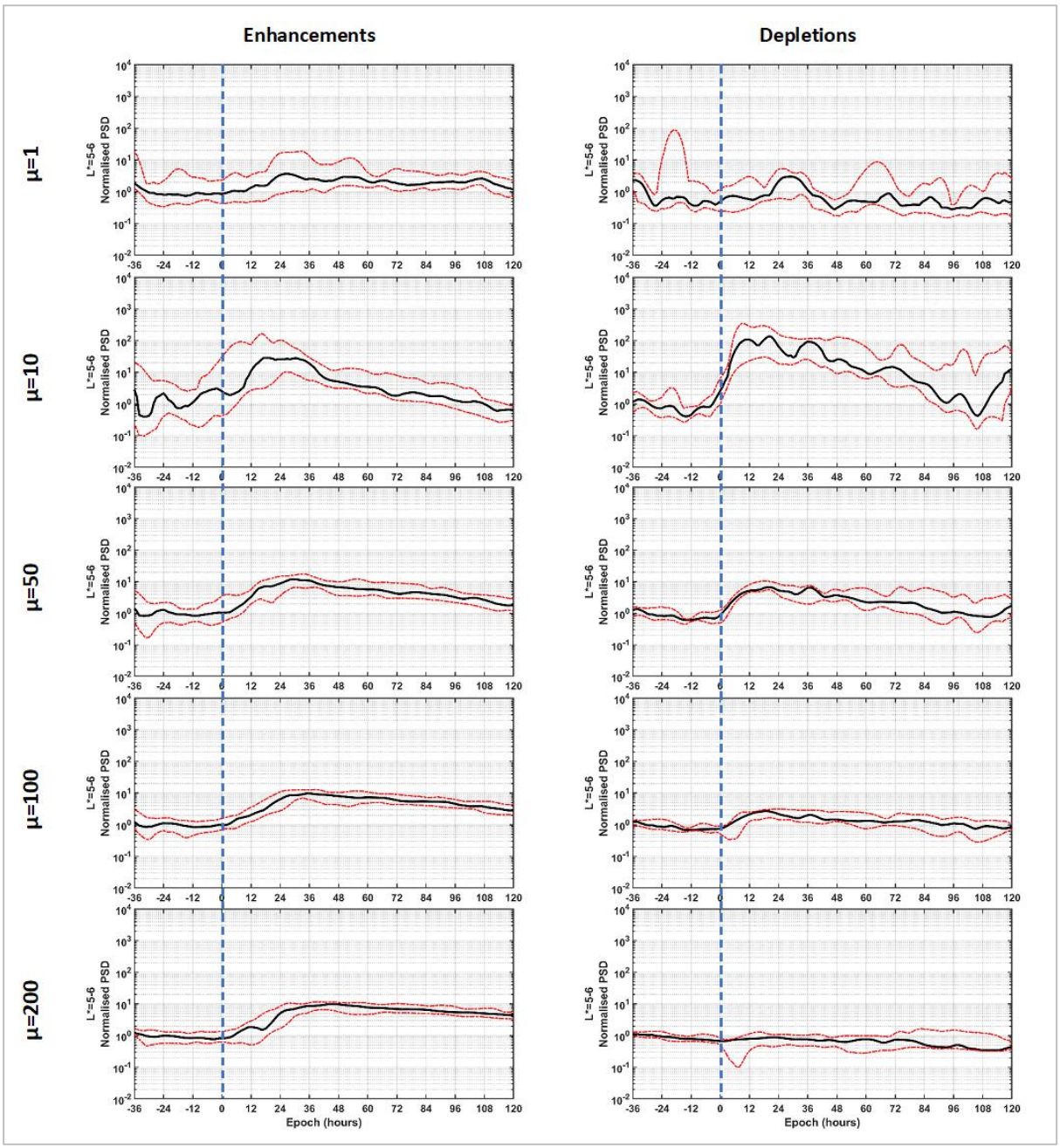

Figure 50 Superposed epoch analysis on the electron PSD [(c·MeV^{-1}·cm^{-1})^3] at L=5-6 for different values of μ [MeV/G]. Top to bottom: μ=1,10 [MeV/G] for source electrons, μ=50 [MeV/G] for source/seed electrons, μ=100 [MeV/G] for seed electrons, μ=200 [MeV/G] for seed/relativistic electrons. Figure produced in MATLAB by the author.*

For **source electrons** of **μ=1 [MeV/G]** or **E=1-10 [keV]**, the PSD again shows no significant difference between the two event categories. There is only one small peak in PSD 24h after t_0 in enhancement events, and many fluctuations in depletion events, none reaching values 1 order of magnitude larger than the pre-event phase values, so we can fully conclude that the μ=1 [MeV/G] electrons are considered insignificant. This will be more visible examining only μ=1 [MeV/G] electrons, which we do in the following sections.

For **source electrons** of **μ=10 [MeV/G]** or **E=10-100 [keV]**, the PSD again shows a large difference between the two event categories, but indeed an interesting one. It starts increasing 6h after t_0, reaches 30 $[(c\cdot MeV^{-1}\cdot cm^{-1})^3]$ at 18h, and returns to its pre-event state values in 36h in enhancement events. On the other hand, in depletion events it starts increasing some hours before t_0, reaches 10^2 $[(c\cdot MeV^{-1}\cdot cm^{-1})^3]$ in only 6h, then gradually decreases until after 96h.

These source electrons appear at L*=5-6 before all other electrons and reach the largest maximum PSD very quickly in depletion events, 6h after t_0. They also appear in enhancement events, even a while before t_0, but reaching a maximum value smaller by 1 order of magnitude. The mechanism responsible for the appearance of these source electron at this region is an injection caused by substorm activity. This time there even seems to be an anti-correlation between their PSD and the AL index. So, to finally reach a conclusion, we have to examine only μ=10 [MeV/G] electrons in every magnetospheric region, which we do in the following sections.

For **source/seed electrons** of **μ=50 [MeV/G]** or **E=50-400 [keV]**, for **seed electrons** of **μ=100 [MeV/G]** or **E=100-600 [keV]**, and for **seed/relativistic electrons** of **μ=200 [MeV/G]** or **E=200-1000 [keV]**, the results for enhancement events are almost the same, with maximum values of around 10 $[(c\cdot MeV^{-1}\cdot cm^{-1})^3]$ at 30h which return to their pre-event state values after more than 96h in enhancement events, but with a maximum of 10, 3 and 1 $[(c\cdot MeV^{-1}\cdot cm^{-1})^3]$ respectively in depletion events, indicating almost no increase. We also note the very narrow interquartile range.

The seed electrons of μ=50 [MeV/G] do appear in both event categories with a comparable but very small maximum. The seed electrons of μ=100 [MeV/G] and μ=200 [MeV/G] do appear in enhancement events with an also comparable maximum, but almost only decrease in depletion events. So, we can say that they are almost insignificant in this region.

In summary, at L*=5-6, excluding the μ=1 [MeV/G] electrons, in enhancement events, for increasing μ, the PSD maximum decreases, its epoch increases and its decay rate decreases. The μ=10 [MeV/G] source electrons appear in both event categories, but more prominently in depletion events. The μ=50 [MeV/G] source/seed electrons are also comparable in both event categories, but the seed electrons of μ=100 and μ=200 [MeV/G] appear only in enhancement events.

5.4 PSD for μ vs L *

5.4.1 PSD for μ=1 vs L*

All plots depict the electron **PSD** $\left[\left(\frac{c}{MeV\ cm}\right)^3\right]$ **for source electrons of μ=1** $\left[\frac{MeV}{G}\right]$ **or E=1-10 [keV] versus L***. All values have been normalized to the median between 18-36 h before t_0, separately for the group of enhancement and of depletion events.

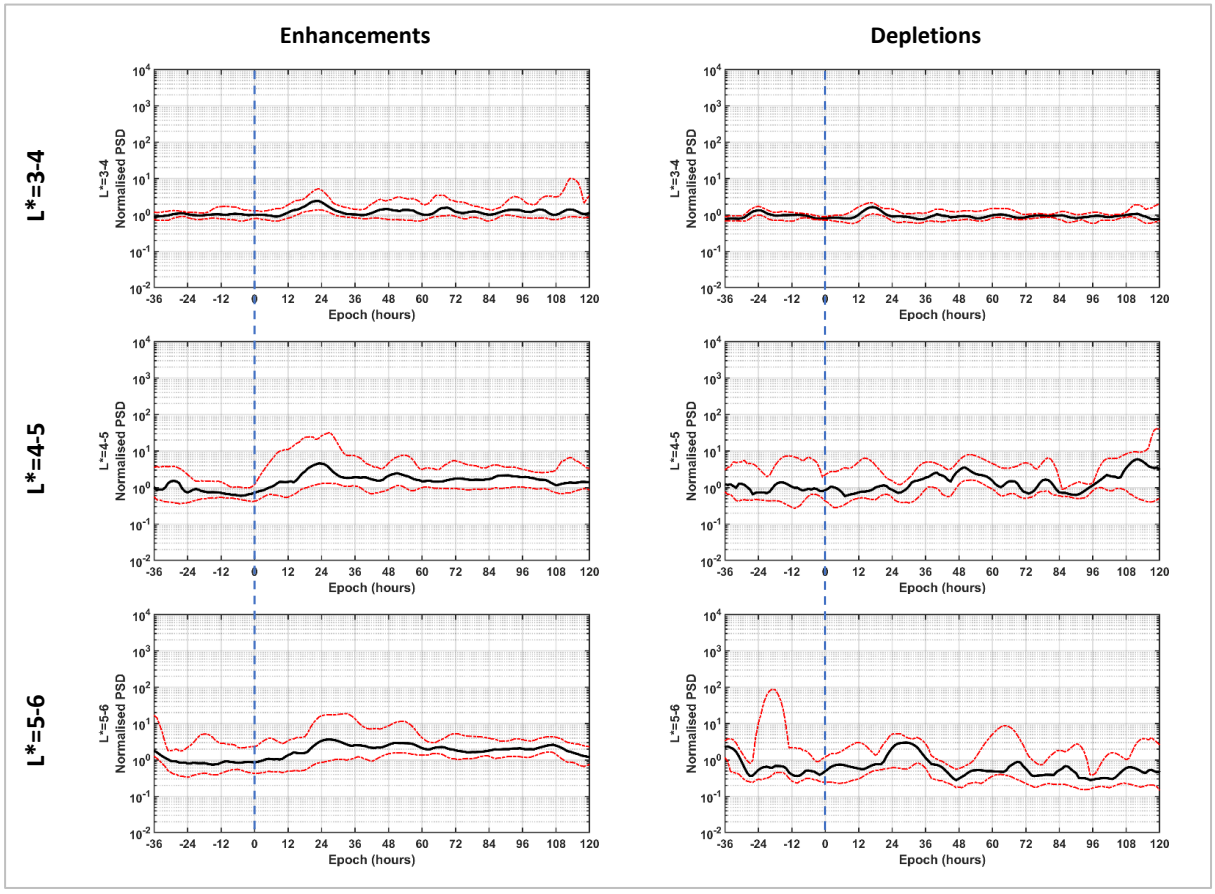

Figure 51 Superposed epoch analysis on the electron PSD [(c·MeV^{-1}·cm^{-1})^3] for source electrons of μ=1 [MeV/G] for different values of L. Top to bottom: L*=3-4, L*=4-5, L*=5-6. Figure produced in MATLAB by the author.*

In this depiction, it is now clear that the source electrons of μ=1 [MeV/G] are insignificant, as they always fluctuate around a rather small value of ~0-10 [(c·MeV^{-1}·cm^{-1})^3], and somewhat higher for increasing L and their behaviour is similar for both the enhancement and depletion events.

So, we can conclude that:

- The source electrons of μ=1 [MeV/G] do not appear to be affected by any kind of disturbance and in turn to have any effect in the variation of seed or relativistic electrons in enhancement or depletion events.

5.4.2 PSD for μ=10 vs L*

All plots depict the electron **PSD** $\left[\left(\frac{c}{MeV\ cm}\right)^3\right]$ **for source electrons of μ=10** $\left[\frac{MeV}{G}\right]$ **or E=10-100 [keV] versus L***. All values have been normalized to the median between 18-36 h before t_0, separately for the group of enhancement and of depletion events.

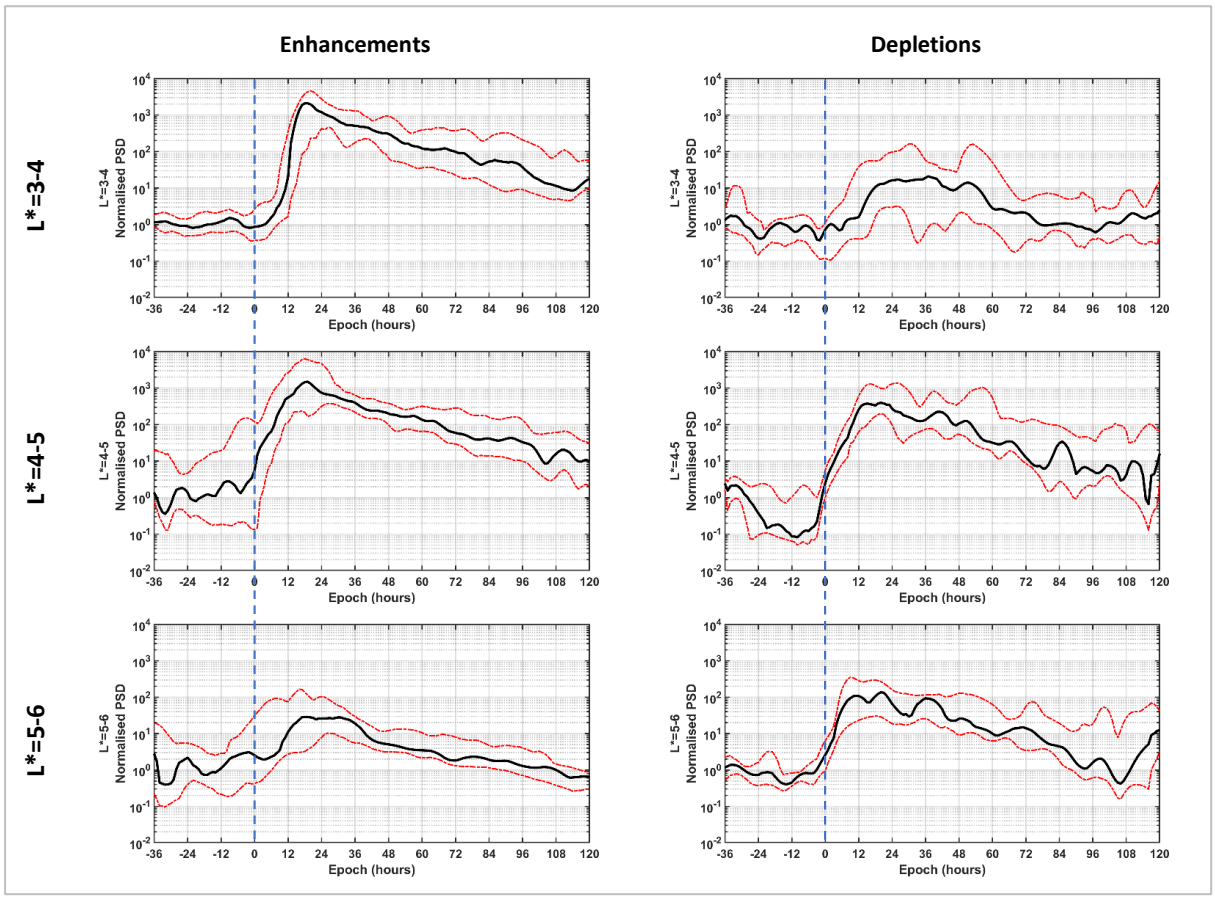

Figure 52 Superposed epoch analysis on the electron PSD [(c·MeV^{-1}·cm^{-1})^3] for source electrons of μ=10 [MeV/G] for different values of L. Top to bottom: L*=3-4, L*=4-5, L*=5-6. Figure produced in MATLAB by the author.*

This depiction is very interesting, in ways we mentioned before. It shows that the source electrons of μ=10 [MeV/G] always appear in both event categories and at every studied region of the magnetosphere, but with different maximum values and duration. They appear with a maximum of around $2 \cdot 10^3$ $[(c \cdot MeV^{-1} \cdot cm^{-1})^3]$ at L*=3-5 (more inward) in enhancement events, and around $2 \cdot 10^2$ $[(c \cdot MeV^{-1} \cdot cm^{-1})^3]$ but at L*=4-6 (more outward) in depletion events, but with much smaller maximum values in all other cases. Also, in enhancement events, they remain enhanced for a longer time period than in depletion events. They are overall so comparable in the two event categories, that we cannot use their appearance or their magnitude to predict the appearance of seed or relativistic electrons.

We also note that, in the enhancement event category, many extreme events are included. This might be the reason why these source electrons are not enhanced at L*=5-6, as in extreme events the last closed drift shell can be located more inward, appearing as a depleted electron flux, and thus PSD, in this area, as also shown by Olifer et al. [2018].

So, we can conclude that:

- Source electrons of μ=10 [MeV/G] appear in both enhancement and depletion events with a comparable mean maximum value.
- The injections transporting the source electrons of μ=10 [MeV/G] to the inner magnetosphere are more effective in enhancement events, together with the more compressed plasmapause, bringing the electrons even at L*=3-4 with a more than 2 orders of magnitude difference compared to that of depletion events at the same region. At L*=4-5 they are comparable, and at L*=5-6 they are more pronounced in depletion events, as a result of the open drift shells in extreme events.
- The appearance of source electrons of μ=10 [MeV/G] does not in any way act as a proxy for the appearance of seed or relativistic electrons, at least for relativistic electrons of μ=900 [MeV/G] at L*>4.5, as of which we sorted the events into the two categories.

5.4.3 PSD for μ=50 vs L*

All plots depict the electron **PSD** $\left[\left(\frac{c}{MeV\ cm}\right)^3\right]$ **for source/seed electrons of μ=50** $\left[\frac{MeV}{G}\right]$ **or E=50-400 [keV] versus L***. All values have been normalized to the median between 18-36 h before t_0, separately for the group of enhancement and of depletion events.

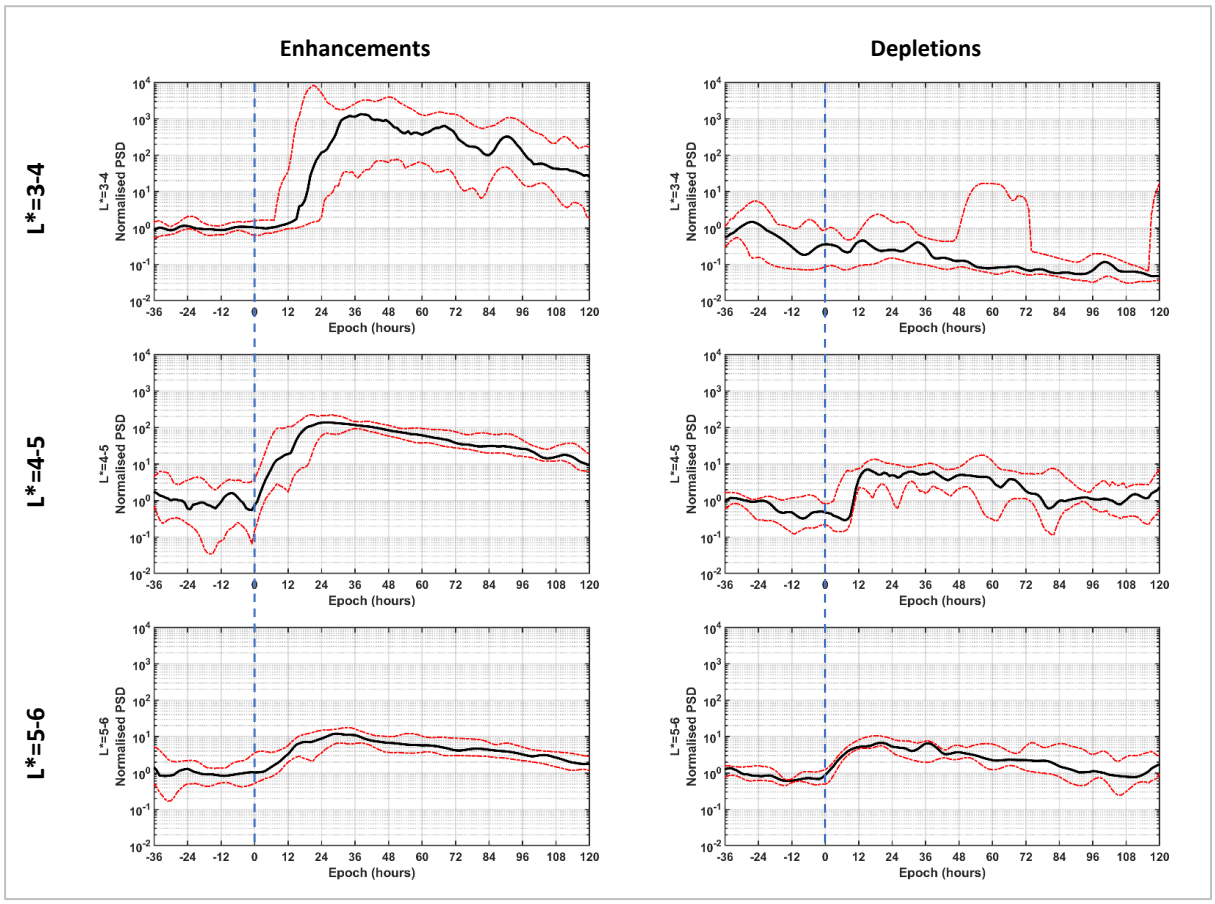

Figure 53 Superposed epoch analysis on the electron PSD [(c·MeV^{-1}·cm^{-1})^3] for source/seed electrons of μ=50 [MeV/G] for different values of L. Top to bottom: L*=3-4, L*=4-5, L*=5-6. Figure produced in MATLAB by the author.*

This depiction follows the previous, in the way that source/seed electrons of μ=50 [MeV/G] appear more inward for enhancement and more outward for depletion events. They appear with a maximum of over 10^3 [$(c \cdot MeV^{-1} \cdot cm^{-1})^3$] at L*=3-4 and 10^2 [$(c \cdot MeV^{-1} \cdot cm^{-1})^3$] at L*=4-5 in enhancement events, but are show very small increase or only decrease in all other cases.

Considering the previous depiction of the μ=10 [MeV/G] source electrons, we can see that in enhancement events, where these source electrons where abundant at L*=3-5, seed electrons of μ=50 [MeV/G] also appear, with a fraction of their maximum values (1/2 at L*=3-4, 1/10 at L*=4-5). On the other hand, in depletion events, where the μ=10 [MeV/G] electrons where also abundant but located at L*=4-6 with a maximum only 1 order of magnitude smaller than those in the enhancement events, the μ=50 [MeV/G] electrons do show a small increase in comparison to those at L*=3-4, but never reach values larger than 1 order of magnitude compared to the pre-event phase values, therefore considered as insignificant. This means that the appearance alone of source electrons does not necessarily lead to the appearance of seed electrons, so there must be additional mechanisms responsible. These results agree with those of Jaynes et al. [2015], who note that the source and the seed electron populations emerge independently from substorm activity.

Also important is the fact that the interquartile range becomes very narrow with increasing L*, in both event categories, but mostly for enhancement events, which means that the μ=50 [MeV/G] electrons have a standard behaviour, even though we do not consider them as purely seed electrons, which we do for the μ=100 [MeV/G] electrons, studied in the next section.

So, we can conclude that:

- Source/seed electrons of μ=50 [MeV/G] appear mostly in enhancement events. This means that the appearance of these electrons acts as a proxy for the appearance of relativistic electrons, at least for relativistic electrons of μ=900 [MeV/G] at L*>4.5, as of which we sorted the events into the two categories. But, because this population covers source and seed electrons, we will not use it as an indication of a specific behaviour.
- The injections transporting the source/seed electrons of μ=50 [MeV/G] to the inner magnetosphere are more effective in enhancement events, together with the more compressed plasmapause, bringing the electrons even at L*=3-4 with a more than 3 orders of magnitude difference compared to that of depletion events at the same region. At L*=4-5 they reach a maximum 1 order of magnitude larger, and at L*=5-6 they are comparable.
- The appearance of source/seed electrons of μ=50 [MeV/G] does not depend on the appearance of source electrons alone, but additional mechanisms are important. So, they either get directly injected from the plasma sheet as an effect of substorm activity, or they are comprised by diffused electrons previously located at larger L*, source electrons or other.

5.4.4 PSD for μ=100 vs L*

All plots depict the electron **PSD** $\left[\left(\frac{c}{MeV\ cm}\right)^3\right]$ **for seed electrons of μ=100** $\left[\frac{MeV}{G}\right]$ **or E=100-600 [keV] versus L***. All values have been normalized to the median between 18-36 h before t_0, separately for the group of enhancement and of depletion events.

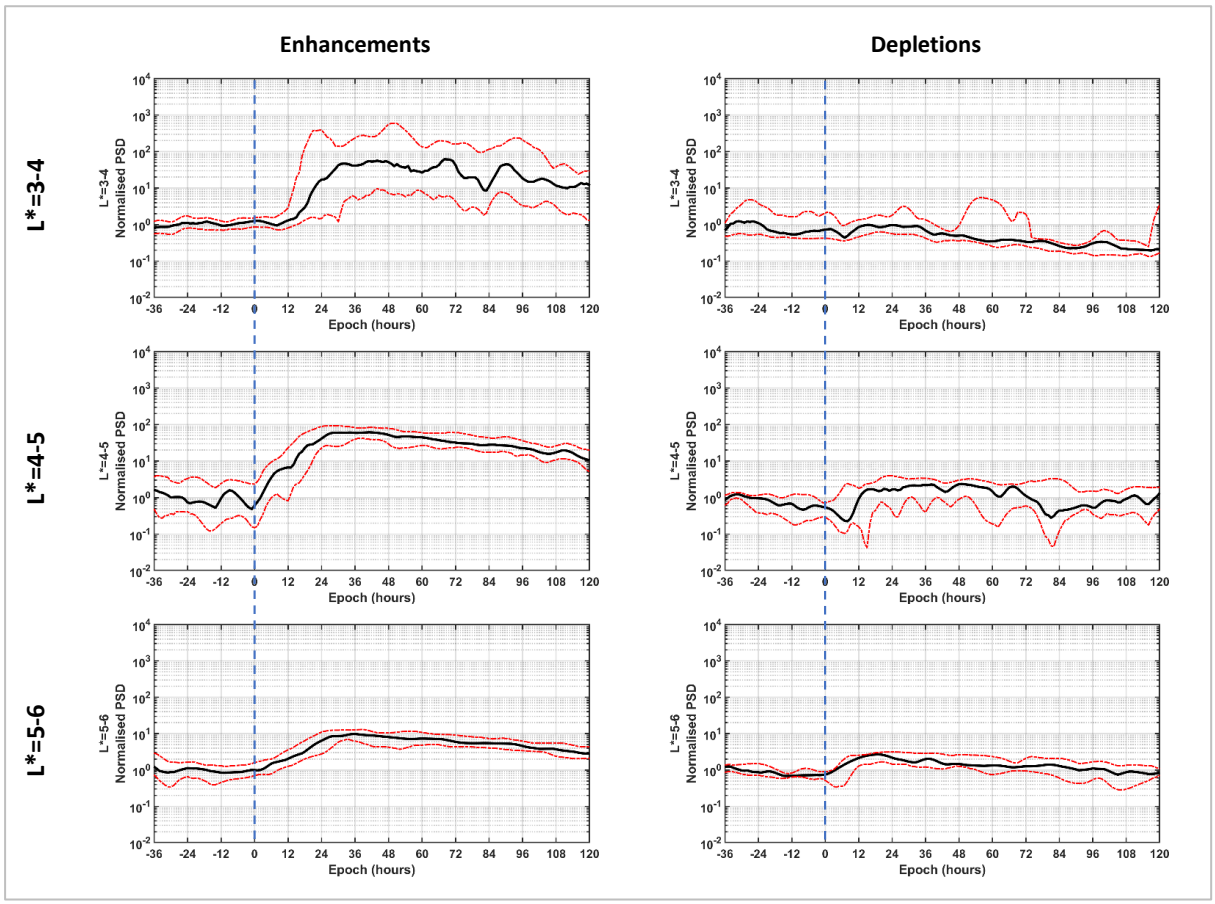

Figure 54 Superposed epoch analysis on the electron PSD [(c·MeV^{-1}·cm^{-1})^3] for seed electrons of μ=100 [MeV/G] for different values of L. Top to bottom: L*=3-4, L*=4-5, L*=5-6. Figure produced in MATLAB by the author.*

Here we can see that the seed electrons of μ=100 [MeV/G] appear with a maximum of around or more than 10^2 [$(c \cdot MeV^{-1} \cdot cm^{-1})^3$] at L*=3-4,4-5 in enhancement events, but are almost insignificant in all the other cases, as they never reach values 1 order of magnitude larger than those of the pre-event phase.

Considering the previous depictions for source/seed electrons of μ=50 [MeV/G] we can see a comparable behaviour, but with a bit smaller maximum values, almost by 1 order of magnitude. This is expected as the μ=100 [MeV/G] electrons correspond to larger energies, so they are statistically less possible to get enhanced. Also, this similarity is explained be the electron energies, as at smaller L* the μ=50 [MeV/G] electrons are seed electrons.

In this case of μ=100 [MeV/G], we can compare our results to those of Katsavrias et al. [2019] (Figure 55), where we indeed see a comparable behaviour, thus confirming that the seed electrons are more pronounced in enhancement events, even though the L* bins and the t_0 definition are different. For comparison:

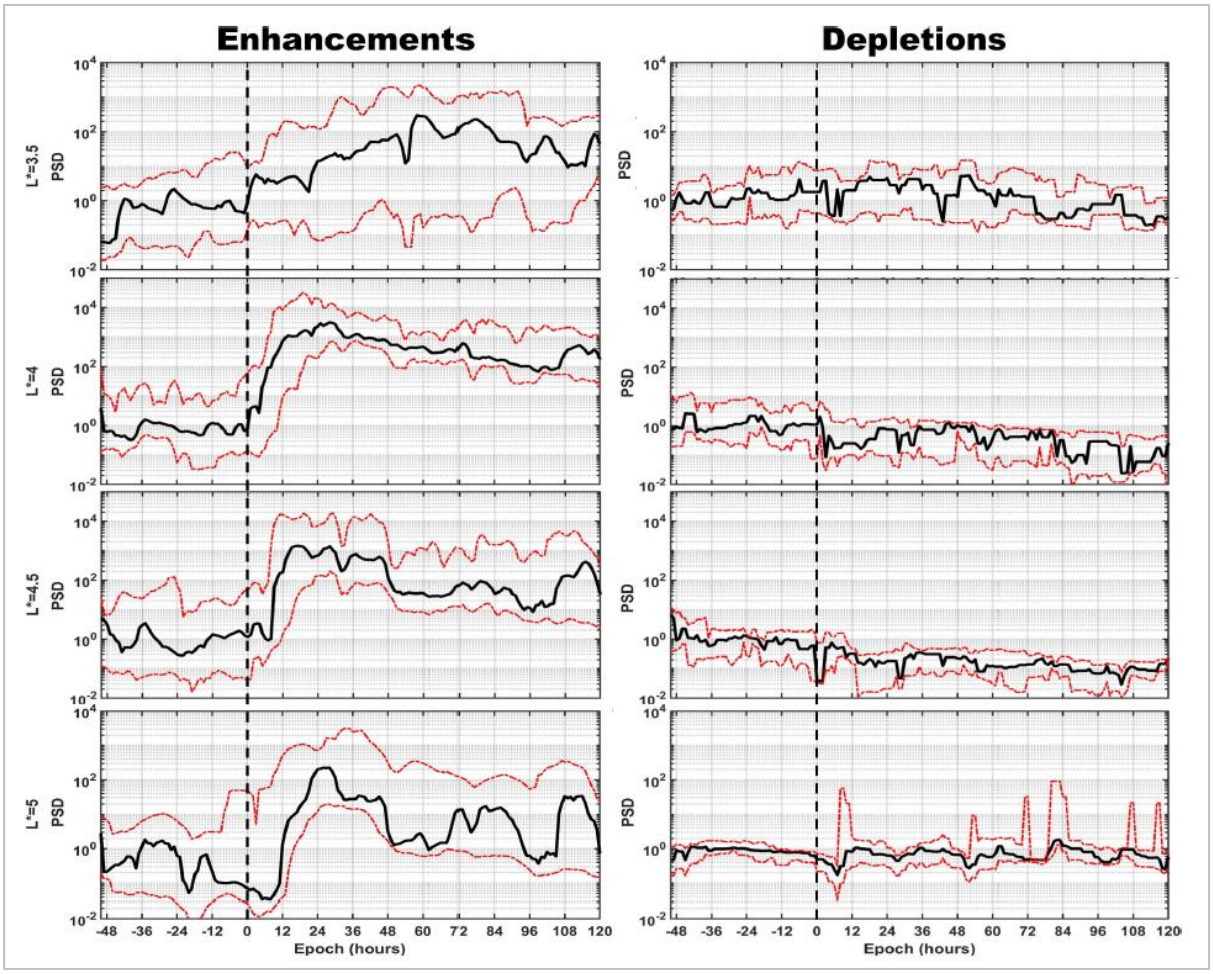

Figure 55 Evolution of the average PSD [$(c \cdot MeV^{-1} \cdot cm^{-1})^3$] for seed electrons of μ=100 [MeV/G] at the regions of L=3.5, 4, 4.5 and L*=5, for enhancement and depletion events, as studied by Katsavrias et al. [2019]. It is clear that these seed electrons are pronounced only in enhancement events, when in depletion events they seem stable or decreasing, agreeing with our results, which only seem a little different because of the different L* binning and the different definition of the key time t_0. Figure by Katsavrias et al. [2019].*

So, we can conclude that:

- Seed electrons of μ=100 [MeV/G] appear only in enhancement events, so they act as a proxy for the appearance of relativistic electrons, at least for relativistic electrons of μ=900 [MeV/G] at L*>4.5, as of which we sorted the events into the two categories.
- The injections transporting the seed electrons of μ=100 [MeV/G] to the inner magnetosphere are more effective in enhancement events, together with the more compressed plasmapause, bringing the electrons even at L*=3-4 with a more than 3 orders of magnitude difference compared to that of depletion events at the same region. At L*=4-5 they reach a maximum 1 order of magnitude larger, and at L*=5-6 they are comparable.
- The appearance of seed electrons of μ=100 [MeV/G] does not depend on the appearance of source electrons alone, but additional mechanisms are important. So, they either get directly injected from the plasma sheet as an effect of substorm activity, or they are comprised by diffused electrons previously located at larger L*, source electrons or other.
- The seed electrons of μ=100 [MeV/G] and μ=50 [MeV/G] follow the same behaviour, mostly in smaller L* values where the μ=50 [MeV/G] are also seed electrons, so they rely on the same mechanisms.

5.4.5 PSD for μ=200 vs L*

All plots depict the electron **PSD** $\left[\left(\frac{c}{MeV\ cm}\right)^3\right]$ **for seed/relativistic electrons of μ=200** $\left[\frac{MeV}{G}\right]$ **or E=200-1000 [keV] versus L***. All values have been normalized to the median between 18-36 h before t_0, separately for the group of enhancement and of depletion events.

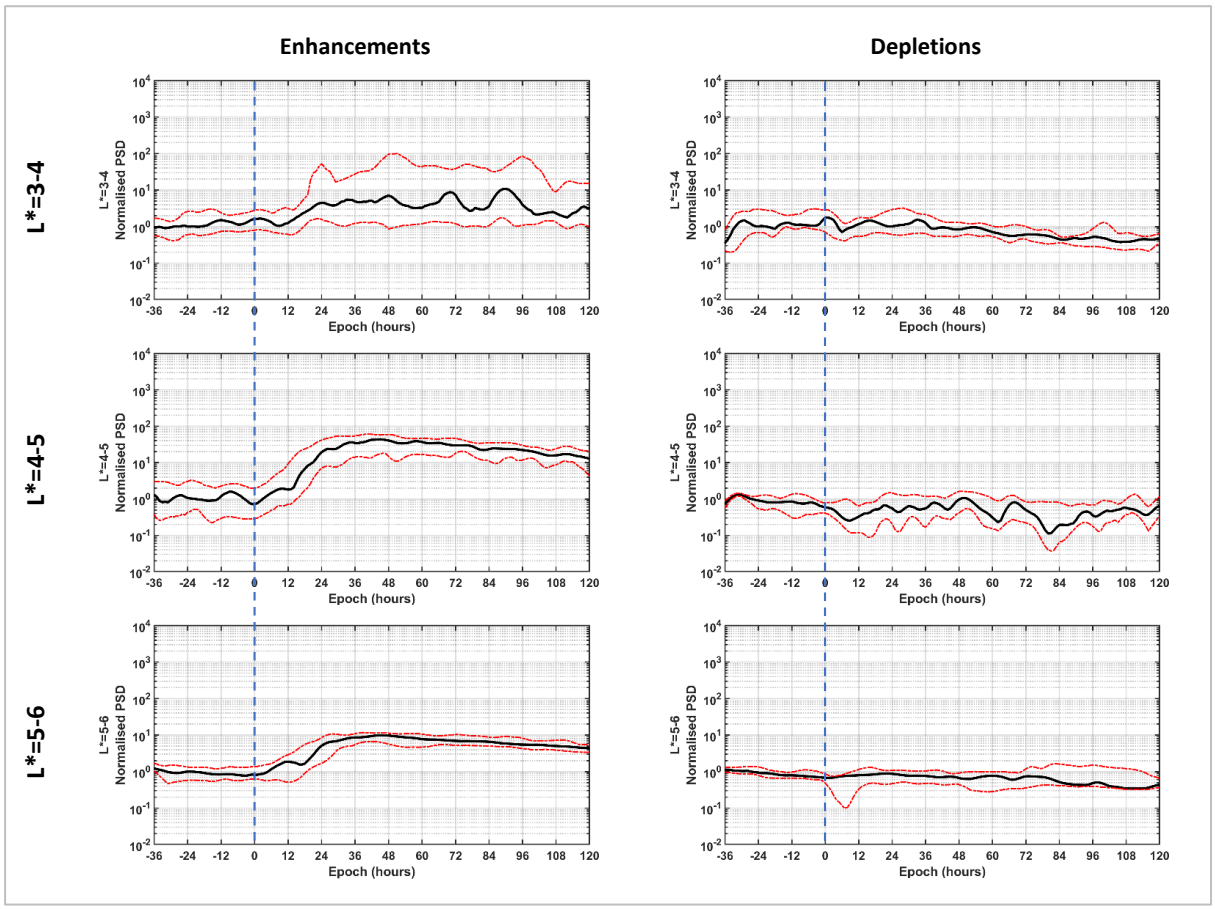

Figure 56 Superposed epoch analysis on the electron PSD [(c·MeV^{-1}·cm^{-1})^3] for seed/relativistic electrons of μ=200 [MeV/G] for different values of L. Top to bottom: L*=3-4, L*=4-5, L*=5-6. Figure produced in MATLAB by the author.*

The seed electrons of μ=200 [MeV/G] appear with a maximum value of 40 [$(c \cdot MeV^{-1} \cdot cm^{-1})^3$] at L*=4-5 in enhancement events, but are insignificant in all the other cases, according to the previous criteria.

Considering the two previous depictions for source/seed electrons of μ=50 [MeV/G] and seed electrons of μ=100 [MeV/G], we can still see a comparable behaviour, but with even smaller maximum values (almost 1 order of magnitude). This is also expected as the μ=200 [MeV/G] electrons are even less statistically possible to get enhanced.

In this case, at smaller L* the μ=200 [MeV/G] electrons are relativistic electrons, but we cannot compare our results with those of Katsavrias et al. [2019], as they only study μ=900 [MeV/G] relativistic electrons. We note that at L*=3-4 where they are considered relativistic electrons, the interquartile region is very broad, showing a dependence on each event characteristics and ability of injecting them to this region.

So, we can conclude that:

- Seed/relativistic electrons of μ=200 [MeV/G] appear only in enhancement events, so they can act as a proxy for the appearance of relativistic electrons, at least for relativistic electrons of μ=900 [MeV/G] at L*>4.5, as of which we sorted the events into the two categories.
- The injections transporting the seed/relativistic electrons of μ=200 [MeV/G] to the inner magnetosphere are more effective in enhancement events, together with the more compressed plasmapause, bringing the electrons even at L*=3-4 but with only 1 order of magnitude difference compared to that of depletion events at the same region. At L*=4-5 they reach a maximum 2 orders of magnitude larger, and at L*=5-6 only 1 order of magnitude larger.
- The appearance of seed/relativistic electrons of μ=200 [MeV/G] does not depend on the appearance of source electrons alone, but additional mechanisms are important. So, they either get directly injected from the plasma sheet as an effect of substorm activity, or they are comprised by diffused electrons previously located at larger L*, source electrons or other.
- The seed electrons of μ=200 [MeV/G] and μ=100 [MeV/G] follow the same behaviour, mostly in larger L* values where the μ=200 [MeV/G] are also seed electrons, so they rely on the same mechanisms.

5.5 L or L* vs Waves and PSD for comparison

In the previous sections we reached some general conclusions for each PSD group. Some of these where:

- That the μ=1 [MeV/G] electrons are clearly insignificant.
- That the μ=10 [MeV/G] are considered purely source electrons.
- That the μ=50 [MeV/G] and μ=200 [MeV/G] cover different electron populations, and generally follow the same behaviour as the μ=100 [MeV/G] electrons in specific regions.
- That the μ=100 [MeV/G] are considered purely seed electrons.

So, in this section, we only use the μ=10 [MeV/G] electrons as source electrons and the μ=100 [MeV/G] electrons as seed electrons, and we compare their PSD with the appearance of chorus and Pc5 waves at each magnetospheric region. This way we try to reach some final conclusions about the relationship between them.

We gather some important comments in tables, with the following description of the maximum values of each quantity median:

×	Obscured, insignificant or only decreasing
✓	Around 1 or between 1-10
✓✓	Around 10 or between 10-10^2
✓✓✓	Around 10^2 or between 10^2-10^3
✓✓✓✓	Around 10^3 or between 10^3-10^4

Table 10 Legend for the method followed in this chapter. Each value range corresponds to a different symbol, for easier comparison. Table produced by the author.

5.5.1 L or L*=3-4 vs chorus waves, Pc5 waves, source e PSD and seed e PSD

The depicted quantities are the **chorus wave amplitude [nT] at L=3-4**, the **Pc5 wave power [nT^2/Hz] at L*=3-4**, the **PSD** $\left[\left(\frac{c}{MeV\ cm}\right)^3\right]$ **for source electrons of μ=10** $\left[\frac{MeV}{G}\right]$ **or E=10=100 [keV] and seed electrons of μ=100** $\left[\frac{MeV}{G}\right]$ **or E=100-600 [keV] at L*=3-4.** All values have been normalized to the median between 18-36 h before t_0, separately for the group of enhancement and of depletion events.

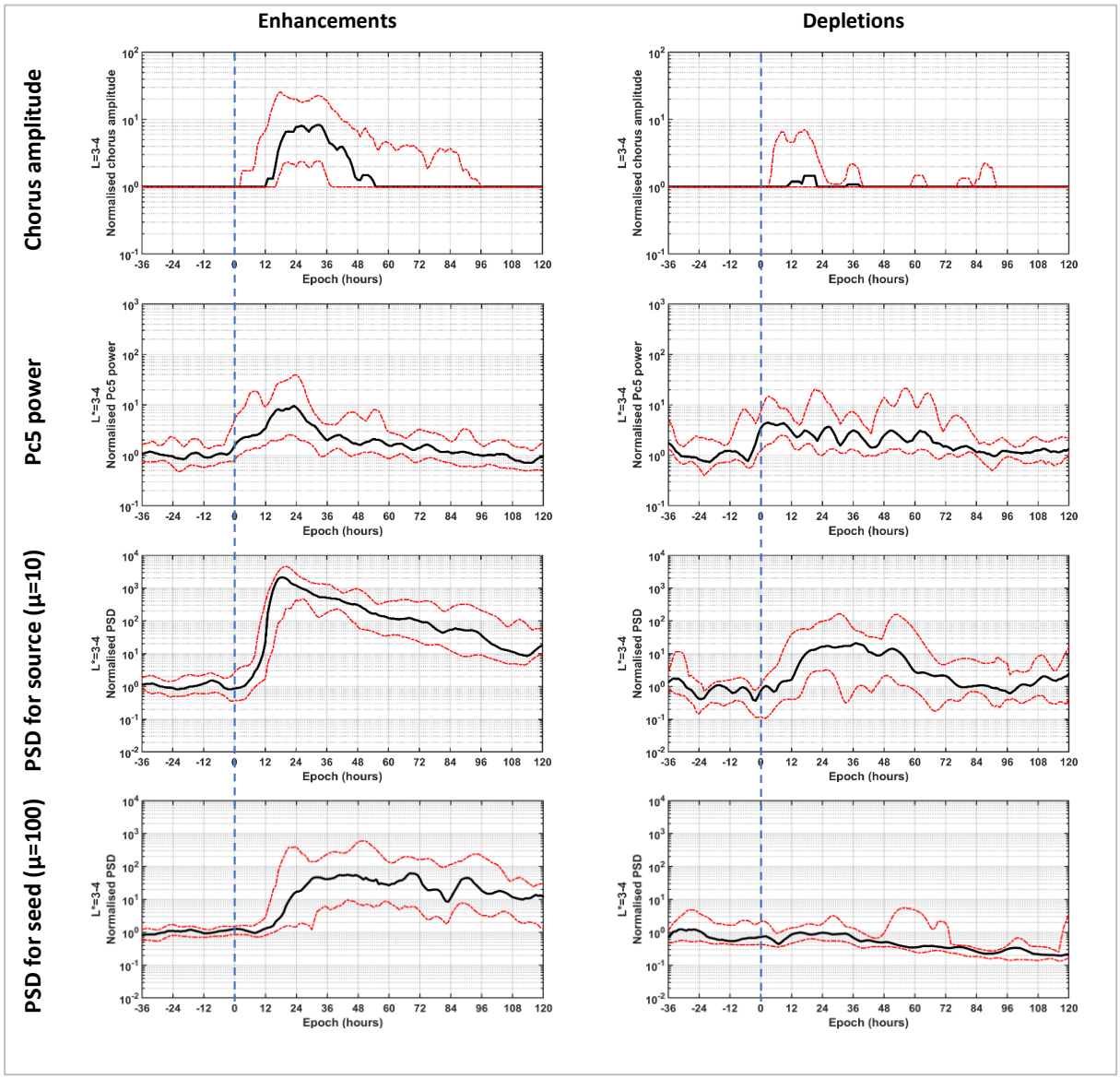

Figure 57 Comparison of some parameters from previous figures. Top to bottom: chorus wave amplitude [pT], Pc5 wave power [nT^2/Hz], PSD [(c·MeV^{-1}·cm^{-1})^3] for source electrons of μ=10 [MeV/G], PSD [(c·MeV^{-1}·cm^{-1})^3] for seed electrons of μ=100 [MeV/G], all at L=3-4 or L=3-4. We note that at L=3-4 the chorus waves are obscured by the plasmapause position.*

Chorus waves exhibit their lowest activity, almost none in depletion events, but we already explained that this is greatly affected by the plasmapause position which is mostly located over L=4. So, the chorus depiction is clearly obscured, and we cannot safely find any correlation or reach any conclusion in this region.

Pc5 waves also exhibit their lowest activity, lower than 10 nT^2, so they are considered insignificant as explained before, but more pronounced in enhancement events.

About the electrons, we see that source electrons of **μ=10 [MeV/G]** are more prominent in enhancement events, with a 2 orders of magnitude difference, and the seed electrons of **μ=100 [MeV/G]** appear pronounced only in enhancement events.

In summary:

At L*=3-4	Enhancement	Depletion
Chorus	× (obscured)	× (obscured)
Pc5	✓	✓
Source e	✓✓✓✓	✓✓
Seed e	✓✓	×

Table 11 The resulting comparison between enhancement and depletion events at L=3-4.*

We notice that there is a small correlation between source electrons and chorus waves, but we cannot safely confirm it, as mentioned above.

Source and seed electrons appear together in enhancement events, the source get injected and the seed are either injected or comprise of diffused electrons previously located at larger L*.

All the above should lead to the appearance or relativistic electrons in enhancement events, at least for relativistic electrons of μ=900 [MeV/G] at L*>4.5, as of which we sorted the events into the two categories. We continue this comparison at the rest of the regions. We still have to determine the mechanism responsible for accelerating these seed electrons to relativistic energies.

5.5.2 L or L*=4-5 vs chorus waves, Pc5 waves, source e PSD and seed e PSD

The depicted quantities are the **chorus wave amplitude [nT] at L=4-5**, the **Pc5 wave power [nT^2/Hz] at L*=4-5**, the **PSD** $\left[\left(\frac{c}{MeV\ cm}\right)^3\right]$ **for source electrons of μ=10** $\left[\frac{MeV}{G}\right]$ **or E=10-100 [keV] and seed electrons of μ=100** $\left[\frac{MeV}{G}\right]$ **or E=100-600 [keV] at L*=4-5**. All values have been normalized to the median between 18-36 h before t_0, separately for the group of enhancement and of depletion events.

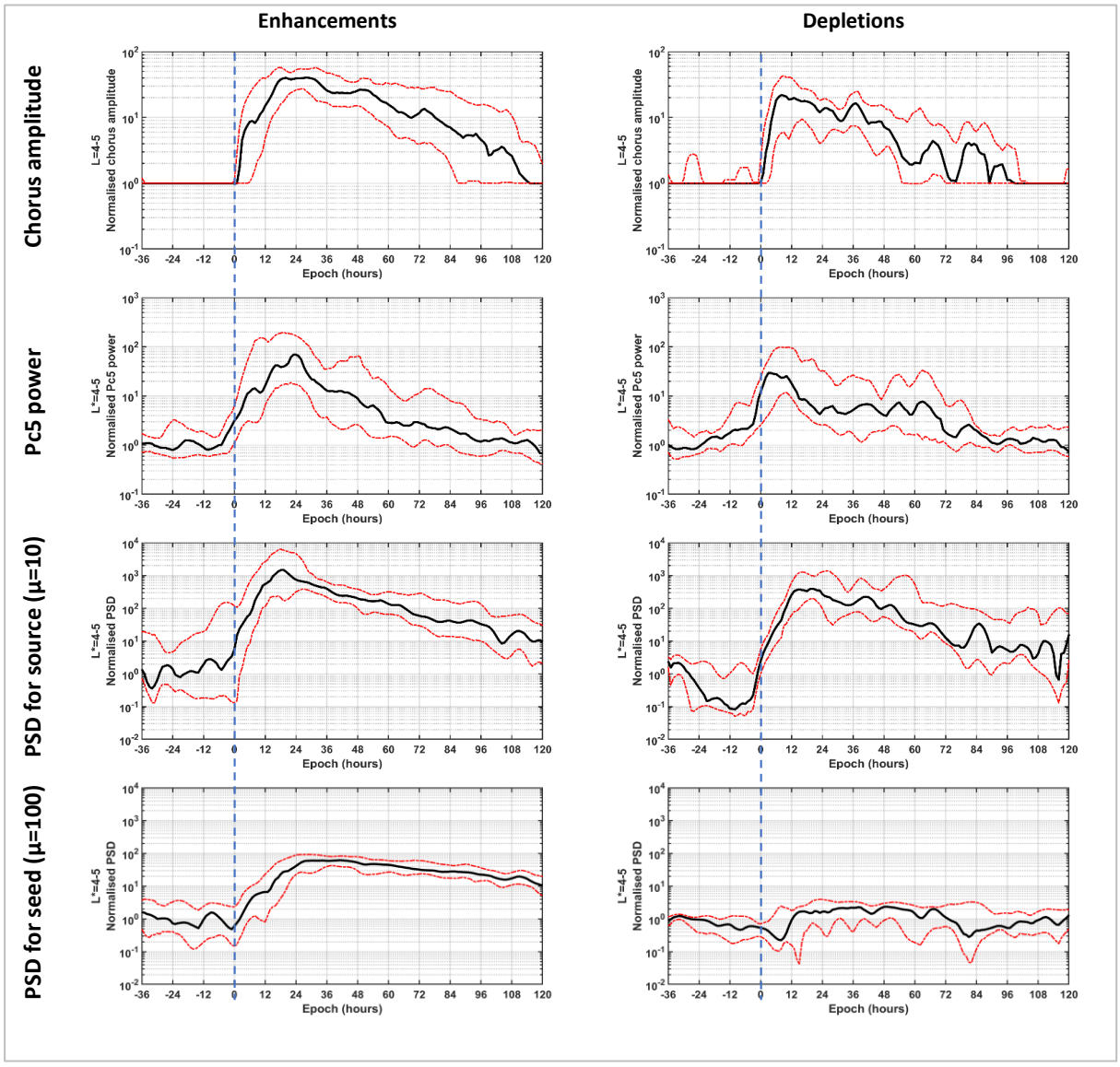

Figure 58 Comparison of some parameters from previous figures. Top to bottom: chorus wave amplitude [nT], Pc5 wave power [nT²/Hz], PSD [(c·MeV⁻¹·cm⁻¹)³] for source electrons of μ=10 [MeV/G], PSD [(c·MeV⁻¹·cm⁻¹)³] for seed electrons of μ=100 [MeV/G], all at L=4-5 or L=4-5.*

Chorus waves exhibit enhanced but not their greatest activity, with a comparable maximum value in both event categories but a greater duration in enhancement events.

Pc5 waves also exhibit enhanced activity, comparable in both event categories.

About the electrons, we see that source electrons of **μ=10 [MeV/G]** appear in both event categories with a comparable maximum value and duration, but seed electrons of **μ=100 [MeV/G]** appear more prominently in enhancement events.

In summary:

At L*=4-5	Enhancement	Depletion
Chorus	✓✓	✓✓
Pc5	✓✓	✓✓
Source e	✓✓✓✓	✓✓✓
Seed e	✓✓	✓

Table 12 The resulting comparison between enhancement and depletion events at L=4-5.*

Now that the chorus waves are not obscured by the plasmapause position, we can clearly see the correlation between source electrons and chorus waves, both in the order of magnitude difference and in the duration and fluctuations. This confirms that the chorus waves are emitted as a result of the source electron injection and energisation.

Source and seed electrons appear together only in enhancement events, but in depletion events, even though source electrons are comparable to those in enhancement events, the seed electrons almost do not appear. This confirms that the appearance of source and seed electrons is not entirely correlated, meaning that seed electrons are not comprised only by energised source electrons, but can depend on other mechanisms, such as the aforementioned direct injection from the plasma sheet, or the diffusion of electrons previously located at larger L*.

We do notice that in this region, the appearance of comparable source and seed electrons combined with the appearance of the waves, does indeed lead to the appearance or relativistic electrons in enhancement events, at least for relativistic electrons of μ=900 [MeV/G] at L*>4.5, as of which we sorted the events into the two categories. We continue this comparison at the last of the regions.

5.5.3 L or L*=5-6 vs chorus waves, Pc5 waves, source e PSD and seed e PSD

The depicted quantities are the **chorus wave amplitude [nT] at L=5-6**, the **Pc5 wave power [nT^2/Hz] at L*=5-6**, the **PSD** $\left[\left(\frac{c}{MeV\ cm}\right)^3\right]$ **for source electrons of μ=10** $\left[\frac{MeV}{G}\right]$ **or E=10-100 [keV] and seed electrons of μ=100** $\left[\frac{MeV}{G}\right]$ **or E=100-600 [keV] at L*=5-6**. All values have been normalized to the median between 18-36 h before t_0, separately for the group of enhancement and of depletion events.

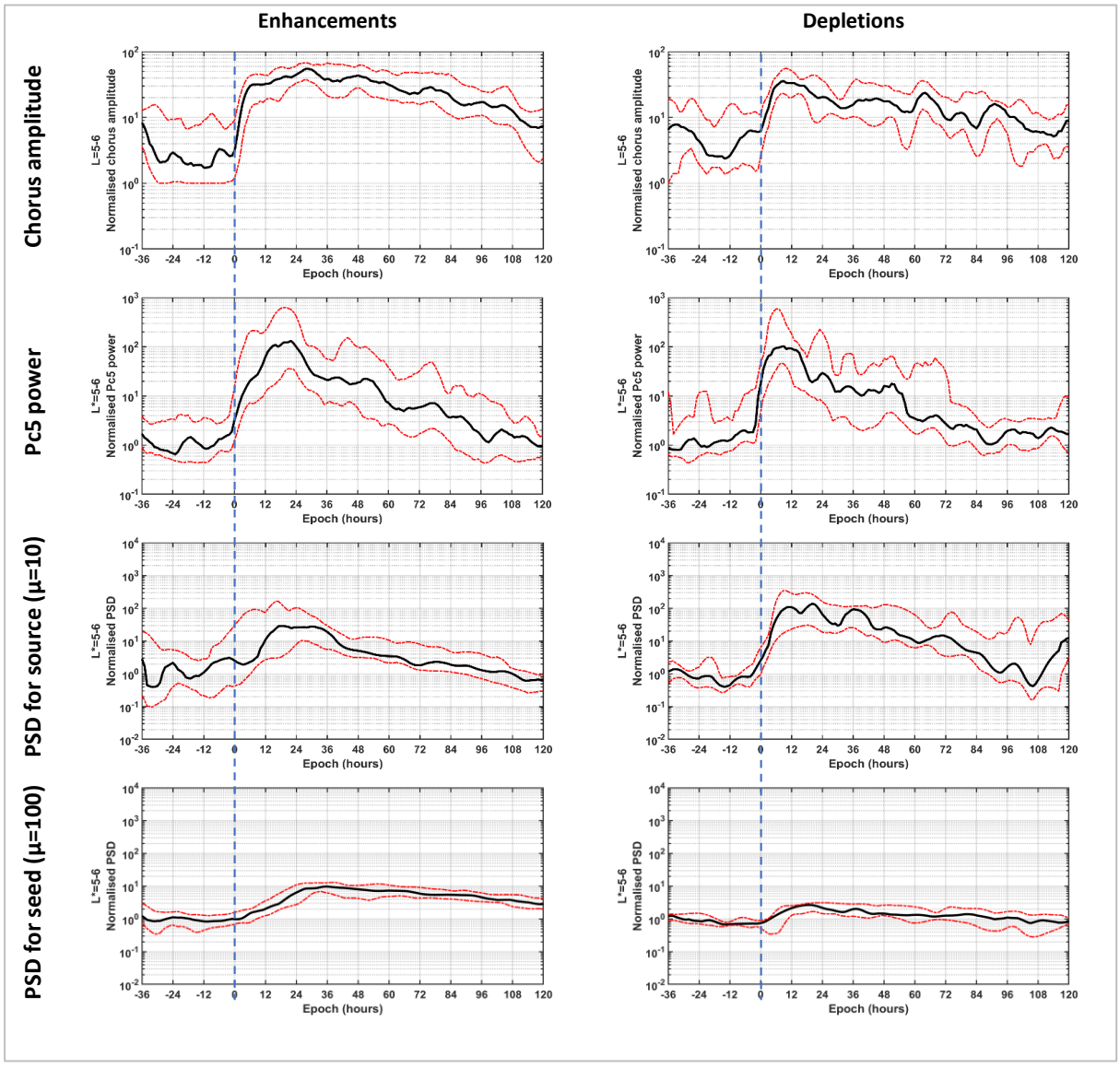

Figure 59 Comparison of some parameters from previous figures. Top to bottom: chorus wave amplitude [nT], Pc5 wave power [nT²/Hz], PSD [(c·MeV⁻¹·cm⁻¹)³] for source electrons of μ=10 [MeV/G], PSD [(c·MeV⁻¹·cm⁻¹)³] for seed electrons of μ=100 [MeV/G], all at L=5-6 or L=5-6.*

Chorus waves exhibit their greatest activity, with a larger maximum value and duration in enhancement events.

Pc5 waves also exhibit their most enhanced activity, comparable in both event categories, but with greater duration in enhancement events.

About the electrons, we see that source electrons of **μ=10 [MeV/G]** this time appear more prominently in depletion events, but the seed electrons of **μ=100 [MeV/G]** are more pronounced in enhancement events, but are almost insignificant in depletion events.

In summary:

At L*=5-6	Enhancement	Depletion
Chorus	✓✓	✓✓
Pc5	✓✓✓	✓✓
Source e	✓✓	✓✓✓
Seed e	✓✓	✓

Table 13 The resulting comparison between enhancement and depletion events at L=5-6.*

In this case we can see that even though the source electrons in enhancement events have a maximum 1 order of magnitude smaller than in the depletion events, the chorus waves that they emit are clearly comparable in both event categories.

Source and seed electrons almost appear enhanced together in enhancement events. Furthermore, in depletion events, source electrons appear more prominently but seed electrons do not. This means that the appearance of source and seed electrons is clearly independent.

We do notice that the appearance alone of plenty source electrons, does not lead to the appearance of either seed or relativistic electrons. Though, again we notice that the appearance of both source and seed electrons combined with the appearance of prolonged wave activity, does indeed lead to the appearance or relativistic electrons in enhancement events, at least for relativistic electrons of μ=900 [MeV/G] at L*>4.5, as of which we sorted the events into the two categories.

We arrange the previous tables all together in a different way to arrive at some conclusions:

Enhancement	L*=3-4	L*=4-5	L*=5-6
Chorus	× (obs)	✓✓	✓✓
Pc5	✓	✓✓	✓✓✓
Source e	✓✓✓✓	✓✓✓✓	✓✓
Seed e	✓✓	✓✓	✓✓

Depletion	L*=3-4	L*=4-5	L*=5-6
Chorus	× (obs)	✓✓	✓✓
Pc5	✓	✓✓	✓✓
Source e	✓✓	✓✓✓	✓✓✓
Seed e	×	✓	✓

Table 14 The final comparison for each event category, and for every L region, based on the previous Tables 11, 12 and 13.*

In both event categories, the chorus and Pc5 waves show a comparable behaviour at the same region, with larger maximum values and greater duration for increasing L*.

In enhancement events, the chorus and Pc5 waves reach larger maximum values and show greater duration compared to depletion events. The source electrons appear with larger maximum PSD values and greater duration of enhanced PSD that reaches smaller L* regions compared to depletion events. Also, in enhancement events, seed electrons do appear and follow the same behaviour, although in depletion events they reach smaller maximum values.

In summary, the two biggest differences between enhancement and depletion events, are the behaviour of the source electrons, that appear more inward in enhancement events, but do also appear in depletion events, and the behaviour of the seed electrons which are mostly pronounced only in enhancement events. These seed electrons interact with the chorus waves, reaching relativistic energies, and thus leading to the appearance of relativistic electrons of μ=900 [MeV/G] at L*>4.5, explaining the categorization we used in this study, according to Katsavrias et al. [2019].

So, we can conclude that:

- In enhancement events, the appearance of enhanced source and seed electrons at lower L*, together with the enhanced and prolonged wave activity, are efficient in accelerating the seed electrons to relativistic energies.
- In depletion events, the absence of enhanced source and seed electrons at lower L* together with the slightly smaller and shorter wave activity, cannot efficiently accelerate the seed electrons to relativistic energies.

Or, finally, that:

- The effect of VLF waves on the acceleration of electrons to relativistic energies seems to be determined by the abundance of seed electrons, mostly at L*=4-5, the nominal heart of the outer radiation belt.

Chapter 6: Conclusions

About the solar wind parameters:

- Enhancement events are caused by disturbances showing a two-step increased IMF, a prolonged negative Bz, and a highly increased and long lasting V_{SW} values reaching over 500 [km/s], together resulting in enhanced magnetic reconnection at the dayside magnetopause.

About the geomagnetic indices and the magnetospheric parameters:

- Enhancement events are characterised by increased geomagnetic activity, indicated by prolonged negative SYM-H and AL indices, meaning statistically stronger and more prolonged storm and substorm activity, and a significantly compressed plasmapause reaching under L=4.

About the chorus waves:

- Chorus waves appear at t_0 in both enhancement and depletion events, during enhanced geomagnetic storm and substorm activity, but decay with a smaller rate than the activity does.
- The chorus wave amplitude maximum value and duration increase with increasing L, in both enhancement and depletion events.
- In enhancement events the chorus wave activity is more pronounced and long-lasting over a broad L-shell region: at L=3-4 the waves appear more because of the more compressed plasmapause, at L=4-5 their duration is longer, but in L=5-6 their activity is comparable with that of depletion events.

About the Pc5 waves:

- Pc5 waves appear a while before t_0 in both event categories. During enhancement events their main drivers seem to be pressure pulses and instabilities generated by the enhanced solar wind velocity, while in depletion events, only pressure pulses are responsible for the excitation of Pc5 waves.
- The Pc5 wave power maximum value and duration increase with increasing L*, both in enhancement and depletion events.
- In enhancement events the Pc5 wave activity is more pronounced and longer-lasting: the wave power maximum value is less than 1 order of magnitude larger, is reached 24h after t_0, and the Pc5 wave activity decays slower, compared to depletion events, especially at L*=4-5. At L*=5-6 their activity is comparable.

About the source electrons of μ=1 [MeV/G]:

- The source electrons of μ=1 [MeV/G] do not appear to be affected by any kind of disturbance and in turn to have any effect in the variation of seed or relativistic electrons in enhancement or depletion events.

About the source electrons of μ=10 [MeV/G]:

- Source electrons of μ=10 [MeV/G] appear in both enhancement and depletion events with a comparable mean maximum value.
- The injections transporting the source electrons of μ=10 [MeV/G] to the inner magnetosphere are more effective in enhancement events, together with the more compressed plasmapause, bringing the electrons even at L*=3-4 with a more than 2 orders of magnitude difference compared to that of depletion events at the same region. At L*=4-5 they are comparable, and at L*=5-6 they are more pronounced in depletion events, as a result of the open drift shells in extreme events.
- The appearance of source electrons of μ=10 [MeV/G] does not in any way act as a proxy for the appearance of seed or relativistic electrons, at least for relativistic electrons of μ=900 [MeV/G] at L*>4.5, as of which we sorted the events into the two categories.

About the source/seed electrons of μ=50 [MeV/G]:

- Source/seed electrons of μ=50 [MeV/G] appear mostly in enhancement events. This means that the appearance of these electrons acts as a proxy for the appearance of relativistic electrons, at least for relativistic electrons of μ=900 [MeV/G] at L*>4.5, as of which we sorted the events into the two categories. But, because this population covers source and seed electrons, we will not use it as an indication of a specific behaviour.
- The injections transporting the source/seed electrons of μ=50 [MeV/G] to the inner magnetosphere are more effective in enhancement events, together with the more compressed plasmapause, bringing the electrons even at L*=3-4 with a more than 3 orders of magnitude difference compared to that of depletion events at the same region. At L*=4-5 they reach a maximum 1 order of magnitude larger, and at L*=5-6 they are comparable.
- The appearance of source/seed electrons of μ=50 [MeV/G] does not depend on the appearance of source electrons alone, but additional mechanisms are important. So, they either get directly injected from the plasma sheet as an effect of substorm activity, or they are comprised by diffused electrons previously located at larger L*, source electrons or other.

About the seed electrons of μ=100 [MeV/G]:

- Seed electrons of μ=100 [MeV/G] appear only in enhancement events, so they act as a proxy for the appearance of relativistic electrons, at least for relativistic electrons of μ=900 [MeV/G] at L*>4.5, as of which we sorted the events into the two categories.
- The injections transporting the seed electrons of μ=100 [MeV/G] to the inner magnetosphere are more effective in enhancement events, together with the more compressed plasmapause, bringing the electrons even at L*=3-4 with a more than 3 orders of magnitude difference

compared to that of depletion events at the same region. At L*=4-5 they reach a maximum 1 order of magnitude larger, and at L*=5-6 they are comparable.

- The appearance of seed electrons of μ=100 [MeV/G] does not depend on the appearance of source electrons alone, but additional mechanisms are important. So, they either get directly injected from the plasma sheet as an effect of substorm activity, or they are comprised by diffused electrons previously located at larger L*, source electrons or other.
- The seed electrons of μ=100 [MeV/G] and μ=50 [MeV/G] follow the same behaviour, mostly in smaller L* values where the μ=50 [MeV/G] are also seed electrons, so they rely on the same mechanisms.

About the seed/relativistic electrons of μ=200 [MeV/G]:

- Seed/relativistic electrons of μ=200 [MeV/G] appear only in enhancement events, so they can act as a proxy for the appearance of relativistic electrons, at least for relativistic electrons of μ=900 [MeV/G] at L*>4.5, as of which we sorted the events into the two categories.
- The injections transporting the seed/relativistic electrons of μ=200 [MeV/G] to the inner magnetosphere are more effective in enhancement events, together with the more compressed plasmapause, bringing the electrons even at L*=3-4 but with only 1 order of magnitude difference compared to that of depletion events at the same region. At L*=4-5 they reach a maximum 2 orders of magnitude larger, and at L*=5-6 only 1 order of magnitude larger.
- The appearance of seed/relativistic electrons of μ=200 [MeV/G] does not depend on the appearance of source electrons alone, but additional mechanisms are important. So, they either get directly injected from the plasma sheet as an effect of substorm activity, or they are comprised by diffused electrons previously located at larger L*, source electrons or other.
- The seed electrons of μ=200 [MeV/G] and μ=100 [MeV/G] follow the same behaviour, mostly in larger L* values where the μ=200 [MeV/G] are also seed electrons, so they rely on the same mechanisms.

About the difference between enhancement and depletion events:

- In enhancement events, the appearance of enhanced source and seed electrons at lower L*, together with the enhanced and prolonged wave activity, are efficient in accelerating the seed electrons to relativistic energies.
- In depletion events, the absence of enhanced source and seed electrons at lower L* together with the slightly smaller and shorter wave activity, cannot efficiently accelerate the seed electrons to relativistic energies.

About the effect of VLF waves in the electron acceleration:

- The effect of VLF waves on the acceleration of electrons to relativistic energies seems to be determined by the abundance of seed electrons, mostly at L*=4-5, the nominal heart of the outer radiation belt.

Finally, summarising the conclusions concerning only the enhancement events:

- They are caused by disturbances showing a two-step increased IMF, a prolonged negative Bz, and a highly increased and long lasting V_{SW} values reaching over 500 [km/s], together resulting in enhanced magnetic reconnection at the dayside magnetopause.
- They lead to increased geomagnetic activity, indicated by prolonged negative SYM-H and AL indices, meaning statistically stronger and more prolonged storm and substorm activity, and a significantly compressed plasmapause reaching under L=4.
- They result in more efficient injections of source and mostly seed electrons to the inner magnetosphere, even more pronounced at L*=3-4.
- They are characterised by more pronounced and prolonged chorus and Pc5 wave activity over a broad L-shell region.
- The abundance of the seed electrons accompanied by enhanced wave activity finally determines the effect of the enhancement events, being the electron acceleration to relativistic energies, mostly at L*=4-5, the nominal heart of the outer radiation belt.

Bibliography

Babcock H.W. (1961), The Topology of the Sun's Magnetic Field and the 22-Year Cycle, Astrophysical Journal, vol. 133, pp. 572-578, doi:10.1086/147060.

Baker D. and Daglis I.A. (2007), Radiation Belts and Ring Current, in: Space Weather - Physics and Effects, pp. 173-202, Springer Praxis Books. Springer, Berlin, Heidelberg, doi: 10.1007/978-3-540-34578-7_6.

Balasis G., Daglis I.A., Georgiou M., Papadimitriou C., Haagmans R. (2013), Magnetospheric ULF wave studies in the frame of Swarm mission: a time-frequency analysis tool for automated detection of pulsations in magnetic and electric field observations, in: Earth, Planets, and Space, vol. 65, pp. 1385-1398, doi: 10.5047/eps.2013.10.003.

Balasis G., Daglis I.A., Mann I.R. (2016), Waves, Particles, and Storms in Geospace: A Complex Interlay, Oxford University Press, doi: 10.1093/acprof:oso/9780198705246.001.0001.

Bingham S.T., Mouikis C.G., Kistler L.M., Boyd A.J., Paulson K., Farrugia C.J., Huang C.L., Spence H.E., Claudepierre S.G., Kletzing C. (2018), The Outer Radiation Belt Response to the Storm Time Development of Seed Electrons and Chorus Wave Activity During CME and CIR Driven Storms, J. Geophys. Res., vol. 123, pp. 10139-10157, doi: 10.1029/2018JA025963.

Boynton R.J., Aryan H., Walker S.N., Krasnoselskikh V., Balikhin M.A. (2018), The influence of solar wind and geomagnetic indices on Lower Band Chorus emissions in the inner magnetosphere, J. Geophys. Res., vol. 123, doi: 10.1029/2018JA025704.

Burton R.K., McPherron R.L., Russell C.T. (1975), An empirical relationship between interplanetary conditions and Dst. Journal of Geophysical Research, 80(31), 4204–4214, doi: 10.1029/JA080i031p04204.

Chen Y., Friedel H.W., Reeves G.D., Onsager T.G., Thomsen M.F. (2005), Multisatellite determination of the relativistic electron phase space density at geosynchronous orbit: Methodology and results during geomagnetically quiet times, J. Geophys. Res. Space Physics, vol. 110, A10210, doi: 10.1029/2004JA010895.

Claudepierre S.G., Elkington S.R., Wiltberger M. (2008), Solar wind driving of magnetospheric ULF waves: Pulsations driven by velocity shear at the magnetopause, J. Geophys. Res., vol. 113, A05218, doi:10.1029/2007JA012890.

Crooker N.U. (1977), The Magnetospheric Boundary Layers: A Geometrically Explicit Model, J. Geophys. Res., vol. 82, no. 25, pp. 3629–3633, doi:10.1029/JA082i025p03629.

Fennel J.F., Blake J.B., Claudepierre S., Mazur J., Kanekal S., O'Brien P., Baker D., Crain W., Mabry D., Clemmons J. (2016), Current energetic particle sensors, J. Geophys. Res Space Physics, vol. 121, pp. 8840-8858, doi: 10.1002/2016JA022588.

Hajra R., Tsurutani B.T., Echer E., Gonzalez W.D. (2014), Relativistic electron acceleration during high-intensity, long-duration, continuous AE activity (HILDCAA) events: Solar cycle phase dependences, Geophys. Res. Lett., vol. 41, pp. 1876– 1881, doi:10.1002/2014GL059383.

Hajra R., Tsurutani B.T., Echer E., Gonzalez W.D., Santolik O. (2015), Relativistic (E>0.6,>2.0 and >4.0 MeV) electron acceleration at geosynchronous orbit during high-intensity, long-doration,

continuous AE activity (HILDCAA) events, The Astrophysical Journal, vol. 799, pp. 39-46, doi: 10.1088/0004-637X/799/1/39.

Jaynes A.N.,Baker D.N., Singer H.J., Rodriguez J.V., Loto'aniu T.M., Ali A.F., Elkington S.R., Li X., Kanekal S.G., Claudepierre S.G., Fennell J.F., Li W., Thorne R.M., Kletzing C.A., Spence H.E., Reeves G.D. (2015), Source and seed populations for relativistic electrons: Their roles in radiation belt changes, J. Geophys. Res. Space Physics, vol. 120, pp. 7240-7254, doi: 10.1002/2015JA021234.

Jian L., Russell C.T., Luhmann J.G, Skoug R.M. (2006), Properties of Stream Interactions at One AU during 1995-2004, Solar Physics, vol. 239, pp. 337-392, doi: 10.1007/s11207-006-0132-3.

Kallenrode M.-B. (2004), Space Physics: An Introduction to Plasmas and Particles in the Heliosphere and Magnetospheres, Springer-Verlag, pp. 482, doi: 10.1007/978-3-662-09959-9.

Kataoka R., Miyoshi Y. (2006), Flux enhancement of radiation belt electrons during geomagnetic storms driven by coronal mass ejections and corotating interaction region, Space Weather, 4:09004, doi: 10.1029/2005SW000211.

Katsavrias C., Daglis I.A., Li W. (2019), On the statistics of acceleration and loss of relativistic electrons in the outer radiation belt: A superposed epoch analysis, J. Geophys. Res.: Space Physics, vol.124, pp. 2755–2768, doi: 10.1029/2019JA026569.

Katsavrias C. (2019), On the Variability of Seed, Relativistic and Ultra–Relativistic Electron Population in the Outer Van Allen Belt, PhD Dissertation, National and Kapodistrian University of Athens.

Kepko L., Spence H.E., Singer H.J. (2002), ULF waves in the solar wind as direct drivers of magnetospheric pulsations, Geophys. Res. Lett., 29(8), doi: 10.1029/2001GL014405.

Kivelson M.G., Russell C.T (1995), Introduction to Space Physics, Cambridge: Cambridge University Press.

Lam M.M., Horne R.B., Meredith N.P., Glauert S.A., Moffat-Griffin T., Green J.C (2010), Origin of energetic electron precipitation >30 keV into the atmosphere, J. Geophys. Res. Space Physics, 115:A00F08, doi: 10.1029/2009JA014619.

Levenberg K. (1944), A method for the solution of certain problems in least squares, Quarterly of Applied Mathematics, vol. 2, pp. 164-186.

Li W., Ma Q., Thorne R.M., Bortnik J., Zhang X.-J., Li J., Baker D.N., Reeves G.D., Spence H.E., Kletzing C.A., Kurth W.S., Hospodarsky G.B., Blake J.B., Fennell J.F., Kanekal S.G., Angelopoulos V., Green J.C., Goldstein J. (2016), Radiation belt electron acceleration during the 17 March 2015 geomagnetic storm: Observations and simulations, J. Geophys. Res. Space Physics, vol. 121, pp. 5520-5536, doi: 10.1002/2016JA022400.

Li W., Ni B., Thorne R.M., Bortnik J., Green J.C., Kletzing C.A., Kurth W.S., Hospodarsky G.B. (2013), Constructing the global distribution of chorus wave intensity using measurements of electrons by the POES satellites and waves by the Van Allen Probes, Geophys. Res. Lett., vol. 40, pp. 4526-4532, doi: 10.1002/grl.50920.

Li W., Thorne R.M., Bortnik J., Baker D.N., Reeves G.D., Kanekal S.G., Spence H.E., Green J.C. (2015), Solar wind conditions leading to efficient radiation belt electron acceleration: A superposed epoch analysis, Geophys. Res. Lett., vol. 42, issue 17, pp. 6906-6915, doi: 10.1002/2015GL065342.

Li W, Thorne R.M., Bortnik J., McPherron R., Nishimura Y., Angelopoulos V., Richardson I.G. (2012), Evolution of chorus waves and their source electrons during storms driven by corotating interaction regions, J. Geophys. Res., vol. 117, A08209, doi: 10.1029/2012JA017797.

Marquardt D.W. (1963), An algorithm for least squares estimation on nonlinear parameters, Society for Industrial and Applied Mathematics, vol. 11, pp. 431-441.

McPherron R.L. (2005), Magnetic Pulsations: Their Sources and Relation to Solar Wind and Geomagnetic Activity, Surveys in Geophysics, vol. 26, issue 5, pp. 545-592, doi: 10.1007s10712-005-1758-7.

Meredith N.P., Horne R.B., Anderson R.R. (2001), Substorm dependence of chorus amplitudes: Implications for the acceleration of electrons to relativistic energies, J. Geophys. Res., vol. 106, A7, pp. 13165-13178, doi: 10.1029/2000LA900156.

Meredith N.P., Horne R.B., Iles R.H.A., Thorne R.M., Heynderickx D., Anderson R.R. (2002), Outer zone relativistic electron acceleration associated with substorm-enhanced whistler mode chorus, J. Geophys. Res., vol. 107, A7, doi: 10.1029/2001JA900146.

Meredith N.P., Horne R.B., Sicard-Piet A., Boscher D., Yearby K.H., Li W., Thorne R.M. (2012), Global model of lower band and upper band chorus from multiple satellite observations, J. Geophys. Res., vol. 117, A10225, doi: 10.1029/2012JA017978.

Meredith N.P., Horne R.B., Summers D., Thorne R.M., Iles R.H.A., Heynderickx D., Anderson R.R. (2002), Evidence for acceleration of outer zone electrons to relativistic energies by whistler mode chorus, Ann. Geophys., vol. 20, pp. 967-979, doi: 10.5194/angeo-20-967-2002.

Mitchel D.G. (1994), The Space Environment, Fundamentals of Space Systems, edited by V.L. Pisacane and R.C. Moore, Oxford University Press, pp. 45-98.

Nasi A. (2017), Identification and study of Ultra-Low Frequency (ULF) waves during geospace magnetic storms (Ανίχνευση και μελέτη γεωμαγνητικών ταλαντώσεων χαμηλής συχνότητας κατά τη διάρκεια γεωδιαστημικών μαγνητικών καταιγίδων), Bachelor Thesis, National and Kapodistrian University of Athens, https://pergamos.lib.uoa.gr/uoa/dl/object/1911264.

Newell P.T., Sotirelis T., Liou K. Meng C.-I., Rich F.J. (2007), A nearly universal solar wind-magnetosphere coupling function inferred from 10 magnetospheric state variables, J. Geophys. Res., vol. 112, A01206, doi: 10.1029/2006JA012015.

Ni B., Li W., Thorne R.M., Bortnik J., Green J.C., Kletzing C.A., Kurth W.S., Hospodarsky G.B., and de Soria-Santacruz Pich M. (2014), A novel technique to construct the global distribution of whistler mode chorus wave intensity using low-altitude POES electron data, J. Geophys. Res. Space Physics, vol. 119, pp. 5658-5699, doi: 10.1002/2014JA019935.

O'Brien T.P., Moldwin M.B. (2003), Empirical plasmapause models from magnetic indices, Geophys. Res. Lett., 30:1152, doi: 10.1029/2002GL016007.

Olifer L., Mann I.R., Morley S.K., Ozeke L.G., Choi D. (2018), On the role of last closed drift shell dynamics in driving fast losses and Van Allen radiation belt extinction, J. Geophys. Res. Space Physics, vol. 123, pp. 3692-3703, doi: 10.1029/2018JA025190.

Parker E.N. (1963), The Solar-Flare Phenomenon and the Theory of Reconnection and Annihilation of Magnetic Fields, Astrophysical Journal, Supplement Series (U.S.), vol. 8, p. 177, doi:10.1086/190087.

Parks G.K. (1991), Physics of Space Plasmas – an Introduction, Addison-Wesley Publishing Co., Redwood City, CA.

Pierrard V., Stegen K. (2008), A three-dimansional dynamic kinetic model of the plasmasphere, J. Geophys. Res., 113, A10209, doi:10.1029/2008JA013060.

Pulkkinen T.I., Dimmock A.P., Osmane A., Nykyri K. (2015), Solar wind energy input to the magnetosheath and at the magnetopause, Geophys. Res. Lett., vol. 42, pp. 4723-4730, doi: 10.1002/2015GL064226.

Reeves G.D. (2015), Radiation Belt Electron Acceleration and Role of Magnetotail, in: Magnetotails in the Solar System (editors: Keiling A., Jackman C.M. and Delamere P.A.), doi: 10.1002/9781118842324.ch20.

Reeves G.D. (1998), Relativistic electrons and magnetic storms: 1992-1995, Geophys. Res. Lett., vol. 25, issue 11, pp. 1817-1820, doi: 10.1029/98GL01398.

Reeves G.D. and Daglis I.A. (2016), Geospace Magnetic Storms and the Van Allen Radiation Belts, in Waves, Particles and Storms in Geospace, edited by G. Balasis, I.A. Daglis, and I.R. Mann, Oxford University Press.

Reeves G.D, McAdams K.L., Friedel R.H., O'Brien T.P (2003), Acceleration and loss of relativistic electrons during geomagnetic storms, Geophys. Res. Let., 30:1529, doi: 10.1029/2002GL016513.

Russell C.T. (2007), The Coupling of the Solar Wind to the Earth's Magnetosphere, Space Weather: Physics and Effects, Springer Praxis Books, Springer Berlin Heidelberg, pp. 103-130, doi: 10.1007/978-3-540-34578-7_4.

Shue J.-H., Song P., Russel C.T., Steinberg J.T. Chao J.K., Zastenker G., Vaisberg O.L., Kokubun S., Singer H.J., Detman T.R., Kawano H. (1998), Magnetopause location under extreme solar wind conditions, J. Geophys. Res. Space Physics, vol. 103, pp. 17691-17700, doi: 10.1029/98JA01103.

Takahashi K., Miyoshi Y. (2016), Introduction to Wave-Particle Interactions and their Impact on Energetic Particles in Geospace, in: Waves, Particles, and Storms in Geospace: A Complex Interplay, doi: 10.1093/acprof:oso/9780198705246.003.0003.

Thorne R.M., Li W., Ni B., Ma Q., Bortnik J., Chen L., Baker D.N, Spence H.E., Reeves G.D., Henderson M.G., Kletzing C.A. Kurth W.S., Hospodarsky G.B., Blake J.B., Fennell J.F., Claudepierre S.G., Kanekal S.G. (2013), Rapid local acceleration of relativistic radiation-belt electrons by magnetospheric chorus, Nature, vol. 504, pp. 411-414, doi: 10.1038/nature12889.

Tsyganenko N.A., Sitnov M.I. (2005), Modeling the dynamics of the inner magnetosphere during strong geomagnetic storms, J. Geophys. Res. Space Physics, vol. 110, A03208, doi: 10.1029/2004JA010798.

Turner D.L., Li X. (2008), Radial gradients of phase space density of the outer radiation belt electrons prior to sudden solar wind pressure enhancements, Geophys. Res. Lett., vol. 35, L18101, doi: 10.1029/2008GL034866.

Turner D.L., Angelopoulos V., Li W., Hartinger M.D., Usanova M., Mann I.R., Bortnik J., Shprits Y. (2013), On the storm-time evolution of relativistic electron phase space density in Earth's outer radiation belt, J. Goephys. Res. Space Physics, vol. 118, pp. 2196-2212, doi: 10.1002/jgra.50151.

Walt, M. (1994). Introduction to Geomagnetically Trapped Radiation (Cambridge Atmospheric and Space Science Series). Cambridge: Cambridge University Press. doi:10.1017/CBO9780511524981.

Woodroffe J.R. (2010), Ultra-Low Frequency Waves, Magnetic Pulsations, and the Ionospheric Alfven Resonator, Retrieved from the University of Minnesota Digital Conservancy, http://purl.umn.edu/101391.

Xiao F., et al. (2014), Chorus acceleration of radiation belt relativistic electrons during March 2013 geomagnetic storm, J. Geophys. Res. Space Physics, vol. 119, pp. 3325-3332, doi: 10.1002/2014JA019822.

Zurbuchen T.H., Richardson I.G (2006), In-Situ Solar Wind and Magnetic Field Signatures of Interplanetary Coronal Mass Ejections, Space Sci. Rev., vol. 123, pp. 31023, doi: 10.1007/s11214-006-9010-4.

Online Sources

A Practical Guide to Wavelet Analysis	http://paos.colorado.edu/research/wavelets/
Matlab	https://www.mathworks.com/
National Oceanic and Atmospheric Administration	https://www.ngdc.noaa.gov/
NASA	https://www.nasa.gov/
NASA OMNIWeb Plus	https://omniweb.gsfc.nasa.gov/
RBSP Mission Data Directory	https://www.rbsp-ect.lanl.gov/science/DataDirectories.php
Tufts University	https://www.tufts.edu/
Wolfram	http://www.wolfram.com/
World Data Center for Geomagnetism, Kyoto	http://wdc.kugi.kyoto-u.ac.jp/

Wavelet software was provided by C. Torrence and G. Compo,
and is available at URL: http://atoc.colorado.edu/research/wavelets/.